Ab-Initio Simulations of Pressure Effects on Structural and Electronic Properties of Iron Based Superconductors

Dissertation zur Erlangung
des Doktorgrades des Naturwissenschaften

vorgelegt beim Fachbereich Physik
der Johann Wolfgang Goethe-Universität
in Frankfurt am Main

von
Milan Tomić
aus Smederevo, Serbien

Frankfurt am Main (2013)

vom Fachbereich Physik der
Johann Wolfgang Goethe-Universität als Dissertation angenommen

Dekan:

1. Gutachter:

2. Gutachter:

3. Gutachter:

Datum der Disputation:

Zussamenfassung

Die *ab-initio* Molekulardynamik-Methode ist eine der fundamentalsten Werkzeuge der heutigen Festkörperphysik und unersetzbar für die Untersuchung der mikroskopischen Eigenschaften von Materie. Das Ziel der *ab-initio* Molekulardynamik ist, die Zeitentwicklung von System aus wechselwirkenden Atomkernen und Elektronen zu beschreiben. Allgemein kann die elektronische Bewegung relativistisch untersucht werden. Diese Behandlung ist notwendig für die Beschreibung von schweren Elementen, wohingegen wir in dieser Arbeit Materialien behandeln werden, in denen relativistische Effekte vernachlässigbar sind.

Im ersten Kapitel geben wir einen allgemeinen Überblick über die Methode der nichtrelativistischen *ab-initio* Molekulardynamik. Unser Ausgangspunkt ist dabei die überaus komplizierte Vielteilchen-Hamiltonfunktion, welche ein System von nichtrelativistischen Atomkernen und Elektronen beschreibt, die über die Coulombkraft miteinander wechselwirken. Mit Hilfe der Born-Oppenheimer-Näherung und weiteren adiabatischen Näherungen können gewichtige Vereinfachungen des Problems erreicht werden. Entsprechend der Tatsache, dass Atomkerne eine um mindestens drei Größenordnungen höhere Masse als Elektronen besitzen, kann man annehmen, dass die Elektronen instantan auf Änderungen der Konfiguration der Atomkerne reagieren, wohingegen die Atomkerne selbst sich entsprechend der klassischen Bewegungsgleichungen bewegen. Dies bedeutet, dass für die elektronische Wellenfunktion die Position der Atome eine vergleichsweise einfache parametrische Abhängigkeit darstellt und damit eine Hamiltonfunktion konstruiert werden kann, in der die Coulombwechselwirkung mit den Atomkernen nur als externes Potential eingeht. Wenn die resultierende effektive Schrödingergleichung für das elektronische Problem gelöst wird, kann daraus ein effektives Coulombpotential berechnet werden, welches zusammen mit der interatomaren Coulombwechselwirkung die Kräfte auf die Atome zugänglich und berechenbar macht. Mit dieser Methode wird das Ziel, die zeitliche Entwicklung der atomaren Positionen und elektronischen Wellenfunktion zu beschreiben, erreichbar.

Das Problem, eine Lösung der Schrödingergleichung zu finden, bleibt damit weiterhin bestehen. Ein bis heute sehr erfolgreicher Ansatz ist die Dichtefunktionaltheorie (DFT), welche wir im zweiten Kapitel vorstellen werden. Wie bereits vorher bemerkt, geht in der betrachteten effektiven Hamiltonfunktion die Wechselwirkung der Elektronen mit den Atomkernen als ein externes Potential ein. Alle weiteren Terme sind *universell*, das heißt sie hängen nicht von den spezifischen Eigenschaften des zu untersuchenden Materials ab. Als Konsequenz lässt sich daraus das Hohenberg-Kohn-Theorem formulieren, welches besagt, dass das externe Potential eindeutig durch die elektronische Grundzustandsdichte bestimmt ist. Dies erlaubt es uns, alle Observablen als Funktionale der Elektronendichte aufzufassen. Die Elektronendichte ist nur noch eine Funktion der drei Ortskoordinaten, wodurch wir eine signifikante Vereinfachung gegenüber der elektronischen Vielteilchenwellenfunktion erreichen, welche von $3N$ Variablen abhängt (wobei N die Anzahl der Elektronen beschreibt). Eine weitere wichtige Vereinfachung lässt sich durch eine Ein-Elektron-Parametrisierung der Elektronendichte erreichen, in der ein fiktives System von Elektronen nur durch ein effektives gemitteltes Feld wechselwirkt. Für dieses System wird gefordert, dass es die gleiche Elektronendichte wie das ursprüngliche reale System besitzt. Damit bildet man das eigentliche Problem des Findens der Elektronendichte des Gesamtsystems auf das Lösen eines Eigenwertproblems einer effektiven Ein-Elektron-Schrödingergleichung ab. Die resultierenden Gleichungen sind als Kohn-Sham-Gleichungen bekannt, mit den zugehörigen Ein-Elektron-Wellenfunktionen, den Kohn-Sham Orbitalen. Die größte Hürde der Dichtefunktionaltheorie ist dabei, dass die genaue Form des Funktionals des effektiven gemittelten Feldes nicht bekannt ist, und so gewisse Näherungen notwendigerweise erfolgen müssen. Trotz dieser Tatsache kann die Dichtefunktionaltheorie in vielen System beachtliche Erfolge erzielen. Eine Ausnahme bilden dabei Systeme von stark korrelierten Materialien. Eisenbasierte Supraleiter gehören zur Kategorie der weniger stark korrelierten Systeme, so dass sich auch mit der DFT genaue Vorhersagen für diese Materialien treffen lassen.

Im dritten Kapitel widmen wir uns der konkreten Implementierung der DFT. Eine optimale numerische Leistung wird durch wählen einer möglichst kleinen Basis erreicht. Dies ist allgemein ein schwieriges Problem, da die Forderung einer akkuraten Beschreibung der Wellenfunktion in der interatomaren Region auf der einen Seite, sowie die Beschreibung der lokalisierten Elektronen in Atomkernnähe auf der anderen Seite zueinander komplementär sind. Ein weit verbreiteter Ansatz ist, den Raum in zwei Bereiche zu unterteilen: Einmal in einen sogenannten Interstitialbereich zwischen den Atomen, und einmal in einen sphärischen Bereich um die Atome selbst, wobei für jeden dieser zwei Teilbereiche eine spezialisierte Basis gewählt wird. Eine Umsetzung dieser Idee ist die Projektoren-erweiterte Wellenmethode, oder auch Projector Augmented Wave method (PAW), welche für die meisten in dieser Arbeit gezeigten Rechnung verwendet wurde.

Die PAW Methode verwendet Operatoren, welche die elektronische Wellenfunktion in eine glatte Pseudowellenfunktion transformieren, die wiederum effizient in einer Basis von ebenen Wellen entwickelt werden kann. Diese Transformation wird erreicht durch die Verwendung von Atom-ähnlichen Projektorfunktionen in der Atomkernregion. Es ist auch möglich, eine Atom-ähnliche Basis im gesamten Raum zu verwenden, wie es beispielsweise in der sogenannten vollen Potential- und lokalen Orbitalmethode, oder auch Full Potential Local Orbital method (FPLO) realisiert wird. Diese Methode ist die zweite, die in dieser Arbeit zur Anwendung kam und ist besonders geeignet für die Konstruktion von projektiven Wannierfunktionen und stark gebundenen Modellen, wie zum Beispiel in sogenannten Tight-Binding Modellen.

Die Simulation von Ausübung von Druck auf ein Material sowie das numerische Lösen der Kohn-Sham-Gleichungen erfordert die Anwendung von Minimierungs- und Diagonalisierungsalgorithmen, welche wir im vierten Kapitel behandeln werden. Ein Diagonalisierungsproblem kann einerseits als ein Minimierungsproblem betrachtet werden, andererseits kann auch mit Hilfe des Variationsprinzip ein Minimierungsproblem als Diagonalisierungsproblem formuliert werden. Simulationen von hydrostatischem Druck oder Strukturvorhersagen bei Nulldruck können durch eine Minimierung der Enthalpie erreicht werden. Dies kann erfolgen durch Verwendung eines Minimierungsalgorithmus wie der konjugierten Gradientenmethode oder anderer quasi-Newtonscher Methoden. Die Ausübung von nichthydrostatischem Druck hingegen bedarf eines anderen Ansatzes. Für diesen Zweck haben wir eine Methode entwickelt, die auf einer Modifizierung des schnellen Inertial-Relaxationsalgorithmus, oder auch Fast Inertial Relaxation Engine (FIRE), basiert. Der FIRE Algorithmus erreicht eine numerische Minimierung durch Integration von Newton-ähnlichen Bewegungsgleichungen. Die Verwendung von Differentialgleichungen zweiter Ordnung und daraus resultierenden inertialen Eigenschaften macht diesen Algorithmus zu einer nichtlokalen Minimierungsmethode, da die Information der Energielandschaft in den Geschwindigkeiten der betrachteten Teilchen codiert ist. Daher kann FIRE lokale Minimierungsmethoden in komplizierten Energielandschaften übertreffen. Weiterhin konnten wir aufgrund der metadynamischen Eigenschaften von FIRE den Algorithmus modifizieren und den Konfigurationsraum um die kristallinen Freiheitsgrade erweitern. Dadurch erhielten wir Bewegungsgleichungen, mit denen es möglich wurde, den Spannungstensor an die Einheitszelle des Kristalls zu koppeln.

Im fünften Kapitel werden wir die vorher diskutierten Methoden auf reale Systeme anwenden und unsere Ergebnisse der *ab-initio* Simulationen von druckinduzierten Effekten in $BaFe_2As_2$ und $CaFe_2As_2$ diskutieren. Zuerst geben wir eine Einführung in die Struktur und die phänomenologischen Eigenschaften von Eisenbasierten Supraleitern. Wir konzentrieren uns dabei auf die 122-Familie von Eisenpniktiden, die insbesondere unter

Druck interessante Effekte aufweist. Die Eisenbasierten Supraleiter werden im Allgemeinen supraleitend unter Anwendung von externem Druck, wobei ein Übergang von einer magnetisch geordneten orthorhombischen Phase hin zu einer tetragonalen nichtmagnetischen Phase zu beobachten ist. Eine besondere Eigenschaft der 122-Familie ist das Auftreten einer kollabierten tetragonalen Phase, deren Einfluss auf die supraleitenden Eigenschaften bisher nicht zufriedenstellend geklärt ist. Ebenso sind die exakten Druckbedingungen für die Supraleitung nicht ausreichend verstanden. Daher untersuchen wir in dieser Arbeit auch uniaxialen Druck als weitere Möglichkeit, die Eigenschaften dieser Systeme zu modifizieren. Dazu führen wir eine systematische Untersuchung durch, in der wir hydrostatischen sowie uniaxialen Druck entlang der Kristallaxen $\mathbf{a}$, $\mathbf{b}$, $\mathbf{c}$ und $\mathbf{a}+\mathbf{b}$ auf die zu untersuchenden Systeme ausüben. Dabei werden unsere Resultate zeigen, dass uniaxialer Druck in $\mathbf{c}$-Richtung den kritischen Druck für den Übergang von der orthorhombischen zur tetragonalen Phase um eine Größenordnung in $BaFe_2As_2$ sowie $CaFe_2As_2$ reduzieren kann. Weiterhin werden wir sehen, dass in $BaFe_2As_2$ eine weitere tetragonale Phase vor dem Übergang in die kollabierte tetragonale Phase existiert. Im Unterschied zur experimentellen Beobachtung finden wir in $CaFe_2As_2$ keine solche tetragonale Phase. Der strukturelle Phasenübergang in die tetragonale Phase in $BaFe_2As_2$ wird begleitet von signifikanten Änderungen in der Fermifläche, wobei die Lochzylinder um den Γ-Punkt verschwinden und dadurch mögliche Cooperpaar-Streuungskanäle zwischen Elektron- und Lochtaschen unterdrückt werden. Wir sehen, dass applizierter Druck in der Ebene, kompressiv wie expansiv, keinen Übergang von der orthorhombischen zur tetragonalen Phase herbeiführen kann. Stattdessen finden wir, dass Druck in gleicher Ebene eine Vertauschung der ferromagnetischen und antiferromagnetischen Richtungen zur Folge hat, was eine direkte Konsequenz der intrinsischen magnetoelastischen Kopplung und des Drucks ist. Unsere Ergebnisse geben weiterhin Einsicht in den Mechanismus der sogenannten Entzwilligung in der orthorhombischen Phase und treffen Vorhersagen zum kritischen Druck bei dem eine Invertierung der Orthorhombizität in Domänen stattfindet.

Das sechste Kapitel behandelt die Entfaltung der elektronischen Bandstruktur und deren Anwendung auf Eisenbasierte Supraleiter. Dies ist insbesondere wichtig für Systeme in denen die ursprüngliche Translationssymmetrie gebrochen ist und Superzellenrechnungen notwendig werden. Die Analyse der resultierenden elektronischen Struktur wird so durch Faltung der Brillouinzone erschwert. Um dieses Problem zu lösen haben wir eine Methode zur Entfaltung der Bandstruktur basierend auf Gruppentheoretischen Prinzipien entwickelt. In dieser Herangehensweise bilden wir das Entfaltungsproblem auf die irreduziblen Unterräume der Raumgruppe ab. Dieser Ansatz ermöglicht es uns, die Punktgruppenoperationen auf der gleichen Basis wie Translationen zu behandeln und

so unter gewissen Bedingungen die Bandstruktur hinausgehend über reine Translationssymmetrie zu entfalten. Diese Möglichkeit ist wichtig für Modellrechnungen, wo die Minimierung des Konfigurationsraumes von großem Vorteil ist. Die projektiven Eigenschaften dieser Methode erlauben eine anschauliche physikalische Erklärung des Entfaltens, da die irreduziblen Unterräume orthogonal bezüglich jeder Observable sind, die der Symmetrie der Raumgruppe entspricht. Zur Hilfestellung findet der Leser eine Einführung in das Thema der irreduziblen Darstellungen von Raumgruppen im Anhang dieses Kapitels.

Weitere in diesem Zusammenhang wichtige Ergebnisse werden im siebten Kapitel vorgestellt, bei denen der Verfasser dieser Arbeit mit beteiligt war. Wichtige Resultate wurden dabei bei der Untersuchung des gigantischen Volumenkollaps von MnS_2 unter Druck erzielt, ebenso bei der Untersuchung der elektronischen Struktur in alkalidotiertem Picen. In der Studie über MnS_2, geleitet von S. Kimber, wurden *ab-initio* Simulationen unter Druck durchgeführt und die relativen Stabilitätsregionen der konkurrierenden Hochspin- und Niedrigspin-Phasen von MnS_2 bestimmt, sowie mit Phononenrechnungen die Stabilitäten der Struktur überprüft. Die Niedrigspin-Struktur bei hohem Druck von MnS_2 wurde dabei als Arsenopyrit-artig und als ein effektiv valenzgebundener Festkörper identifiziert. Das fehlen metallischer Eigenschaften sowie das Vorhandensein von Valenzbindungen lassen auf einen qualitativ neuen Mechanismus des Volumenkollaps in MnS_2 schließen, mit wichtigen Konsequenzen für das Verständnis des äußeren Mantels der Erde. Im Falle von alkalidotiertem Picen konnten experimentell bisher nicht zugängliche Kristallstrukturen untersucht werden. Aufgrund dieser Strukturen konnte durch Rechnungen von H. Lee basierend auf dynamischer Molekularfeldtheorie (DMFT) die experimentellen Photoemissionsexperimente von A. Ruff in alkalidotiertem Picen erklärt, sowie die Bedeutung der elektronischen Korrelationen in diesem System aufgezeigt werden.

Im achten und letzten Kapitel geben wir eine Zusammenfassung der Ergebnisse dieser Arbeit und einen Ausblick auf zukünftige Untersuchungen. Da die Überschätzung des magnetischem Moments das zurzeit bedeutendste Problem bei der Simulation von Eisenbasierten Supraleitern unter Druck darstellt, ist eine mögliche Verbesserung der Dichtefunktionaltheorie durch eine Austauschfeld-Skalierung wünschenswert. Ein Erfolg auf diesem Gebiet wäre von großem Vorteil insbesondere für die *ab-initio* Untersuchung von dotierten Eisenpniktidsupraleitern. Studien dieser Art sind außerdem von besonderer Bedeutung für das Verständnis von Störstellen in Eisenselenid-Verbindungen wie FeSe oder KFe_2Se_2, sowie uniaxialer Spannung in Systemen von FeSe auf $SrTiO_3$-Substraten, in denen die höchsten kritischen Temperaturen T_c beobachtet wurden. Auch das Entfalten der Bandstruktur ist dabei bedeutsam, da Rechnungen mit großen Superzellen notwendig sind. Die Generalisierung und Erweiterung dieser Methode über Inklusion der magnetischen Symmetrien ist dabei sehr erstrebenswert, was zum Beispiel durch die Hinzunahme der irreduziblen Repräsentationen von Shubnikovgruppen möglich ist.

Abstract

The *ab-initio* molecular dynamics framework has been the cornerstone of computational solid state physics in the last few decades. Although it is already a mature field it is still rapidly developing to accommodate the growth in solid state research as well as to efficiently utilize the increase in computing power. Starting from the first principles, the *ab-initio* molecular dynamics provides essential information about structural and electronic properties of matter under various external conditions.

In this thesis we use the *ab-initio* molecular dynamics to study the behavior of $BaFe_2As_2$ and $CaFe_2As_2$ under the application of external pressure. $BaFe_2As_2$ and $CaFe_2As_2$ belong to the family of iron based superconductors which are a novel and promising superconducting materials. The application of pressure is one of two key methods by which electronic and structural properties of iron based superconductors can be modified, the other one being doping (or chemical pressure). In particular, it has been noted that pressure conditions have an important effect, but their exact role is not fully understood.

To better understand the effect of different pressure conditions we have performed a series of *ab-initio* simulations of pressure application. In order to apply the pressure with arbitrary stress tensor we have developed a method based on the Fast Inertial Relaxation Engine, whereby the unit cell and the atomic positions are evolved according to the metadynamical equations of motion.

We have found that the application of hydrostatic and **c** axis uniaxial pressure induces a phase transition from the magnetically ordered orthorhombic phase to the non-magnetic collapsed tetragonal phase in both $BaFe_2As_2$ and $CaFe_2As_2$. In the case of $BaFe_2As_2$, an intermediate tetragonal non-magnetic tetragonal phase is observed in addition. Application of the uniaxial pressure parallel to the **c** axis reduces the critical pressure of the phase transition by an order of magnitude, in agreement with the experimental findings. The in-plane pressure application did not result in transition to the non-magnetic tetragonal phase and instead, rotation of the magnetic order direction could be observed. This is discussed in the context of Ginzburg-Landau theory. We have also found that the magnetostructural phase transition is accompanied by a change in the Fermi surface

topology, whereby the hole cylinders centered around the Γ point disappear, restricting the possible Cooper pair scattering channels in the tetragonal phase. Our calculations also permit us to estimate the bulk moduli and the orthorhombic elastic constants of $BaFe_2As_2$ and $CaFe_2As_2$.

To study the electronic structure in systems with broken translational symmetry, such as doped iron based superconductors, it is necessary to develop a method to unfold the complicated bandstructures arising from the supercell calculations. In this thesis we present the unfolding method based on group theoretical techniques. We achieve the unfolding by employing induced irreducible representations of space groups. The unique feature of our method is that it treats the point group operations on an equal footing with the translations. This permits us to unfold the bandstructures beyond the limit of translation symmetry and also formulate the tight-binding models of reduced dimensionality if certain conditions are met. Inclusion of point group operations in the unfolding formalism allows us to reach important conclusions about the two versus one iron picture in iron based superconductors.

And finally, we present the results of *ab-initio* structure prediction in the cases of giant volume collapse in MnS_2 and alkaline doped picene. In the case of MnS_2, a previously unobserved high pressure arsenopyrite structure of MnS_2 is predicted and stability regions for the two competing metastable phases under pressure are determined. In the case of alkaline doped picene, crystal structures with different levels of doping were predicted and used to study the role of electronic correlations.

Contents

List of Figures

List of Tables

Preface

The main research topic of the thesis are structural and electronic effects of pressure application in the iron pnictide family of superconductors. The particular question we aimed to examine was the role of particular pressure conditions, or more precisely, what is the difference between the application of hydrostatic and uniaxial pressure.

We concerned mainly two materials, $BaFe_2As_2$ and $CaFe_2As_2$, where application of pressure, yields very prominent structural and electronic effects, one of the most remarkable being manifested in the appearance of the so-called collapsed tetragonal phase.

To proceed with such a study, it is necessary to employ a number of methods and theoretical concepts. In order to maintain conceptual simplicity and provide a reasonably self-contained coverage of the performed research, the exposition of material in this thesis is laid out linearly and every chapter builds on the exposition of the previous chapter, while at the same time introducing the necessary information.

Since the general problematics of simulation of pressure application belongs to the realm of the ab-initio molecular dynamics, the first half of this thesis introduces the topic. A general overview of the formalism of ab-initio molecular dynamics is given in first chapter. The formalism of ab-initio molecular dynamics reduces the immensely complicated problem of the many-body interaction in the system composed of atomic nuclei and their electrons into two loosely coupled, and thus, more manageable problems of the nuclear and the electronic subsystems. Motion of atomic nuclei can be treated classically. However, atomic nuclei move in a potential arising from the internuclear Coulomb interaction and the effective potential arising from the interaction with the electronic subsystem.

In order to solve the equations of motion of atomic nuclei, it is necessary to solve the quantum equations of motion of the electronic system first. This is achieved by the Density Functional Theory formalism which is outlined in the second chapter. Density Functional Theory leverages one-to-one mapping between the many-body electronic ground

state and the corresponding charge density. This allows for single electron parametrization of the many body electronic state which leads to immense simplification of the computational requirements since it casts the many-body problem in the form of the familiar single-electron Schrödinger equation.

Choice of the convenient basis is of paramount importance for numerically solving the equations based on Density Functional Theory. All computational results presented in this thesis use either Projector Augmented Wave basis or localized basis of the Full Potential Local Orbital method which are described in the third chapter.

Once the basis is in place, all ingredients for solving the problem of the electronic motion are set. To achieve the structure prediction at zero temperature it is necessary to optimize positions of the atomic nuclei so that their interaction energy is minimized. This is the objective of structure optimization methods which are described in the fourth chapter. To simulate the application of hydrostatic pressure, methods like conjugate gradient can be used. However, simulation of application of uniaxial pressure has required the development of a new method. We have achieved that by modifying the metadynamics of the Fast Inertial Relaxation Engine so that the equations of motion treat lattice degrees of freedom on an equal footing with the atomic degrees of freedom.

With this achieved, we could perform the study of effects of pressure on $BaFe_2As_2$ and $CaFe_2As_2$. We have simulated the effects of hydrostatic and uniaxial pressures along all three crystallographic axes of the orthorhombic unit cell of $BaFe_2As_2$ and $CaFe_2As_2$ as well as along the diagonal of the iron plane. Detailed analysis of structural and electronic properties was performed for all optimized structures. A Ginzburg-Landau analysis of the in-plane application of uniaxial pressure was performed in collaboration with Rafael M. Fernandes. Results of this study, as well as short overview of basic properties of iron based superconductors is given in the fifth chapter

In the analysis of the electronic structure it is very useful to be able to unfold the complicated bandstructures obtained for systems where the original translational symmetry is broken. This is why an original method to unfold the bandstructures and tight-binding models was developed, based on group theoretical principles. The method is described in the sixth chapter, and in order to facilitate the discussion of the unfolding method, a brief overview of the necessary group theoretical concepts is given in the appendix.

Our pressure simulation method has proven itself very robust and apart from the cases of $BaFe_2As_2$ and $CaFe_2As_2$ we also applied the method successfully to the study of the giant volume collapse in MnS_2 as well as to theoretical prediction of alkali doped picene structures. In both cases important results were contributed to the main study and they are outlined in the seventh chapter.

Finally, all results are briefly summarized in the eighth chapter and a possible path towards the future studies is outlined.

Chapter 1

Ab-initio Molecular Dynamics

The most important information that can be obtained from the microscopic modeling of matter is through its structural and electronic behavior. These properties are the main subject of this thesis, which has the study of the electronic and the structural properties of the iron-pnictide materials as a principal goal.

At the microscopic level, the quantum treatment of matter is a highly complex problem with multitude of approaches, each describing certain aspects with varying levels of success. A few of these different approaches can be roughly unified within the framework of the Ab-Initio Molecular Dynamics which provides a set of approximation driven principles allowing access to the most relevant electronic and structural properties [1, 2]. This is achieved by decoupling simpler, classical, structural equations from the highly complex electronic equations. The structural properties are intimately tied to the spatial distribution of the atomic nuclei interacting through the effective Coulomb potential. This potential arises from the classical pairwise electrostatic interaction of nuclei and the complex interaction of electrons driven by the laws of quantum mechanics. Of course, the electronic problem still remains a highly complex issue.

This chapter is organized in the following way. First, the Hamiltonian of the many-body problem is outlined and then the approximations needed to carry out the separation of the equations of motion of the atomic nuclei and the electrons, namely the adiabatic and the Born-Oppenheimer approximations, are developed. Finally, the classical treatment of the equations of motion of atomic nuclei is made.

1.1 Non-relativistic Many-Body Hamiltonian

Let us suppose that we have a solid consisting of N positively charged atomic nuclei (ions) located at positions $\boldsymbol{R}_n$ and M electrons at positions $\boldsymbol{r}_\alpha$, all interacting via the Coulomb interaction only. Then, the Hamiltonian of such system is given by

$$\hat{\mathrm{H}} = \hat{\mathrm{T}}_\mathrm{I} + \hat{\mathrm{T}}_\mathrm{E} + \hat{\mathrm{V}}_\mathrm{II} + \hat{\mathrm{V}}_\mathrm{IEe} + \hat{\mathrm{V}}_\mathrm{EE} = \sum_{n=1}^{N} \frac{\hat{\mathbf{P}}_n^2}{2M_n} + \sum_{\alpha=1}^{M} \frac{\hat{\mathbf{p}}_\alpha^2}{2m} + \frac{e^2}{8\pi\varepsilon_0} \sum_{n=1}^{N}\sum_{m=1}^{N} \frac{Z_n Z_m}{|\hat{\mathbf{R}}_n - \hat{\mathbf{R}}_m|} - \frac{e^2}{4\pi\varepsilon_0} \sum_{n=1}^{N}\sum_{\alpha=1}^{M} \frac{Z_n}{|\hat{\mathbf{R}}_n - \hat{\mathbf{r}}_\alpha|} + \frac{e^2}{8\pi\varepsilon_0} \sum_{\alpha=1}^{M}\sum_{\beta=1}^{M} \frac{1}{|\hat{\mathbf{r}}_\alpha - \hat{\mathbf{r}}_\beta|} \quad (1.1)$$

where the terms are

- $\hat{\mathrm{T}}_\mathrm{I}$ is kinetic energy operator of ions
- $\hat{\mathrm{T}}_\mathrm{E}$ is kinetic energy operator of electrons
- $\hat{\mathrm{V}}_\mathrm{II}$ is potential energy operator of ion-ion interaction
- $\hat{\mathrm{V}}_\mathrm{IE}$ is potential energy operator of ion-electron interaction
- $\hat{\mathrm{V}}_\mathrm{EE}$ is potential energy operator of electron-electron interaction

In the coordinate representation, momentum operators become derivative operators $\hat{\mathbf{P}}_n = \partial_{\boldsymbol{R}_n}$, $\hat{\mathbf{p}}_\alpha = \partial_{\boldsymbol{r}_\alpha}$ (where $\partial/\partial x = \partial_x$), position operators become multiplicative operators $\hat{\mathbf{R}}_n = \boldsymbol{R}_n$, $\hat{\mathbf{r}}_\alpha = \boldsymbol{r}_\alpha$, and a state of the system is determined by a wavefunction $\langle \boldsymbol{R}, \boldsymbol{r} | \Psi(t) \rangle = \Psi(\boldsymbol{R}, \boldsymbol{r}, t)$, satysfying the Schrödinger equation

$$i\hbar \frac{\partial}{\partial t} \Psi(\boldsymbol{R}, \boldsymbol{r}, t) = \hat{\mathrm{H}} \Psi(\boldsymbol{R}, \boldsymbol{r}, t) \quad (1.2)$$

where $\boldsymbol{R}$ and $\boldsymbol{r}$ denote totality of electronic and ionic positions. Equation (1.2) is a non-linear differential equation for a function of $3N + 3M$ variables, describing all of the ionic and electronic degrees of freedom. Since both N and M are of the order of the Avogadro number $N_A \sim 10^{23}$, the solution to eq. (1.2) becomes computationally intractable.

1.2 Adiabatic and Born-Oppenheimer Approximation

In order to reach a computationally practical method for solving eq. (1.2) a series of approximations are required. We first consider the Born-Oppenheimer[3], and the adiabatic approximations, which are used to decouple the motion of ions and electrons. The reasoning behind the approximation is that ions are much more massive than electrons, at least by three orders of magnitude. This means that the characteristic response time of the electronic motion is smaller than the characteristic response time of the atomic motion by the same order of magnitude. The consequence is that the electronic states can be considered to instantaneously adapt to any given ionic configuration. We can now show that the interactions between the electrons and the atomic nuclei are unable to bring about transitions between the stationary electronic states, which is the final requirement that needs to be fulfilled in order to decouple the ionic from the electronic motion.

To proceed with this consideration, we factorize the solution to eq. (1.2) in the following manner

$$\Psi(\boldsymbol{R},\boldsymbol{r},t) = \langle \boldsymbol{R},\boldsymbol{r}| \sum_{\lambda} |\Psi_\lambda(t)\rangle = \langle \boldsymbol{R},\boldsymbol{r}| \sum_{\lambda} |\Phi_\lambda(t)\rangle \otimes |\psi_\lambda\rangle = \sum_{\lambda} \Phi_\lambda(\boldsymbol{R},t)\psi_\lambda(\boldsymbol{R},\boldsymbol{r}) \quad (1.3)$$

where $\psi_\lambda(\boldsymbol{R},\boldsymbol{r})$ comprise the electronic wavefunction basis satisfying the Schrödinger equation for the effective electronic Hamiltonian $\hat{\mathrm{H}}_\mathrm{E}$

$$\hat{\mathrm{H}}_\mathrm{E}\psi_\lambda(\boldsymbol{R},\boldsymbol{r}) = (\hat{\mathrm{T}}_\mathrm{E} + \hat{\mathrm{V}}_\mathrm{IE} + \hat{\mathrm{V}}_\mathrm{EE})\psi_\lambda(\boldsymbol{R},\boldsymbol{r}) = E_\lambda(\boldsymbol{R})\psi_\lambda(\boldsymbol{R},\boldsymbol{r}) \quad (1.4)$$

In other words, eq. (1.3) decomposes the full state into the sum of factorizable states, where the electronic factor-state satisfies, eq. (1.4) (where dependency on the ionic configuration is purely parametric), and the entire time dependence is held in the ionic factor state. With this ansatz we can now proceed to find the Hamiltonian matrix elements

$$\langle\Psi(t)|\hat{\mathrm{H}}|\Psi(t)\rangle = \langle\Psi(t)|\left[\hat{\mathrm{T}}_\mathrm{I} + \hat{\mathrm{T}}_\mathrm{E} + \hat{\mathrm{V}}_\mathrm{II} + \hat{\mathrm{V}}_\mathrm{IE} + \hat{\mathrm{V}}_\mathrm{EE}\right]|\Psi(t)\rangle = \langle\Psi(t)|\left[\hat{\mathrm{T}}_\mathrm{I} + \hat{\mathrm{V}}_\mathrm{II} + E_\lambda\right]|\Psi(t)\rangle \quad (1.5)$$

where we have used eq. (1.4) and the fact that $\hat{\mathrm{T}}_\mathrm{E}$ acts only on $|\psi_\lambda\rangle$. Now, it is necessary to evaluate the matrix elements of $\hat{\mathrm{T}}_\mathrm{I}$. However, some additional care needs to be

taken, since $\hat{\mathrm{T}}_\mathrm{I}$ acts both on the electronic and the ionic factor-states. In the coordinate representation, the matrix elements become

$$\langle\Psi(t)|\hat{\mathrm{T}}_\mathrm{I}|\Psi(t)\rangle = \sum_{n=1}^{N}\sum_{\kappa}\sum_{\lambda}\frac{\hbar^2}{2M_n}\int\int \mathrm{d}\boldsymbol{R}\mathrm{d}\boldsymbol{r}\Phi_\kappa(\boldsymbol{R},t)\psi_\kappa(\boldsymbol{R},\boldsymbol{r})\frac{\partial^2}{\partial\boldsymbol{R}_n^2}\left[\Phi_\lambda(\boldsymbol{R},t)\psi_\lambda(\boldsymbol{R},\boldsymbol{r})\right] \quad (1.6)$$

where we have assumed the functions Φ and ψ to be real, since eq. (1.2) is real. When derivatives in the integrand of eq. (1.6) are calculated, the matrix element of the ionic kinetic energy is

$$\begin{aligned}\langle\Psi_\kappa(t)|\hat{\mathrm{T}}_\mathrm{I}|\Psi_\lambda(t)\rangle = \sum_{n=1}^{N}\sum_{\kappa}\sum_{\lambda}\frac{\hbar^2}{2M_n}\Bigg[&\int \mathrm{d}\boldsymbol{R}\Phi_\kappa(\boldsymbol{R},t)\frac{\partial^2}{\partial\boldsymbol{R}_n^2}\Phi_\lambda(\boldsymbol{R},t)\delta_{\kappa\lambda} + \\ &\int \mathrm{d}\boldsymbol{r}\psi_\kappa(\boldsymbol{R},\boldsymbol{r})\frac{\partial^2}{\partial\boldsymbol{R}_n^2}\psi_\lambda(\boldsymbol{R},\boldsymbol{r})\delta_{\kappa\lambda} + \\ 2\int\int \mathrm{d}\boldsymbol{R}\mathrm{d}\boldsymbol{r}\Phi_\kappa(\boldsymbol{R},t)&\left[\frac{\partial}{\partial\boldsymbol{R}_n}\Phi_\lambda(\boldsymbol{R},t)\right]\psi_\kappa(\boldsymbol{R},\boldsymbol{r})\left[\frac{\partial}{\partial\boldsymbol{R}_n}\psi_\lambda(\boldsymbol{R},\boldsymbol{r})\right]\Bigg] \quad (1.7)\end{aligned}$$

For the first and the second terms on the right hand side, we have employed the fact that both the electronic and the ionic wave functions are orthonormal. Were it not for the third term in the right hand side of eq. (1.7), the kinetic energy matrix would be diagonal, and hence the Hamiltonian eq. (1.5) would be also diagonal, since all interaction terms are diagonal. This would mean, that if we prepare the system in the pure state $|\Psi_\lambda(t)\rangle = |\Phi_\lambda(t)\rangle \otimes |\psi_\lambda\rangle$, it would remain in that state indefinitely. Also, we could factorize the eq. (1.2) into separate equations for the electronic and the ionic states. The electronic state would be determined by eq. (1.4) and the ionic state would be given by the equation

$$i\hbar\frac{\partial}{\partial t}|\Phi_\lambda(t)\rangle = \hat{\mathrm{H}}|\Phi_\lambda(t)\rangle = \left(\hat{\mathrm{T}}_\mathrm{I} + \langle\psi_\lambda|\hat{\mathrm{T}}_\mathrm{I}|\psi_\lambda\rangle + \hat{\mathrm{V}}_\mathrm{II} + E_\lambda\right)|\Phi_\lambda(t)\rangle \quad (1.8)$$

This result is known as the adiabatic approximation. The remaining question is, which conditions are required so that the third term on the right-hand side of the eq. (1.7) can be neglected.

The third term, rewritten in the Dirac notation, is

$$I_3 = 2\sum_{n=1}^{N}\sum_{\kappa}\sum_{\lambda}\frac{1}{M_n}\langle\Phi_\kappa(t)|\hat{\mathbf{P}}_n|\Phi_\lambda(t)\rangle\cdot\langle\psi_\kappa|\hat{\mathbf{P}}_n|\psi_\lambda\rangle$$

If I_3 is much smaller than the difference between E_λ and E_κ, then the off-diagonal matrix elements of the Hamiltonian will be too small to cause a transition between the states $|\Psi_\lambda\rangle$ and $|\Psi_\kappa\rangle$, which means that the condition for the adiabatic approximation to hold is

$$\frac{1}{M}\left|\langle\Phi_\kappa(t)|\hat{\mathbf{P}}_n|\Phi_\lambda(t)\rangle\cdot\langle\psi_\kappa|\hat{\mathbf{P}}_n|\psi_\lambda\rangle\right| \ll |E_\lambda - E_\kappa|$$

where M is a mass of the order of the typical ionic mass. If we assume the characteristic frequency of the electronic motion caused by the interaction with the ions to be ω_{IE}, then we have that

$$\frac{m}{M}\left|\frac{\hbar\omega_{\mathrm{IE}}}{E_\lambda - E_\kappa}\right| \ll 1 \tag{1.9}$$

Since the prefactor of m/M is always smaller than $5\cdot10^{-4}$, the condition in eq. (1.9) will hold unless electronic energy levels are very close. This can happen in some exceptional cases, such as the case of Jahn-Teller systems. For metallic systems, where there is no gap at the Fermi level, the adiabatic approximation is justified by the fact that the relevant energy scale of a few eV is dictated by the plasmon excitations, which will dominate any excitations produced by ionic interactions.

In summary, we have shown that in the large majority of cases, separation of the electronic and the ionic motion through the adiabatic approximation is justified and that, electronic and ionic motions are dictated by the equations (1.4) and (1.8), respectively. However, these equations are still not fully decoupled, since the electronic states enter the ionic Schrödinger equation through diagonal matrix elements of the ionic kinetic energy. Despite of this, these matrix elements, have been shown to contribute less than 0.5% to the right hand side of the eq. (1.8) and can be omitted. The approximation in which those matrix elements are dropped, is known as the Born-Oppenheimer approximation.

1.3 Classical Approximation of the Ionic Motion

Since atomic nuclei have a large mass, their thermal wavelength $\lambda_T = \hbar(2Mk_BT)^{-1/2}$ is very small. For Hydrogen at room temperature λ_T is around $0.2\mathring{A}$. Since internuclear

distances are an order of magnitude larger, a quantum treatment of atomic nuclei is unnecessary. The only exception is Hydrogen at very low temperatures.

We arrive at the classical approximation by taking the expectation values of the ionic position and momentum operators at a given state $|\Psi_\lambda\rangle$, $\langle\hat{\mathbf{R}}_n\rangle_\lambda$ and $\langle\hat{\mathbf{P}}_n\rangle_\lambda$ and identifying them as the values of the classical position and the momentum variables in that state. The time evolution of the expectation values is given by the Ehrenfest theorem

$$i\hbar\frac{\partial}{\partial t}\langle\hat{\mathbf{R}}_n\rangle_\lambda = \langle[\hat{\mathrm{H}},\hat{\mathbf{R}}_n]\rangle_\lambda$$
$$i\hbar\frac{\partial}{\partial t}\langle\hat{\mathbf{P}}_n\rangle_\lambda = \langle[\hat{\mathrm{H}},\hat{\mathbf{P}}_n]\rangle_\lambda$$

The second equation gives the Newton's equations of motion. The commutator of the momentum and the Hamiltonian operator is given by

$$\langle[\hat{\mathrm{H}},\hat{\mathbf{P}}_n]\rangle_\lambda = \left\langle\left[\sum_{n=1}^{N}\frac{\hbar^2}{2M_n}\frac{\partial^2}{\partial\boldsymbol{R}_n^2} + \hat{\mathrm{V}}_{\mathrm{II}} + E_\lambda(\boldsymbol{R}), -i\hbar\frac{\partial}{\partial\boldsymbol{R}_n}\right]\right\rangle_\lambda =$$
$$i\hbar\frac{\partial}{\partial\boldsymbol{R}_n}\left(\left\langle\hat{\mathrm{V}}_{\mathrm{II}}\right\rangle_\lambda + E_\lambda\right) = i\hbar\frac{\partial}{\partial\boldsymbol{R}_n}\left\langle\hat{\mathrm{V}}_{\mathrm{II}}\right\rangle_\lambda + i\hbar\frac{\partial}{\partial\boldsymbol{R}_n}\langle\psi_\lambda|\hat{\mathrm{H}}_{\mathrm{E}}|\psi_\lambda\rangle = i\hbar\frac{\partial\tilde{E}_\lambda}{\partial\boldsymbol{R}_n}$$

where $\tilde{E}_\lambda = \left\langle\hat{\mathrm{V}}_{\mathrm{II}}\right\rangle_\lambda + E_\lambda$. As a consequence of the Born-Oppenheimer approximation, we can assume that the electronic state is always variational with respect to the ionic configuration, since electrons always have enough time to assume a state which minimizes the energy. Since this is the case, the Hellmann-Feynman theorem can be employed to calculate the derivative of the expectation value of the electronic energy

$$\frac{\partial E_\lambda}{\partial\boldsymbol{R}_n} = \left\langle\psi_\lambda\middle|\frac{\partial\hat{\mathrm{H}}_{\mathrm{E}}}{\partial\boldsymbol{R}_n}\middle|\psi_\lambda\right\rangle$$

Finally, if n_λ are occupation numbers of states $|\psi_\lambda\rangle$, then the classical equations of motion for atomic nuclei are

$$\frac{\partial\boldsymbol{P}_n}{\partial t} = \sum_\lambda n_\lambda\frac{\partial\tilde{E}_\lambda}{\partial\boldsymbol{R}_n} \tag{1.10}$$

A special case of (1.10) is the structural optimization problem where $\partial\boldsymbol{P}_n/\partial t = 0$. This means that, we need to find the ionic positions $\boldsymbol{R}_n^*$ for which the total energy $\tilde{E} = \sum_\lambda n_\lambda\tilde{E}_\lambda$ is minimized, ie. $\partial_{\boldsymbol{R}_n}\tilde{E}\Big|_{\boldsymbol{R}_n^*} = 0$. In other words, we need to find a stable structure for a given chemical composition. This is one of the fundamental problems in

ab-initio molecular dynamics and is also an essential part of this thesis. Some structural optimization methods, which were important for our studies are described in (insert section).

It is worth pointing out here that the electronic Schrödinger equation (1.4) can now be written as

$$\left(\hat{\mathrm{T}} + \hat{\mathrm{V}} + \hat{\mathrm{V}}_{\mathrm{Ext}}\right)|\psi\rangle = E|\psi\rangle \tag{1.11}$$

where $\hat{\mathrm{T}}$ is the electronic kinetic energy, $\hat{\mathrm{V}}$ is the electron-electron interaction and $\hat{\mathrm{V}}_{\mathrm{Ext}}$ is the electron-ion interaction, here termed "external". The reason for that nomenclature is that, the electron-ion interaction is external to the electron system when considered independently from the ions in the context of the Born-Oppenheimer approximation.

1.4 Summary

The purpose of this section was to briefly introduce the method of ab-initio molecular dynamics. We have started with the many-body Hamiltonian (1.1) and the corresponding Schrödinger equation (1.2) for the wavefunction of all atomic nuclei and electrons. It was then shown that by employing the adiabatic and the Born-Oppenheimer approximation, the wavefunction can be factorized into electronic and ionic wavefunctions. The electronic wavefunction can be obtained by solving the effective electronic problem (1.4), a highly nontrivial task, where the ionic configuration enters only as a parameter. The electronic energy levels and states can then be plugged into the classical equation of ionic motion (1.10), which can then be solved.

Chapter 2

Density Functional Theory

In the previous chapter, the method of ab-initio molecular dynamics was introduced. We have seen how, knowing the electronic state, classical equations of motion of atomic nuclei can be solved. However, the major problem of the electronic state is still unsolved. Historically, there have been many approaches, but, arguably, the most successful one is the Density Functional Theory.

The Density Functional Theory is based on the Hohenberg-Kohn theorems which state that the electron density contains all of the information needed to calculate the energy of the system. This vastly simplifies the problem since instead of solving for the wavefunction, which is a function of $3N$ variables, where N is the number of electrons, we have to solve for the electron density which is a function of 3 variables and can be obtained by cleverly employing single-electron approximations.

In this chapter we will start with the Hohenberg-Koh theorems since they are relatively straight-forward and self-contained as a consequence of the variational principle. Then, the non-relativistic electronic Hamiltonian will be introduced and the possibility of single electron wafefunction parametrization of the many-electron state will be discussed, leading to the introduction of the Kohn-Sham equations, as a way to conduct practical computations. Finally, spin-polarized density functional theory will be outlined.

2.1 Hohenberg-Kohn Theorems

Since the early days of the quantum mechanics and the Thomas-Fermi model[4][5], it was believed that the energy of the electrons described by eq. (1.11), depends only on the electron density. This assertion was formally proved by the Hohenberg-Kohn theorems[6].

Let us repeat eq. (1.11) with the first two terms fully expanded.

$$\left(\sum_{\alpha=1}^{M}\frac{\hat{\mathbf{p}}_\alpha^2}{2m}+\frac{e^2}{4\pi\varepsilon_0}\sum_{\alpha=1}^{M}\sum_{\beta=1}^{M}\frac{1}{|\hat{\mathbf{r}}_\alpha-\hat{\mathbf{r}}_\beta|}+\hat{\mathrm{V}}_{\mathrm{Ext}}\right)|\psi\rangle=E|\psi\rangle$$

As stated previously, this equations determines the electronic state and the electronic energy levels. The first two terms are the electronic kinetic energy and the electron-electron Coulomb interaction, while the third term is the electron-ion Coulomb interaction. The first two terms are universal, that is, they will have the same form for every substance under consideration. The third term is the only term that distinguishes different substances. It is therefore natural to assume that there is a correspondence between the external potential and the electron density. Precisely this is the content of the first Hohenberg-Kohn theorem

Theorem I The external potential is uniquely determined by the ground state electron density up to an additive constant.

Proof Let us assume the opposite, namely, that there are two arbitrary external potentials $\hat{\mathrm{V}}^1_{\mathrm{Ext}}$ and $\hat{\mathrm{V}}^2_{\mathrm{Ext}}$ with the same ground state electron density ρ. Let the states $|\psi^1\rangle$ and $|\psi^2\rangle$ be the ground states corresponding to these two external potentials. We have then that the ground state energies are

$$\begin{aligned}E_0^1&=\left\langle\psi^1\right|\hat{\mathrm{H}}^1\left|\psi^1\right\rangle=\left\langle\psi^1\right|\hat{\mathrm{T}}+\hat{\mathrm{V}}+\hat{\mathrm{V}}^1_{\mathrm{Ext}}\left|\psi^1\right\rangle\\E_0^2&=\left\langle\psi^2\right|\hat{\mathrm{H}}^2\left|\psi^2\right\rangle=\left\langle\psi^2\right|\hat{\mathrm{T}}+\hat{\mathrm{V}}+\hat{\mathrm{V}}^2_{\mathrm{Ext}}\left|\psi^2\right\rangle\end{aligned}$$

According to the variational principle, the expectation value for $\hat{\mathrm{H}}^1$ is minimal for the ground state $|\psi^1\rangle$ which means that

$$E_0^1<\left\langle\psi^2\right|\hat{\mathrm{H}}^1\left|\psi^2\right\rangle=\left\langle\psi^2\right|\hat{\mathrm{H}}^2\left|\psi^2\right\rangle+\left\langle\psi^2\right|\hat{\mathrm{H}}^1-\hat{\mathrm{H}}^2\left|\psi^2\right\rangle=E_0^2+\int\mathrm{d}\boldsymbol{r}\rho(\boldsymbol{r})[v^1_{\mathrm{Ext}}(\boldsymbol{r})-v^2_{\mathrm{Ext}}(\boldsymbol{r})]\quad(2.1)$$

where $v^1_{\mathrm{Ext}}(\boldsymbol{r})$ and $v^2_{\mathrm{Ext}}(\boldsymbol{r})$ are the densities of the potential energy defined as

$$\left\langle\psi^i\right|\hat{\mathrm{V}}^i_{\mathrm{Ext}}\left|\psi^i\right\rangle=\int\mathrm{d}\boldsymbol{r}\rho(\boldsymbol{r})v^i_{\mathrm{Ext}}(\boldsymbol{r})$$

for $i = 1, 2$. We can now rewrite eq. (2.1) for the external potential $\hat{\mathrm{V}}^2_{\mathrm{Ext}}$ and the Hamiltonian $\hat{\mathrm{H}}^2$ in the state $|\psi^1\rangle$ which yields

$$E_0^2 < \left\langle \psi^1 \middle| \hat{\mathrm{H}}^2 \middle| \psi^1 \right\rangle = \left\langle \psi^1 \middle| \hat{\mathrm{H}}^1 \middle| \psi^1 \right\rangle + \left\langle \psi^1 \middle| \hat{\mathrm{H}}^2 - \hat{\mathrm{H}}^1 \middle| \psi^1 \right\rangle = E_0^1 + \int \mathrm{d}\boldsymbol{r} \rho(\boldsymbol{r})[v^2_{\mathrm{Ext}}(\boldsymbol{r}) - v^1_{\mathrm{Ext}}(\boldsymbol{r})] \quad (2.2)$$

If we sum eqs. (2.1) and (2.2) we arrive at

$$E_0^1 + E_0^2 < E_0^1 + E_0^2$$

which is a contradiction, impliying that the external potentials $\hat{\mathrm{V}}^1_{\mathrm{Ext}}$ and $\hat{\mathrm{V}}^1_{\mathrm{Ext}}$ have to be identical.

A direct and very important consequence of the theorem is that the ground state $|\psi\rangle$ is also uniquely determined by the electron density, since the Schrödinger equation (1.11) is uniquely determined by the external potential.

Let us now introduce the notion of a functional. Broadly speaking, a functional is a function that maps a function onto a number. It is a useful concept since our goal in the Density Functional Theory is to express expectation values of all observables as a functional of the electron density. For the single electron local observables it can be done in the following manner

$$O[\rho] = \left\langle \psi \middle| \hat{\mathrm{O}} \middle| \psi \right\rangle = \int \mathrm{d}\boldsymbol{r} \hat{\mathrm{o}}(\boldsymbol{r}) \rho(\boldsymbol{r}) \quad (2.3)$$

where $\hat{\mathrm{o}}(\boldsymbol{r})$ is the density of the variable $\hat{\mathrm{O}}$ and the notation $O[\rho]$ is used to specify that the expectation value of the observable $\hat{\mathrm{O}}$ is a functional of the electron density.

In the proof of the first theorem, we have used the fact that the energy is minimal in the ground state. Whether the energy is minimal for the ground state electron density is a separate question which is answered by the second Hohenberg-Kohn theorem.

Theorem II Let $\tilde{\rho}(\boldsymbol{r})$ be an arbitrary electron density of N electrons. We can define the energy functional E_{Trial} as

$$E_{\mathrm{Trial}}[\tilde{\rho}] = F[\tilde{\rho}] + \int \mathrm{d}\boldsymbol{r} v_{\mathrm{Ext}}(\boldsymbol{r}) \rho(\boldsymbol{r}) \quad (2.4)$$

where the functional F is defined as

$$F[\tilde{\rho}] = \left\langle \psi_{\tilde{\rho}} \right| \hat{\mathrm{T}} + \hat{\mathrm{V}}_{\mathrm{EE}} \left| \psi_{\tilde{\rho}} \right\rangle \tag{2.5}$$

where $|\psi_{\tilde{\rho}}\rangle$ is the ground state corresponding to the electron density $\tilde{\rho}$. Let ρ be the ground state density, so that $E_0 = E_{\mathrm{Trial}}[\rho]$. We have then for every $\tilde{\rho} \neq \rho$ that

$$E_0 < E_{\mathrm{Trial}}[\tilde{\rho}]$$

In other words, the energy functional is minimized for the ground state density.

Proof From the variational principle we have that

$$E_0 = \left\langle \psi_{\rho} \right| \hat{\mathrm{H}} \left| \psi_{\rho} \right\rangle \leq \left\langle \psi_{\tilde{\rho}} \right| \hat{\mathrm{H}} \left| \psi_{\tilde{\rho}} \right\rangle = E_{\mathrm{Trial}}[\tilde{\rho}]$$

which proves the theorem.

It is now possible to restate the variational principle in terms of the functionals of the density. Variations of the energy functional E_{Trial}, subject to the constraint of electron number conservation, must vanish when varying the electron density ρ around the ground state density ρ_0

$$\delta \left\{ E_{\mathrm{Trial}}[\rho] - \mu \left(\int \mathrm{d}\boldsymbol{r} \rho(\boldsymbol{r}) - N \right) \right\} = 0$$

where μ is the chemical potential, playing the role of the Lagrange multiplier for the electron number constraint. Taking the functional derivative we obtain

$$\left\{ \frac{\delta E_{\mathrm{Trial}}[\rho]}{\delta \rho} - \mu \right\} \delta\rho = \left\{ v_{\mathrm{Ext}}(\boldsymbol{r}) + \frac{\delta F[\rho]}{\delta \rho} + \mu \right\} \delta\rho = 0$$

where $\delta\rho = \rho - \rho_0$ are electron density variations. Since the variations $\delta\rho$ are arbitrary, the term inside the bracket must be zero, which gives us the generalized Thomas-Fermi equation

$$v_{\mathrm{Ext}}(\boldsymbol{r}) + \frac{\delta F[\rho]}{\delta \rho} + \mu = 0 \tag{2.6}$$

The only term that depends on electron density is the second term. Moreover, the

second term depends *only* on the electron density since the functional F, as defined in eq. (2.5), depends only on the electron density. This means, in principle, that this equation can be solved for the density ρ. However, this is not practically feasible since the form of the universal functional is unknown and only approximations are available.

2.2 General Form of The Density Functional

In eq. (2.3), the expectation value of the single-electron local observable is written with the help of the electron density. This expression is a special case of the following equation

$$O = \mathrm{Tr}\hat{\mathrm{O}}\hat{\rho} = \mathrm{Tr}\left(\sum_i w_i \hat{\mathrm{O}}|\psi_i\rangle\langle\psi_i|\right)$$

where $\hat{\rho}$ is the density matrix in the mixed state with the weights w_i corresponding to the pure states $|\psi_i\rangle$. When the coordinate representation is employed, this expression becomes

$$O = \int \mathrm{d}\boldsymbol{r}_1^1..\mathrm{d}\boldsymbol{r}_N^1\mathrm{d}\boldsymbol{r}_2^2..\mathrm{d}\boldsymbol{r}_N^2\hat{\mathrm{O}}(\boldsymbol{r}_1^1,..,\boldsymbol{r}_N^1;\boldsymbol{r}_1^2,..,\boldsymbol{r}_N^2)\rho_N(\boldsymbol{r}_1^2,..,\boldsymbol{r}_N^2;\boldsymbol{r}_1^1,..,\boldsymbol{r}_N^1)$$

Since the electronic Hamiltonian $\hat{\mathrm{H}}_\mathrm{E}$ contains only single and two-electron terms, we can make some simplifications. Let us consider the two particle observable $\hat{\mathrm{O}}_2$ whose matrix elements are $\hat{\mathrm{O}}_2(\boldsymbol{r}_1^1,\boldsymbol{r}_2^1;\boldsymbol{r}_1^2,\boldsymbol{r}_2^2)$. The expectation value is

$$O_2 = \int \mathrm{d}\boldsymbol{r}_1^1\mathrm{d}\boldsymbol{r}_2^1\mathrm{d}\boldsymbol{r}_1^2\mathrm{d}\boldsymbol{r}_2^2\hat{\mathrm{O}}_2(\boldsymbol{r}_1^1,\boldsymbol{r}_2^1;\boldsymbol{r}_1^2,\boldsymbol{r}_2^2)\int \mathrm{d}\boldsymbol{r}_3^1..\mathrm{d}\boldsymbol{r}_N^1\mathrm{d}\boldsymbol{r}_3^2..\mathrm{d}\boldsymbol{r}_N^2\rho_N(\boldsymbol{r}_1^2,..,\boldsymbol{r}_N^2;\boldsymbol{r}_1^1,..,\boldsymbol{r}_N^1) = \int \mathrm{d}\boldsymbol{r}_1^1\mathrm{d}\boldsymbol{r}_2^1\mathrm{d}\boldsymbol{r}_1^2\mathrm{d}\boldsymbol{r}_2^2\hat{\mathrm{O}}_2(\boldsymbol{r}_1^1,\boldsymbol{r}_2^1;\boldsymbol{r}_1^2,\boldsymbol{r}_2^2)\rho_2(\boldsymbol{r}_1^2,\boldsymbol{r}_2^2;\boldsymbol{r}_1^1,\boldsymbol{r}_2^1)$$

Here the two particle density matrix ρ_2 is introduced

$$\rho_2(\boldsymbol{r}_1^1,\boldsymbol{r}_2^1;\boldsymbol{r}_1^2,\boldsymbol{r}_2^2) = \int \mathrm{d}\boldsymbol{r}_3^1..\mathrm{d}\boldsymbol{r}_N^1\mathrm{d}\boldsymbol{r}_3^2..\mathrm{d}\boldsymbol{r}_N^2\rho_N(\boldsymbol{r}_1^1,..,\boldsymbol{r}_N^1;\boldsymbol{r}_1^2,..,\boldsymbol{r}_N^2)$$

If we proceed in the same manner for the single particle observable $\hat{\mathrm{O}}_1$ we will arrive at the result for the expectation value

$$O_1 = \int \mathrm{d}\boldsymbol{r}_1^1 \mathrm{d}\boldsymbol{r}_1^2 \hat{\mathrm{O}}_1(\boldsymbol{r}_1^1;\boldsymbol{r}_1^2) \int \mathrm{d}\boldsymbol{r}_2^1..\mathrm{d}\boldsymbol{r}_N^1 \mathrm{d}\boldsymbol{r}_2^2..\mathrm{d}\boldsymbol{r}_N^2 \rho_N(\boldsymbol{r}_1^2,..,\boldsymbol{r}_N^2;\boldsymbol{r}_1^1,..,\boldsymbol{r}_N^1) = \int \mathrm{d}\boldsymbol{r}_1^1 \mathrm{d}\boldsymbol{r}_1^2 \hat{\mathrm{O}}_1(\boldsymbol{r}_1^1;\boldsymbol{r}_1^2)\rho_1(\boldsymbol{r}_1^2 2;\boldsymbol{r}_1^1)$$

where the single particle density matrix

$$\rho_1(\boldsymbol{r}_1^1;\boldsymbol{r}_1^2) = \int \mathrm{d}\boldsymbol{r}_2^1..\mathrm{d}\boldsymbol{r}_N^1 \mathrm{d}\boldsymbol{r}_2^2..\mathrm{d}\boldsymbol{r}_N^2 \rho_N(\boldsymbol{r}_1^1,..,\boldsymbol{r}_N^1;\boldsymbol{r}_1^2,..,\boldsymbol{r}_N^2)$$

is introduced. We note here, that the diagonal elements of the single particle density matrix are equal to the electron density $\rho_1(\boldsymbol{r};\boldsymbol{r}) = \rho(\boldsymbol{r})$. Also, we can use the fact that $\hat{\mathrm{V}}_{\mathrm{Ext}}$ and $\hat{\mathrm{V}}_{\mathrm{EE}}$ are diagonal in the coordinate representation allowing us to deal only with the electron density $\rho(\boldsymbol{r})$ and the diagonal elements of the two particle density matrix $\rho_2(\boldsymbol{r}_1,\boldsymbol{r}_2) = \rho_2(\boldsymbol{r}_1,\boldsymbol{r}_2;\boldsymbol{r}_1,\boldsymbol{r}_2)$ respectively.

We can now attempt to find the form of the energy functional $E[\rho]$. The electronic kinetic energy expectation value is given by

$$T = \sum_{\alpha=1}^{N} \frac{1}{2m} \int \mathrm{d}\boldsymbol{r}_1^1 \mathrm{d}\boldsymbol{r}_1^2 \hat{\mathbf{p}}_\alpha^2(\boldsymbol{r}_1^1;\boldsymbol{r}_1^2)\rho_1(\boldsymbol{r}_1^2;\boldsymbol{r}_1^1) = -\frac{\hbar^2}{2m} \int \mathrm{d}\boldsymbol{r}_1^1 \left[\frac{\partial^2}{\partial(\boldsymbol{r}_1^1)^2}\rho_1(\boldsymbol{r}_1^1;\boldsymbol{r}_1^2)\right]_{\boldsymbol{r}_1^1=\boldsymbol{r}_1^2}$$

The expectation value of the external potential is obviously

$$V_{\mathrm{Ext}} = -\frac{Ze^2}{4\pi\varepsilon_0} \sum_{n=1}^{N} \int \mathrm{d}\boldsymbol{r} \frac{\rho(\boldsymbol{r})}{|\boldsymbol{R}_n - \boldsymbol{r}|}$$

and finally, the expectation value of the electron-electron interaction is

$$V_{\mathrm{EE}} = \frac{e^2}{8\pi\varepsilon_0} \int \mathrm{d}\boldsymbol{r}_1 \mathrm{d}\boldsymbol{r}_2 \frac{\rho_2(\boldsymbol{r}_1,\boldsymbol{r}_2)}{|\boldsymbol{r}_1 - \boldsymbol{r}_2|}$$

The external potential is readily cast as a functional of the electron density. However, the kinetic energy and the electron-electron interaction assume a more complicated form from which the form of the density functional is not apparent.

We can express the two particle density ρ_2 in terms of the electron density as $\rho_2(\boldsymbol{r}_1,\boldsymbol{r}_2) = \rho(\boldsymbol{r}_1)\rho(\boldsymbol{r}_2)g(\boldsymbol{r}_1,\boldsymbol{r}_2)$. Here we have introduced the two particle correlation function g which tells us how the electron density located at $\boldsymbol{r}_1$ affects the electron density located at $\boldsymbol{r}_2$. Obviously, $0 < g(\boldsymbol{r}_1,\boldsymbol{r}_2) < 1$ and we expect that g increases with the distance

$|\boldsymbol{r}_1 - \boldsymbol{r}_2|$ and that it approaches unity as this distance goes to infinity since the electron densities at $\boldsymbol{r}_1$ and $\boldsymbol{r}_2$ become independent for very large separations. Because of this, it is useful to split the electron-electron interaction into two terms

$$V_{\mathrm{EE}} = V_{\mathrm{EE}}^{\mathrm{H}} + V_{\mathrm{EE}}^{\mathrm{XC}} = \frac{e^2}{8\pi\varepsilon_0}\int \mathrm{d}\boldsymbol{r}_1\mathrm{d}\boldsymbol{r}_2 \frac{\rho(\boldsymbol{r}_1)\rho(\boldsymbol{r}_2)}{|\boldsymbol{r}_1 - \boldsymbol{r}_2|} + \frac{e^2}{8\pi\varepsilon_0}\int \mathrm{d}\boldsymbol{r}_1\mathrm{d}\boldsymbol{r}_2 \frac{\rho(\boldsymbol{r}_1)\rho(\boldsymbol{r}_2)}{|\boldsymbol{r}_1 - \boldsymbol{r}_2|}\left[g(\boldsymbol{r}_1, \boldsymbol{r}_2) - 1\right]$$

The first term is known as the Hartree term and is dominant for large separations, while the second term, known as the exchange-correlation term becomes important for small separations. The Hartree term describes the system of uncorrelated electrons interacting via the Coulomb interaction. It is straightforward to write it as a density functional $V_{\mathrm{EE}}^{\mathrm{H}}[\rho] = \int \mathrm{d}\boldsymbol{r} v_{\mathrm{H}}(\boldsymbol{r})\rho(\boldsymbol{r})$, where the $v_{\mathrm{H}}(\boldsymbol{r})$ is

$$v_{\mathrm{H}}(\boldsymbol{r}) = \frac{e^2}{4\pi\varepsilon_0}\int \mathrm{d}\boldsymbol{r}' \frac{\rho(\boldsymbol{r}')}{|\boldsymbol{r} - \boldsymbol{r}'|}$$

Therefore, for systems where the electrons are weakly interacting, it is still possible to obtain some sensible results without the inclusion of the exchange correlation term.

Without the exchange correlation term, electrons would not behave as Fermions since there is nothing in the energy functional to enforce the Pauli exclusion principle. The Pauli exclusion principle is enforced through the exchange interaction which is the main contribution to the exchange-correlation term.

With only the exchange interaction, it would be forbidden for the electrons with the same spins to occupy the same position, which means that $g(\boldsymbol{r}, \boldsymbol{r}) = 1/2$, because only up to two electrons with different spins are allowed to be located at $\boldsymbol{r}$. The effects of the exchange interaction are equivalent to writing the many-electron state as a Slater determinant

$$\phi(\boldsymbol{r}_1, .., \boldsymbol{r}_N) = \begin{vmatrix} \varphi_1(\boldsymbol{r}_1) & \varphi_2(\boldsymbol{r}_1) & \dots & \varphi_N(\boldsymbol{r}_1) \\ \varphi_1(\boldsymbol{r}_2) & \varphi_2(\boldsymbol{r}_2) & .. & \varphi_N(\boldsymbol{r}_2) \\ \vdots & \vdots & \ddots & \vdots \\ \varphi_1(\boldsymbol{r}_N) & \varphi_2(\boldsymbol{r}_N) & .. & \varphi_N(\boldsymbol{r}_N) \end{vmatrix}_{\otimes}$$

where $\varphi_i(\boldsymbol{r})$ are the single electron basis states. This results in the fully antisymmetric many-electron state which guarantees the Pauli exclusion principle. This is known as the

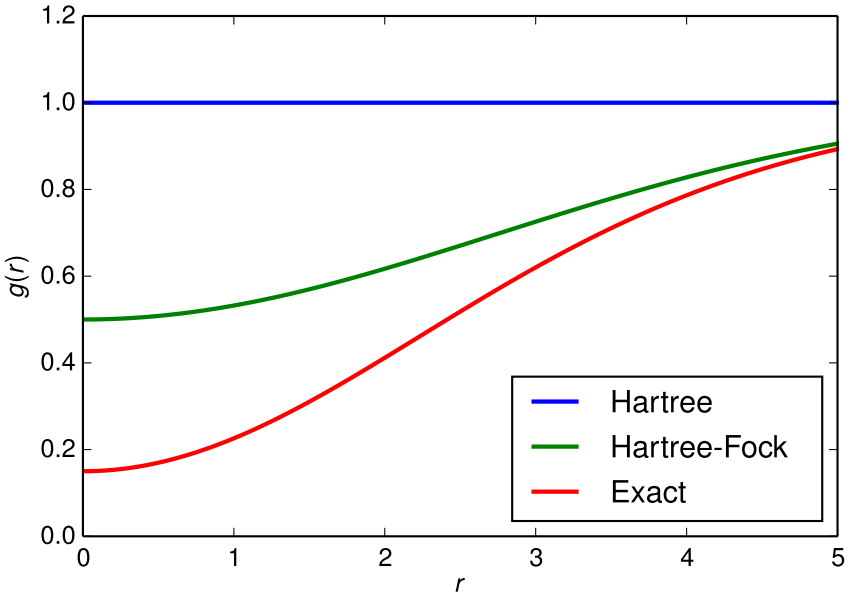

FIGURE 2.1: Pair correlation function within different approximations [1].

Hartree-Fock approximation. Within this approximation, the pair correlation function is bounded by 1/2 from below.

Figure 2.1 shows the schematic behavior of the pair correlation function $g(\boldsymbol{r}_1, \boldsymbol{r}_2)$ as a function of the separation $r = |\boldsymbol{r}_1 - \boldsymbol{r}_2|$ within different approximations. In the Hartree approximation g is constant and equal to unity. Within the Hartree-Fock approximation, it goes down with distance, and reaches 1/2 for $r = 0$. And finally inclusion of the correlations, reduces its value further.

2.3 Kohn-Sham Equations

In the previous section we have outlined the main obstacles one encounters when trying to devise the energy functional. To make the Density Functional Theory a useful computational tool, an ansatz was devised to circumvent the hard problem of the universal functional[7]. The basic idea is to replace the interacting electrons described by eq. (1.11), by a system of fictitious non-interacting electrons with identical density. In other words, instead of considering the single many-body wavefunction $\psi(\boldsymbol{r}_1, .., \boldsymbol{r}_N)$, we have to consider N single-electron wavefunctions $\phi_i(\boldsymbol{r})$ such that

$$\rho(\boldsymbol{r}) = \psi^*(\boldsymbol{r}_1, .., \boldsymbol{r}_N)\psi(\boldsymbol{r}_2, .., \boldsymbol{r}_N) = \sum_{i=1}^{N} \phi_i^*(\boldsymbol{r})\phi_i(\boldsymbol{r})$$

With this ansatz, we can write the expectation value of the kinetic energy as $T =$

$T_S + T - T_S = T_S + T_{XC}$, where the single-electron density kinetic energy T_S was introduced

$$T_S = \sum_{i=1}^{N} \frac{\hbar^2}{2m} \int \mathrm{d}\boldsymbol{r} \phi_i^*(\boldsymbol{r}) \nabla^2 \phi_i(\boldsymbol{r})$$

and the term T_{XC} measures the deviation of the single electron kinetic energy from the exact value. When we put this into the energy functional (2.4) we arrive at

$$E[\phi] = \sum_{i=1}^{N} \int \mathrm{d}\boldsymbol{r} \left[-\frac{\hbar^2}{2m} \phi_i^*(\boldsymbol{r}) \nabla^2 \phi_i(\boldsymbol{r}) + |\phi_i(\boldsymbol{r})|^2 v_{Ext}(\boldsymbol{r}) \right] + T_{XC}[\phi] + V_{EE}[\phi] =$$
$$\sum_{i=1}^{N} \int \mathrm{d}\boldsymbol{r} \left\{ -\frac{\hbar^2}{2m} \phi_i^*(\boldsymbol{r}) \nabla^2 \phi_i(\boldsymbol{r}) + |\phi_i(\boldsymbol{r})|^2 \left[v_{Ext}(\boldsymbol{r}) + v_H(\boldsymbol{r}) \right] \right\} + E_{XC}[\phi]$$

where we consider now the energy to be a functional of wavefunctions ϕ_i. Here, the electron-electron interaction was split into the Hartree and the exchange-correlation term, and then the exchange-correlation energy $E_{XC} = T_{XC} + V_{EE}^{XC}$ was introduced. Following the variational principle, we require that when varying ϕ_i in the ground state, the variations of energy vanish. We also need to impose the condition that wavefunctions ϕ_i are normalized to unity, in order to have the electron density normalized to the number of electrons. Since the energy functional $E[\phi]$ contains both the wavefunctions ϕ_i and their complex-conjugates, we can equally consider both the variations $\delta\phi_i$ and $\delta\phi_i^*$. The choice is up to our convenience, since the resulting variational equations will just be complex-conjugates of each other. We thus choose to vary ϕ_i^* which results in

$$\delta E[\phi^*] = \delta \left\{ -\sum_{i=1}^{N} \frac{\hbar^2}{2m} \int \mathrm{d}\boldsymbol{r} \left[\phi_i^*(\boldsymbol{r}) \nabla^2 \phi_i(\boldsymbol{r}) + |\phi_i(\boldsymbol{r})|^2 (v_H(\boldsymbol{r}) + v_{Ext}(\boldsymbol{r})) \right] + \right.$$
$$\left. E_{XC}[\phi] + \sum_{i=1}^{N} \varepsilon_i \left(1 - \int \mathrm{d}\boldsymbol{r} |\phi_i(\boldsymbol{r})|^2 \right) \right\} =$$
$$\sum_{i=1}^{N} \left\{ -\frac{\hbar^2}{2m} \nabla^2 \phi_i(\boldsymbol{r}) + [v_H(\boldsymbol{r}) + v_{Ext}(\boldsymbol{r})] \phi_i(\boldsymbol{r}) + \frac{\delta E_{XC}[\rho]}{\delta \rho(\boldsymbol{r})} \phi_i(\boldsymbol{r}) - \varepsilon_i \phi_i(\boldsymbol{r}) \right\} \delta\phi_i^*(\boldsymbol{r}) = 0$$

Since variations $\delta\phi_i^*$ are arbitrary and independent, the term within the brackets has to vanish, resulting in

$$\left[-\frac{\hbar^2}{2m} \nabla^2 + v_H(\boldsymbol{r}) + v_{Ext}(\boldsymbol{r}) + V_{XC}(\boldsymbol{r}) \right] \phi_i(\boldsymbol{r}) = \varepsilon_i \phi_i(\boldsymbol{r}) \tag{2.7}$$

where $V_{\mathrm{XC}}(\boldsymbol{r}) = \delta E_{\mathrm{XC}}[\rho]/\delta\rho(\boldsymbol{r})$ is the exchange-correlation potential. The equations (2.7) are known as Kohn-Sham equations and they are the counterpart to the previously mentioned Thomas-Fermi equation (2.6) . They have the form of the eigenproblem of the Kohn-Sham Hamiltonian

$$\hat{\mathrm{H}}_{\mathrm{KS}}\phi_i(\boldsymbol{r}_i) = \varepsilon_i\phi_i(\boldsymbol{r}) \tag{2.8}$$

where

$$\hat{\mathrm{H}}_{\mathrm{KS}} = -\frac{\hbar^2}{2m}\nabla^2 + v_{\mathrm{H}}(\boldsymbol{r}) + v_{\mathrm{Ext}}(\boldsymbol{r}) + V_{\mathrm{XC}}(\boldsymbol{r})$$

The Kohn-Sham approach reduces the Density Functional approach to the familiar single-electron stationary Schrödinger equation (2.7). It is tempting to try to interpret the Lagrange multipliers ε_i as the energy levels and ϕ_i as the single electron orbitals. The DFT-Koopmans' theorem [8] states that the first ionization energy of the system of N electrons is $I = -\varepsilon_{\mathrm{HOMO}}$, where $\varepsilon_{\mathrm{HOMO}}$ corresponds to the highest occupied Kohn-Sham state ϕ_{HOMO}. This means that occupation of state ϕ_i can be considered equivalent to the addition of one non-interacting electron into the orbital ϕ_i with the energy ε_i. Owing to this statement, attribution of the physical significance to the ϕ_i and ε_i is possible in the aforementioned sense, but one always has to bear in mind that the single-electron picture of the Kohn-Sham approach is fundamentally incorrect and that in general, for the many-body system, the concept of the orbital and its energy level, is not well defined.

Up to this point, equations (2.7) are exact. The problem of the universal functional, mentioned earlier, has been reduced to the exchange correlation potential. In order to undertake any practical computation, some approximations for the V_{XC} have to be employed. The basic starting point is to assume that the exchange-correlation energy functional E_{XC} can be written as

$$E_{\mathrm{XC}}[\rho] = \int \mathrm{d}\boldsymbol{r}\varepsilon_{\mathrm{XC}}(\rho)\rho(\boldsymbol{r})$$

where $\varepsilon_{\mathrm{XC}}(\rho)$ is the local exchange-correlation energy density of the electron system of the uniform electron density ρ. This is known as the local density approximation. The resulting exchange-correlation potential is

$$V_{\mathrm{XC}}(\boldsymbol{r}) = \frac{\delta E_{\mathrm{XC}}[\rho]}{\delta \rho(\boldsymbol{r})} = \varepsilon_{\mathrm{XC}}(\rho(\boldsymbol{r})) + \rho(\boldsymbol{r}) \frac{\partial \varepsilon_{\mathrm{XC}}(\rho(\boldsymbol{r}))}{\partial \rho(\boldsymbol{r})}$$

The exchange contribution to $\varepsilon_{\mathrm{XC}}(\rho)$ is known[9] within the local density approximation. To estimate the correlation contribution other many-body methods, such as Quantum Monte Carlo methods can be employed.

The local density approximation performs well in the systems where variations of the electron density are not too large. It results in more uniform electron density and, as a consequence, overestimates the strength of the chemical bonding. To alleviate this deficiencies, the more accurate Generalized Gradient Approximation can be used. With Generalized Gradient Approximation, the exchange correlation energy is assumed to be of the form

$$E_{\mathrm{XC}}[\rho] = \int \mathrm{d}\boldsymbol{r} \left\{ \varepsilon_{\mathrm{XC}}(\rho)\rho(\boldsymbol{r}) + f_{\mathrm{XC}}[\rho, |\nabla \rho|] \right\}$$

where variations in the electron density are taken into account up to first order.

2.4 Spin-Polarized Density Functional Theory

It is apparent that in all of the previous considerations, the spin is nowhere to be found explicitly. The main reason is that from the very beginning we have dealt with the non-relativistic electron Hamiltonian, which is independent from the spin degrees of freedom. If we want to introduce the spin into the equations we have to do so explicitly, either in the electron density, or the Kohn-Sham wavefunctions.

In the context of the Density Functional Theory, this can be achieved by splitting the electron density into spin-up and spin-down components $\rho(\boldsymbol{r}) = \rho_{\downarrow}(\boldsymbol{r}) + \rho_{\uparrow}(\boldsymbol{r})$. In the context of the Kohn-Sham equations, this means that the densities are

$$\rho_{\sigma}(\boldsymbol{r}) = \sum_{i=1}^{N} |\phi_{i,\sigma}(\boldsymbol{r})|^2$$

where $\sigma = \downarrow, \uparrow$. Instead of using ρ_{σ} it is more common to use total electron density $\rho(\boldsymbol{r})$ and the magnetization density $m(\boldsymbol{r}) = \rho_{\uparrow}(\boldsymbol{r}) - \rho_{\downarrow}(\boldsymbol{r})$. The only alteration that needs to be made to the Kohn-Sham equations is to take into account that they are two-component, and that the exchange correlation potential depends on both the electron density and the magnetization density.

This kind of formulation assumes that all electrons have the same spin quantization axis which means that non-collinear magnetism cannot be treated. For a full three-dimensional formulation, it is necessary to employ the spinor representation of the density defined as

$$\rho_{\alpha\beta}(\boldsymbol{r}) = \frac{1}{2}\rho(\boldsymbol{r}) + \frac{1}{2}\sum_i m_i(\boldsymbol{r})\sigma^i_{\alpha\beta}$$

where $i = x, y, z$ are Cartesian components, m_i are the components of the three-dimensional magnetization and $\hat{\sigma}^i$ are Pauli matrices. Indices α and β enumerate spinor components.

2.5 Self-consistent Cycle

The non-relativistic Density Functional Theory framework is now complete. We have the Kohn-Sham equations (2.7) and we have assumed some approximate form of the exchange-correlation potential $V_{\mathrm{XC}}(\boldsymbol{r})$. The remaining question is how to solve the Kohn-Sham equations since in the Kohn-Sham eigenproblem (2.8), the Hamiltonian $\hat{\mathrm{H}}_{\mathrm{KS}}$ depends on its eigenvectors through dependence on the electron density.

This issue can be resolved by using some initial assumption for the wavefunctions ϕ_i^0 and then calculating the Hamiltonian $\hat{\mathrm{H}}^0_{\mathrm{KS}}$. This Hamiltonian is then diagonalized, and a new set of wavefunctions ϕ_i^1 and eigenvalues ε_i^1 is obtained. The Hamiltonian $\hat{\mathrm{H}}^1_{\mathrm{KS}}$ is computed from ϕ_i^1 and the cycle is repeated until the wavefunctions ϕ_i^n and the eigenvalues ε_i^n stop changing appreciably from one step of the cycle to the next one. This is schematically shown on figure 2.2. However, there is no way to guarantee that given any set of initial wavefunctions ϕ_i^0, the self-consistent cycle is going to converge.

2.6 Summary

In this chapter an overview of Density Functional Theory was given. Starting from the Hohenberg-Kohn theorems and their notion that the electron density as the variable that uniquely determines the external potential acting on the many-electron system, the energy expectation value was expressed as a density functional.

Further examination of the energy functional shows that the kinetic energy functional and the exchange-correlation part of the electron-electron interaction functional have

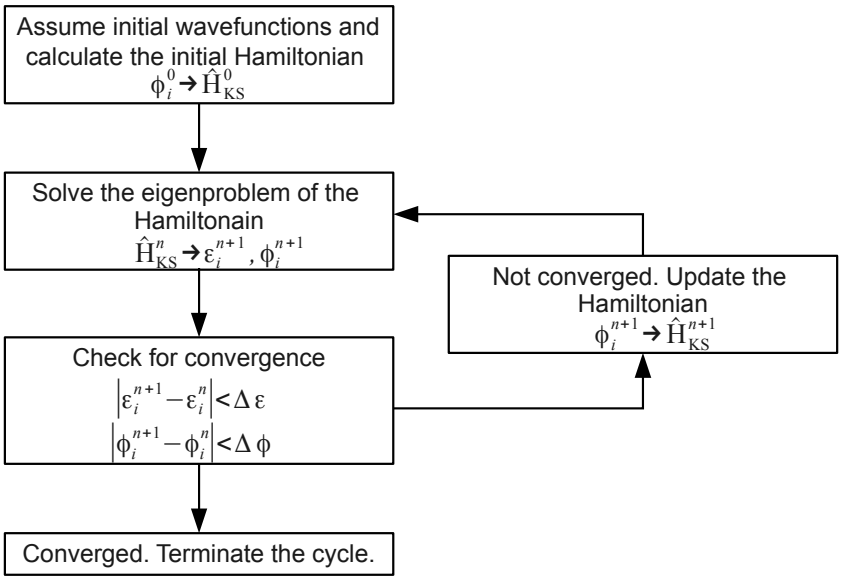

FIGURE 2.2: Schematic outline of the basic self-consistent cycle

highly non-trivial form. In order to work around this difficulty, the electron density was parametrized in terms of a fictitious system of non-interacting electrons, allowing us to write explicitly most of the terms in the energy functional. Everything that remained unknown was consolidated into the exchange correlation potential.

Owing to the single-electron parametrization, and by making use of the variational principle, the problem of the energy functional miminzation can be cast into a familiar form of the eigenproblem of the effective single-electron Hamiltonian. As a result, we are left with a solution in terms of eigenfunctions and eigenvalues which can be interpreted as single-electron orbitals and corresponding energy levels.

And finally, a practical use of this approach can be made by self-consistently solving the Kohn-Sham equations.

Chapter 3

Basis for Solving the Kohn-Sham Equations

In order to practically solve the Kohn-Sham equations it is necessary to specify a set of basis states. Let the basis set be composed of states $|i\rangle$, where $i = 1, .., N$. The Kohn-Sham Hamiltonian is then represented by the following matrix

$$\hat{\mathrm{H}}_{\mathrm{KS}} = \begin{bmatrix} \left\langle 1 \middle| \hat{\mathrm{H}}_{KS} \middle| 1 \right\rangle & \left\langle 1 \middle| \hat{\mathrm{H}}_{KS} \middle| 2 \right\rangle & \dots & \left\langle 1 \middle| \hat{\mathrm{H}}_{KS} \middle| N \right\rangle \\ \left\langle 2 \middle| \hat{\mathrm{H}}_{KS} \middle| 1 \right\rangle & \left\langle 2 \middle| \hat{\mathrm{H}}_{KS} \middle| 2 \right\rangle & \dots & \left\langle 2 \middle| \hat{\mathrm{H}}_{KS} \middle| N \right\rangle \\ \vdots & \vdots & \ddots & \vdots \\ \left\langle N \middle| \hat{\mathrm{H}}_{KS} \middle| 1 \right\rangle & \left\langle N \middle| \hat{\mathrm{H}}_{KS} \middle| 2 \right\rangle & \dots & \left\langle N \middle| \hat{\mathrm{H}}_{KS} \middle| N \right\rangle \end{bmatrix}$$

The solutions to the Kohn-Sham equations are then given by eigenvalues and eigenvectors of this matrix.

The choice of the appropriate basis is dictated by numerical convenience of application to the particular problem, especially trying to keep N as small as possible.

In this context, we can consider two types of basis states. The first type uses localized orbitals, such as Gaussians or atomic-like orbitals, and is commonly used for molecules. The second major group uses extended wavefunctions, most frequently plane waves, and is commonly used for periodic systems. The major problem with the second approach is that the extended basis is ill suited in the vicinity of atomic nuclei, because expansion of rapidly oscillating wavefunctions, close to the nuclei, requires large number of slowly oscillating extended basis wavefunctions. This requires the use of large basis sets, which in turn necessitates diagonalization of large matrices.

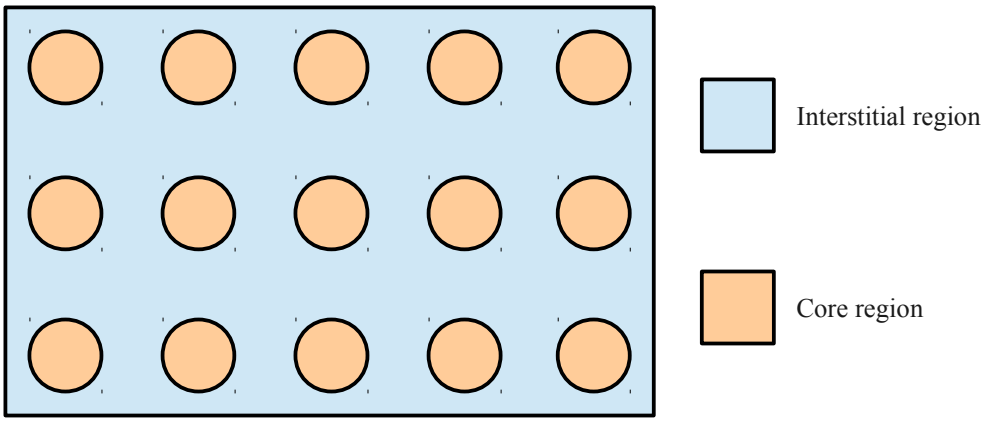

FIGURE 3.1: Schematic view of space subdivision into interstitial and core regions. The core region is composed of non-overlapping atom-centered spheres

There are various ways to solve this problem. The usual one is to divide the computational volume into an interstitial region, further away from the nuclei, and the non-overlapping spherical core regions close to the nuclei (Figure 3.1) and then treat those regions separately in their respective most convenient computational fashions.

This subdivision is the basis of the Projector Augmented Wave method which will be presented here and which was used for most of the calculations performed in this thesis.

A good description of electrons in crystals can also be obtained with a careful use of localized basis, as in the Full Potential Local Orbital method, which will also be outlined. One of the benefits of this method is that it affords simple access to localized properties as well as a straightforward construction of projective Wannier functions. Tis will be shown at the end of the chapter.

3.1 Projector Augmented Wave Method

The Projector Augmented Wave[10] method is a generalization of the earlier Pseudopotential method. The basic idea is to decompose the wavefunction, in this context called the all-electron wavefunction, into a smooth component, called the pseudo-wavefunction, which is identical to the all-electron wavefunction in the interstitial region and atomic-like wavefunction corrections in the core region, called augmentation sphere.

$$|\psi\rangle = |\tilde{\psi}\rangle + |\psi\rangle - |\tilde{\psi}\rangle \tag{3.1}$$

This decomposition is graphically shown in Figure 3.2 which shows the all-electron

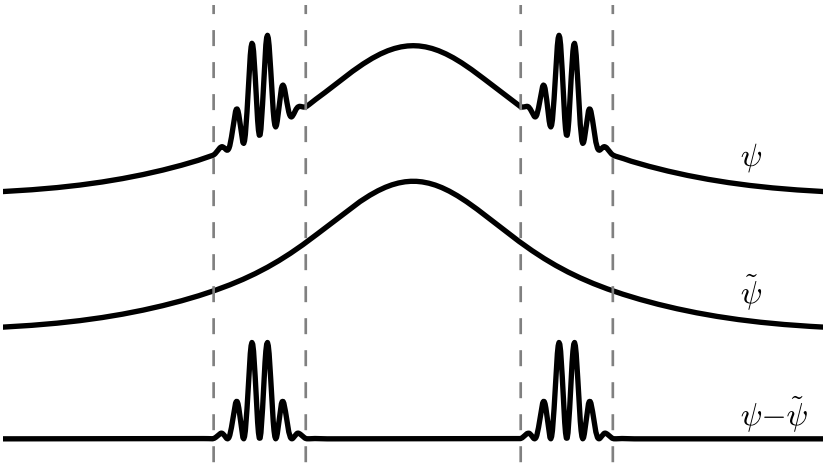

FIGURE 3.2: Panel a) shows all electron wavefunction ψ. Panel b) shows pseudo-wavefunction $\tilde{\psi}$ and panel c) shows the difference $\psi - \tilde{\psi}$.

wavefuntion ψ in the vicinity of two atoms. Pseudo-wavefunction $\tilde{\psi}$ is chosen in such a way that it is identical to ψ in the interstitial region. What is left as a difference in the augmentation sphere $\psi - \tilde{\psi}$ looks like orbitals of two isolated atoms.

Because the difference $\psi - \tilde{\psi}$ is different from zero only within the augmentation spheres, eq. (3.1) can be written as

$$|\psi\rangle = |\tilde{\psi}\rangle + \sum_a (|\psi^a\rangle - |\tilde{\psi}^a\rangle) \tag{3.2}$$

where $|\psi^a\rangle$ and $|\tilde{\psi}^a\rangle$ represent wavefunctions in the core region a and the sum runs over all augmentation spheres. An operator $\hat{\mathcal{T}}$, can be defined based on (3.2) as

$$|\psi\rangle = \hat{\mathcal{T}}|\tilde{\psi}\rangle = \left(1 + \sum_a \hat{\mathcal{T}}^a\right)|\tilde{\psi}\rangle \tag{3.3}$$

The operators $\hat{\mathcal{T}}^a$ have no effect outside of their respective augmentation spheres. The Kohn-Sham equations

$$\hat{\mathrm{H}}_{\mathrm{KS}}|\psi_i\rangle = \varepsilon_i|\psi_i\rangle$$

can now be written as

$$\hat{\mathcal{T}}^\dagger \hat{\mathrm{H}}_{\mathrm{KS}} \hat{\mathcal{T}}|\tilde{\psi}\rangle = \varepsilon \hat{\mathcal{T}}^\dagger \hat{\mathcal{T}}|\tilde{\psi}\rangle$$

If we introduce the pseudo-Hamiltonian $\hat{\tilde{\mathrm{H}}}_{\mathrm{KS}} = \hat{\mathcal{T}}^{\dagger}\hat{\mathrm{H}}_{\mathrm{KS}}\hat{\mathcal{T}}$ and the overlap $\hat{\mathrm{S}} = \hat{\mathcal{T}}^{\dagger}\hat{\mathcal{T}}$, the Kohn-Sham equations take the form of a generalized eigenproblem

$$\hat{\tilde{\mathrm{H}}}_{\mathrm{KS}}|\tilde{\psi}\rangle = \varepsilon\hat{\mathrm{S}}|\tilde{\psi}\rangle$$

where the matrix representing the pseudo-Hamiltonan $\hat{\tilde{\mathrm{H}}}_{\mathrm{KS}}$ is much smaller than the one representing $\hat{\mathrm{H}}_{\mathrm{KS}}$.

The task at hand is to find a general form for the transformation operators $\hat{\mathcal{T}}^a$. To do so, within the augmentation sphere, we expand the all-electron wavefunction into partial wavefunctions ϕ_i^a and then define the corresponding partial waves $\tilde{\phi}_i^a$ as

$$|\phi_i^a\rangle = (1 + \hat{\mathcal{T}}^a)|\tilde{\phi}_i^a\rangle$$

If we assume that partial wavefunctions form a complete basis within the augmentation sphere, we can write

$$|\tilde{\psi}^a\rangle = \sum_i P_i^a|\tilde{\phi}_i^a\rangle \tag{3.4}$$

For the all-electron partial wavefunctions, expansion with the same coefficients hold, since

$$|\psi^a\rangle = \hat{\mathcal{T}}|\tilde{\psi}^a\rangle = \hat{\mathcal{T}}\sum_i P_i^a|\tilde{\phi}_i^a\rangle = \sum_i P_i^a|\phi_i^a\rangle$$

We can now define the smooth projector wavefunctions $|\tilde{p}_i^a\rangle$ such that

$$P_i^a = \langle\tilde{p}_i^a|\tilde{\psi}^a\rangle \tag{3.5}$$

However, this has to be consistent with the expansion (3.4), implying that projector wavefunctions have to satisfy the following conditions

$$\begin{aligned} \sum_i |\tilde{\phi}_i^a\rangle\langle\tilde{p}_i^a| &= 1 \\ \langle\tilde{p}_i^a|\tilde{\phi}_j^a\rangle &= \delta_{ij} \end{aligned} \tag{3.6}$$

The first condition is obtained directly from eq. (3.4) when the projector definition (6.3) is inserted in place of P_i^a. The second condition is also obtained directly from (3.4) by requiring consistency in the limiting case when $|\tilde{\psi}^a\rangle \to |\tilde{\phi}_i^a\rangle$. It can be shown[10] that, given a set of linearly independent functions $|f_i^a\rangle$, the most general form of the projector satisfying (3.6) is given by

$$|\tilde{p}_i^a\rangle = \sum_j \left[\hat{\mathrm{F}}^{-1}\right]_{ij} |f_j^a\rangle$$

where $\hat{\mathrm{F}}$ is a matrix whose elements are given by

$$\left[\hat{\mathrm{F}}\right]_{ij} = \langle f_i^a | \tilde{\phi}_j^a \rangle$$

Thus, given any set of conveniently chosen functions f_i, it is possible to obtain projectors. Since we require projectors to be localized within the augmentation spheres, the functions f_i are chosen to be localized too.

We can now find the general form of the operator $\hat{\mathcal{T}}$. From eq. (3.1) it follows that

$$\hat{\mathcal{T}}^a |\tilde{\phi}_i^a\rangle = |\phi_i^a\rangle - |\tilde{\phi}_i^a\rangle$$

while from eq. (3.6) it follows that

$$\hat{\mathcal{T}}^a = \sum_i \hat{\mathcal{T}}^a |\tilde{\phi}_i^a\rangle\langle\tilde{p}_i^a|$$

By combining these two relations we conclude that

$$\hat{\mathcal{T}} = 1 + \sum_a \hat{\mathcal{T}}^a = 1 + \sum_a \sum_i (|\phi_i^a\rangle - |\tilde{\phi}_i^a\rangle)\langle\tilde{p}_i^a| \tag{3.7}$$

In this way, the transformation operator $\hat{\mathcal{T}}$ is expressed in terms of all-electron partial wavefunctions $|\phi_i^a\rangle$, partial pseudo wavefunctions $|\tilde{\phi}_i^a\rangle$ and the projectors $|\tilde{p}_i^a\rangle$. The projectors are subject to the conditions (3.6) and the all-electron and partial pseudo wavefunctions have to form a complete basis set within their respective augmentation sphere. All other remaining freedoms in choice are used to make computations converge as quick as possible.

For the all-electron partial waves, one usually chooses the solutions of the Schrödinger

equation of an isolated atom, while partial pseudo wavefunctions are chosen as any smooth continuation of all-electron wavefunctions into the augmentation sphere since they are identical by construction on the outside. For this purpose, Bessel functions, Gaussians or even polynomials of even power can be used[11].

3.2 Full Potential Local Orbital Method

The Full Potential Local Orbital method[12] solves the Kohn-Sham equations by employing a basis consisting of non-orthogonal overlapping atomic-like orbitals. Such orbitals can be constructed and manipulated in a computationally effective manner.

Let us consider a Bravais lattice composed of unit cells located at $\boldsymbol{R}_n$ with the basis $\boldsymbol{s}_\alpha$.The periodic crystal potential can be decomposed into a lattice sum of local non-spherical contributions

$$V(\boldsymbol{r}) = \sum_{n\alpha L} V_{\alpha L}(|\boldsymbol{r} - \boldsymbol{R}_n - \boldsymbol{s}_\alpha|) Y_L(\boldsymbol{r} - \boldsymbol{R}_n - \boldsymbol{s}_\alpha) \tag{3.8}$$

where $L = (l, m)$ is the composite angular momentum index denoting the angular momentum and its projection onto the quantization axis. This expansion is truncated at an angular momentum $L_{\max}$ and it can be shown[12] that the potential (3.8) converges to the correct periodic potential with increasing $L_{\max}$.

Localized atomic-like basis is composed of the states

$$\langle \boldsymbol{r}|n, \alpha, L\rangle = \psi^l_\alpha(|\boldsymbol{r} - \boldsymbol{R}_n - \boldsymbol{s}_\alpha|) Y_L(\boldsymbol{r} - \boldsymbol{R}_n - \boldsymbol{s}_\alpha) \tag{3.9}$$

which are a solution to the Schrödinger equation with the spherically symmetric potential

$$V^{\mathrm{at}}_\alpha(r) = \frac{1}{4\pi} \int \mathrm{d}\Omega V(\boldsymbol{r} - \boldsymbol{R}_n - \boldsymbol{s}_\alpha) + \frac{r}{r_0}^4 \tag{3.10}$$

which is composed of the spherically averaged crystal potential around the site $\boldsymbol{R}_n + \boldsymbol{s}_\alpha$ and the confining potential contained in the second term. The unit cell index n is dropped here since the potential will be the same for any other site $\boldsymbol{R}_m + \boldsymbol{s}_\alpha$ because of the translation symmetry. The role of the confining potential is to compress the atomic orbitals. Compressed atomic orbitals are higher in energy and more convenient for formation of the extended states. And finally, the extended states are given by the Bloch sum

$$|\boldsymbol{k}, i\rangle = \sum_{n\alpha L} e^{i\boldsymbol{k}\cdot(\boldsymbol{R}_n+\boldsymbol{s}_\alpha)} C^{\boldsymbol{k}i}_{L\alpha} |n, \alpha, L\rangle \tag{3.11}$$

Matrix elements of the Kohn-Sham equation $\hat{\mathrm{H}}|\boldsymbol{k}, i\rangle = \varepsilon_{\boldsymbol{k}i}|\boldsymbol{k}, i\rangle$ are then given by

$$\sum_{n\beta M} \left(\left\langle 0, \alpha, L \middle| \hat{\mathrm{H}} \middle| n, \beta, M \right\rangle - \langle 0, \alpha, L | n, \beta, M\rangle \varepsilon_{\boldsymbol{k}i} \right) C^{\boldsymbol{k}i}_{\beta M} e^{i\boldsymbol{k}\cdot(\boldsymbol{R}_n+\boldsymbol{s}_\alpha-\boldsymbol{s}_\beta)} = 0 \tag{3.12}$$

where translational invariance of scalar products and matrix elements was used. The Hamiltonian and overlap matrix elements can be read from (3.12) as

$$H^{LM}_{n,\alpha\beta} = \left\langle 0, \alpha, L \middle| \hat{\mathrm{H}} \middle| n, \beta, M \right\rangle$$
$$S^{LM}_{n,\alpha\beta} = \langle 0, \alpha, L | n, \beta, M\rangle$$

The matrix form of eq. (3.12) is

$$(\hat{\mathrm{H}} - \hat{\mathrm{S}}\hat{\mathrm{E}})\hat{\mathrm{C}} = 0 \tag{3.13}$$

where $\hat{\mathrm{C}}$ is a matrix whose elements are coefficients $C^{\boldsymbol{k}i}_{\beta M}$ and $\hat{\mathrm{E}}$ is diagonal matrix with eigenvalues $\varepsilon_{\boldsymbol{k}i}$ on the diagonal.

Localized atomic orbitals can be classified as core and valence orbitals, $|n, \alpha, L_c\rangle$ and $|n, \alpha, L_v\rangle$ respectively. The core orbitals are highly localized and are effectively under the influence of the spherically averaged potential (3.10), while the valence orbitals are affected by the full potential (3.8). Because the core orbitals are solution of the Schrödinger equation with the spherically symmetric potential, they will be orthonormal, and additionally they will be eigenstates of the Bloch Hamiltonian

$$\langle n, \alpha, L_c | m, \beta, M_c\rangle = \delta_{nm}\delta_{\alpha\beta}\delta_{L_cM_c} \tag{3.14}$$
$$\hat{\mathrm{H}}|n, \alpha, L_c\rangle = \varepsilon_{\alpha L_c}|n, \alpha, L_c\rangle \tag{3.15}$$

With this distinction the overlap matrix becomes

$$\hat{\mathrm{S}} = \begin{bmatrix} \hat{\mathrm{S}}_{cc} & \hat{\mathrm{S}}_{cv} \\ \hat{\mathrm{S}}_{vc} & \hat{\mathrm{S}}_{vv} \end{bmatrix}$$

where the matrix elements of the sub-blocks are given by

$$\begin{aligned}\left[\hat{\mathrm{S}}_{cc}\right]_{n,\alpha\beta}^{L_cM_c} &= \langle 0,\alpha,L_c|n,\beta,M_c\rangle = \delta_{0n}\delta_{\alpha\beta}\delta_{L_cM_c}\\ \left[\hat{\mathrm{S}}_{cv}\right]_{n,\alpha\beta}^{L_cM_v} &= \langle 0,\alpha,L_c|n,\beta,M_v\rangle = \left[\hat{\mathrm{S}}_{vc}^{\dagger}\right]_{n,\alpha\beta}^{L_vM_c}\\ \left[\hat{\mathrm{S}}_{vv}\right]_{n,\alpha\beta}^{L_vM_v} &= \langle 0,\alpha,L_v|n,\beta,M_v\rangle\end{aligned}$$

Core state properties (3.14) also simplify the form of the Hamiltonian, since the $\hat{\mathrm{H}}_{cc}$ block will be diagonal

$$\left[\hat{\mathrm{H}}_{cc}\right]_{n,\alpha\beta}^{L_cM_c} = \delta_{0n}\delta_{\alpha\beta}\delta_{L_cM_c}\varepsilon_{\alpha L_c} \tag{3.16}$$

and the $\hat{\mathrm{H}}_{cv}$ block can be written as

$$\begin{aligned}\left[\hat{\mathrm{H}}_{cv}\right]_{n,\alpha\beta}^{L_cM_v} = \left\langle 0,\alpha,L_c\right|\hat{\mathrm{H}}\left|n,\beta,M_v\right\rangle = \\ \sum_{m\gamma N_c}\left\langle 0,\alpha,L_c\right|\hat{\mathrm{H}}\left|m,\gamma,N_c\right\rangle\langle m,\gamma,N_c|n,\beta,M_v\rangle = \\ \sum_{m\gamma N_c}\left[\hat{\mathrm{H}}_{cc}\right]_{m,\beta\gamma}^{L_cN_c}\left[\hat{\mathrm{S}}_{cv}\right]_{n-m,\gamma\beta}^{N_cM_v} = \hat{\mathrm{H}}_{cc}\hat{\mathrm{S}}_{cv}\end{aligned}$$

resulting in the Hamiltonian

$$\hat{\mathrm{H}} = \begin{bmatrix}\hat{\mathrm{H}}_{cc} & \hat{\mathrm{H}}_{cc}\hat{\mathrm{S}}_{cv}\\ \hat{\mathrm{S}}_{vc}\hat{\mathrm{H}}_{cc} & \hat{\mathrm{H}}_{vv}\end{bmatrix} \tag{3.17}$$

where

$$\left[\hat{\mathrm{H}}_{vv}\right]_{n,\alpha\beta}^{L_vM_v} = \left\langle 0,\alpha,L_v\right|\hat{\mathrm{H}}\left|n,\beta,M_v\right\rangle$$

Because the $\hat{\mathrm{S}}_{cc}$ block of the overlap matrix is the unit matrix, Cholesky decomposition of $\hat{\mathrm{S}}$ can be performed

$$\hat{\mathrm{S}} = \hat{\mathrm{S}}^l\hat{\mathrm{S}}^r = \begin{bmatrix}1 & 0\\ \hat{\mathrm{S}}_{vc}^r & \hat{\mathrm{S}}_{vv}^l\end{bmatrix}\begin{bmatrix}1 & \hat{\mathrm{S}}_{cv}^r\\ 0 & \hat{\mathrm{S}}_{vv}^r\end{bmatrix} \tag{3.18}$$

with its inverse given by

$$\hat{\mathrm{S}}^{-1} = \left(\hat{\mathrm{S}}^{r}\right)^{-1}\left(\hat{\mathrm{S}}^{l}\right)^{-1} = \begin{bmatrix} 1 & -\hat{\mathrm{S}}_{cv}\left(\hat{\mathrm{S}}^{r}_{vv}\right)^{-1} \\ 0 & \left(\hat{\mathrm{S}}^{r}_{vv}\right)^{-1} \end{bmatrix} \begin{bmatrix} 1 & 0 \\ -\left(\hat{\mathrm{S}}^{l}_{vv}\right)^{-1}\hat{\mathrm{S}}_{vc} & \left(\hat{\mathrm{S}}^{l}_{vv}\right)^{-1} \end{bmatrix} \tag{3.19}$$

By employing decomposition (3.18), the Kohn-Sham equations (3.13) become

$$(\hat{\mathrm{S}}^{l})^{-1}\hat{\mathrm{H}}(\hat{\mathrm{S}}^{r})^{-1}\hat{\mathrm{D}} = \hat{\mathrm{D}}\hat{\mathrm{E}}$$

where $\hat{\mathrm{D}} = \hat{\mathrm{S}}^{r}\hat{\mathrm{C}}$, or in other words $\hat{\mathrm{D}}$ is the matrix diagonalizing the matrix $\hat{\mathrm{H}}_{p} = (\hat{\mathrm{S}}^{l})^{-1}\hat{\mathrm{H}}(\hat{\mathrm{S}}^{r})^{-1}$. Since the $c-c$ block of the matrix $\hat{\mathrm{H}}_{p}$ is already diagonal it follows that $\hat{\mathrm{D}}_{cc} = 1$. In addition to that, following from (3.17) and (3.19) the $c-v$ block of $\hat{\mathrm{H}}_{p}$ is equal to zero, meaning that the Cholesky decomposition of eq. (3.13) is actually reduced to

$$\left(\hat{\mathrm{S}}^{l}_{vv}\right)^{-1}\left(\hat{\mathrm{H}} - \hat{\mathrm{S}}_{vc}\hat{\mathrm{H}}_{cc}\hat{\mathrm{S}}_{cv}\right)\left(\hat{\mathrm{S}}^{r}_{vv}\right)^{-1}\hat{\mathrm{D}}_{vv} = \hat{\mathrm{D}}_{vv}\hat{\mathrm{E}}_{v}$$

Thus the dimensionality of the eigenproblem (3.13) is reduced only to the dimensionality of the valence subspace. The wavefunction coefficient matrix $\hat{\mathrm{C}}$ can then be obtained from $\hat{\mathrm{D}}$ as $\hat{\mathrm{C}} = (\hat{\mathrm{S}}^{r})^{-1}\hat{\mathrm{D}}$.

3.2.1 Projective Wannier Functions

When dealing with periodic systems, density-functional theory methods employ Bloch wavefunctions to represent the extended states. However, for localized properties, such as bonding information or synthesis of tight-binding models, localized states are preferred. Such states come in form of Wannier functions and since the Full Potential Local Orbital method is utilizing localized atomic-like basis to represent Bloch states, it is particularly well-suited for Wannier function computations.

Given a Bloch state $|\boldsymbol{k}, i\rangle$, a Wannier function centered in the unit cell located at position $\boldsymbol{R}$, can be defined as

$$|W; \boldsymbol{R}, \mu\rangle = \int \mathrm{d}\boldsymbol{k} \sum_{i} e^{-i\boldsymbol{k}\cdot\boldsymbol{R}_{i}} U^{\boldsymbol{k}}_{i\mu} |\boldsymbol{k}, i\rangle$$

where $U^{\boldsymbol{k}}_{i\mu}$ are elements of a unitary matrix $\hat{\mathrm{U}}^{\boldsymbol{k}}$. Because of unitarity, different choices of

$\hat{\mathrm{U}}^{\boldsymbol{k}}$ will yield physically equivalent Wannier functions. The freedom of choice of $\hat{\mathrm{U}}^{\boldsymbol{k}}$ can be used to specify Wannier functions according to a given property, such as maximal localization or a specific projective character. Bloch states $|\boldsymbol{k}, i\rangle$ are given by (3.11) and the matrix $\hat{\mathrm{U}}^{\boldsymbol{k}}$ is given by

$$\hat{\mathrm{U}}^{\boldsymbol{k}}_{i\mu} = \langle \mu | \boldsymbol{k}, i \rangle w_\mu(\varepsilon_{\boldsymbol{k}i}) \tag{3.20}$$

where $|\mu\rangle$ is a projector state which is a linear combination of localized basis states (3.9), and $w_\mu(\varepsilon)$ is an energy window, defined to be

$$w_\mu(\varepsilon) = \begin{cases} 1, & \varepsilon^{\min}_\mu < \varepsilon < \varepsilon^{\max}_\mu \\ g(\Delta\varepsilon_\mu, \varepsilon - \varepsilon^{\min}_\mu), & \varepsilon < \varepsilon^{\min}_\mu \\ g(\Delta\varepsilon_\mu, \varepsilon^{\max}_\mu - \varepsilon), & \varepsilon^{\max}_\mu < \varepsilon \end{cases}$$

where $g(\Delta\varepsilon, \varepsilon - \varepsilon_0)$ is a Gaussian of width $\Delta\varepsilon$ centered around ε_0. This means that Wannier function is specifed by its projective character μ and the energy window w_μ. This practically means, that Wannier functions, whose Bloch sum, reproduces the Kohn-Sham eigenstate with eigenvalues within the specified energy window, of a given atomic character can be extracted from the ab-initio calculation. This procedure is well defined only when matrix $\hat{\mathrm{U}}^{\boldsymbol{k}}$ as defined in (3.20) is unitary, which means that entire projective character μ must be located within the specified energy window.

Hamiltonian representation in the Wannier basis can now be obtained. Let the Bloch sum of Wannier functions be

$$|W; \boldsymbol{k}, \mu\rangle = \sum_i U^{\boldsymbol{k}}_{i\mu} |\boldsymbol{k}, i\rangle = \frac{1}{\sqrt{N}} \sum_{\boldsymbol{R}} e^{i\boldsymbol{k}\cdot\boldsymbol{R}} |W; \boldsymbol{R}, \mu\rangle$$

where N is the number of lattice sites. Expectation value of the Hamiltonian is

$$\left\langle W; \boldsymbol{k}, \mu \right| \hat{\mathrm{H}} \left| W; \boldsymbol{k}, \nu \right\rangle = \sum_{ij} U^{\boldsymbol{k}*}_{i\mu} U^{\boldsymbol{k}}_{j\nu} \left\langle \boldsymbol{k}, i \right| \hat{\mathrm{H}} \left| \boldsymbol{k}, j \right\rangle = \sum_i U^{\boldsymbol{k}*}_{i\mu} U^{\boldsymbol{k}}_{i\nu} \varepsilon_{\boldsymbol{k}i}$$

Fourier transforming this expression, we arrive at the Hamiltonian matrix elements

$$t_{\mu\nu}(\boldsymbol{R}) = \left\langle W; \boldsymbol{0}, \mu \right| \hat{\mathrm{H}} \left| W; \boldsymbol{R}, \nu \right\rangle = \int \mathrm{d}\boldsymbol{k} e^{-i\boldsymbol{k}\cdot\boldsymbol{R}} \sum_i U^{\boldsymbol{k}*}_{i\mu} U^{\boldsymbol{k}}_{i\nu} \varepsilon_{\boldsymbol{k}i}$$

These matrix elements represent hopping energies and they can be used to specify the tight-binding Hamiltonian, whose matrix elements are

$$\left[\hat{\mathrm{H}}_{\boldsymbol{k}}^{\mathrm{TB}}\right]_{\mu\nu} = \frac{1}{\sqrt{N}} \sum_{\boldsymbol{R}} t_{\mu\nu}(\boldsymbol{R}) e^{i\boldsymbol{k}\cdot\boldsymbol{R}}$$

3.3 Summary

We have seen how Kohn-Sham equations from general Density Functional theory can be cast into the computationally convenient matrix form by choosing a basis. Chosen basis states can have localized nature, such as atomic-like orbitals, which are well suited for computations of molecules, or they can have extended nature, such as plane-waves, and they are a natural choice for computations of periodic lattices.

Projector Augmented Wave method was outlined, demonstrating a hybrid approach, reconciling properties of electronic wavefunctions in the interstitial and the core regions. This is achieved by utilizing smooth pseudo-wavefunction, that can efficiently be expanded onto the planewave basis in the interstitial region, and then using the projector functions and all electron localized wavefunctions within the augmentation sphere to reproduce rapidly oscillating electronic states close to the atoms.

It is also possible to expand the extended states fully into localized basis, as is done in the Full Potential Local Orbital method. Through utilization of core and valence state separation, highly compact and efficient basis can be obtained. The method is well suited when local properties are of interest, such as bonding or disorder. In addition, this method provides a simple way to calculate the projective Wannier functions and synthesize a tight-binding model based on those functions.

Chapter 4

Structure Optimization and Matrix Diagonalization Methods

Two most important problems for the computational Ab-initio Molecular Dynamics are function minimization and matrix diagonalization. These two problems are actually interchangeable, since the function minimization can be recast into the matrix diagonalization problem through the variational principle. Kohn-Sham equations are demonstration of this, where the problem of electron density minimization was replaced by the eigenproblem (2.8).

Function minimization is important for the structure optimization, as was argued in 1.3, where minimization of the total energy $\tilde{E}$ was required, while matrix diagonalization is the computationally most demanding part of the Density Functional Theory, where the Kohn-Sham equations (2.8) are to be solved.

In this chapter, a brief overview of algorithms important for this thesis will be given. Since dealing with large matrices is necessary for purposes of the ab-initio calculations, we will focus only on the iterative methods for diagonalization of large matrices, and in particular to cases where only a part of the eigenspectrum is needed. Treatment of the full diagonalization algorithms exceeds the scope of the work here, and will be ommited.

4.1 Minimization of a Single-variable Function

The task of function minimization algorithms is to find the values in a certain subset of domain of the function, for which the function acquires minimal value. Usually, function evaluations are computationally expensive and the minimization algorithms are required to find the minimum with as few function evaluations as possible.

The task of minimization is significantly easier when the approximate location of the minimum is known, and especially if the range, called bracketing range, around the minimum in which the function is unimodular is known. This guarantees that within a bracketing range there will be only one function extremum.

Figure 4.1 shows a bracketed minimum of a single variable unimodular function f. The bracketing range has the property that signs of the first derivative at its ends are opposite, ie. $f'(a)f'(b) < 0$. Given any value x_0 from the bracket on fig. 4.1, the most straightforward attempt at finding the minimum would be to linearly extrapolate the first derivative towards zero. That is, starting from the condition $f'(x_0 + \Delta x_0) = 0$, we would have

$$\Delta x_0 = -\frac{f'(x_0)}{f''(x_0)} \tag{4.1}$$

which is known as the Newton's secant method. The procedure for a minimum search would consist of starting from the initial guess x_0, and then moving to $x_1 = x_0 + \Delta x_0$, where Δx_0 is given by eq. (4.1). Given x_i, this procedure is repeated to obtain $x_{i+1} = x_i + \Delta x_i$ as long as $|f'(x_i)|$ is greater than some threshold value. This is a very simple, and in the ideal case the quickest procedure to find the minimum. However, the biggest drawback is that it requires evaluation of the second derivative, and it might produce numerically unstable behavior in the vicinity of the inflection point where the second derivative vanishes. Simple workaround would be to use a constant value instead of the second derivative $f''(x) = 1/s$, so that $\Delta x_i = -sf'(x_i)$, resulting in the steepest descent method. Here s is the step size. The problem with this method is that the optimal step size is difficult to estimate, resulting in a minimization procedure which requires a large number of function evaluations.

These problems can be circumvented by performing the search in the bracketing range. The search proceeds by iteratively narrowing down the bracketing range. For example, figure 4.1 shows subdivision of the bracketing range $[a, b]$ into two subranges $[a, c]$ and $(c, b]$. If signs of the first derivative are opposite at the endpoints of a range, then the function minimum is bracketed by it. In this way the bracketing range can be subdivided until the resulting range is narrow enough to locate the minimum accurately enough.

The easiest way to perform the search is to perform bisection, that is to choose $c = (a + b)/2$. However, this is rather inefficient since the information about the slope of the function contained in the first derivative is not utilized. This can be achieved by combining the bisection search with the Newton's secant method (4.1). Let us assume that we are in the k-th step of the search, and that the bracketing range is $[a_k, b_k]$. Let us further take that $|f'(b_k)| \leq |f'(a_k)|$, so that b_k is a better guess for the function

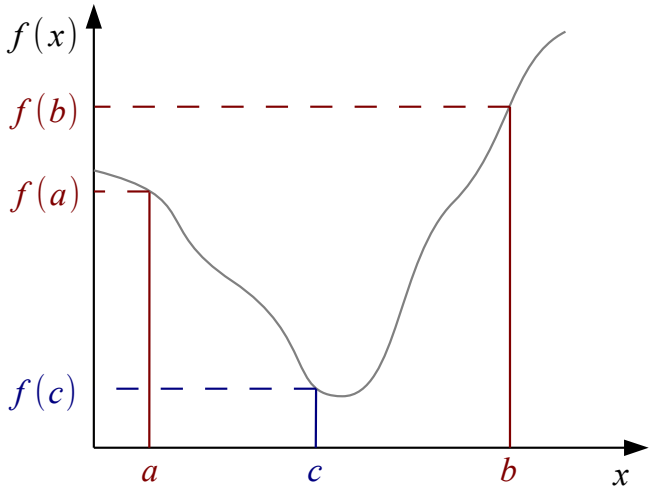

FIGURE 4.1: Bracketing of the minimum. Red lines show the current bracket, while the blue line shows the subdivision of the bracket for further search.

minimum. Then, subdivision point c_k can be computed as

$$c_k = \begin{cases} b_k - \frac{b_k - b_{k-1}}{f'(b_k) - f'(b_{k-1})} f'(b_k), & f'(b_k) \neq f'(b_{k-1}) \\ \frac{a_k + b_k}{2}, & f'(b_k) = f'(b_{k-1}) \end{cases} \tag{4.2}$$

In other words, when possible, utilize interpolation, as in the Newton's secant method, but with numerically approximate second derivative, and otherwise, use bisection search. Equation (4.2) represents the so-called Dekker's method[13]. This method usually performs well for well-behaved functions, but it can converge slower than the bisection method when bisection is used at every step, but b_k converges slowly.

To rectify this, Brent has proposed[14] few alterations. If at step $k-1$ bisection was performed then the following must be satisfied $|b_k - b_{k-1}| > \delta$ and $|b_k - b_{k-1}|/2 > |c_k - b_k|$, where δ is a given numerical tolerance. Otherwise, if at step $k-1$, interpolation was used it must hold that $|b_{k-1} - b_{k-2}| > \delta$ and $|b_{k-1} - b_{k-2}|/2 > |c_k - b_k|$ which forces the interpolation step to halve after every two iterations. Additionally, performance can be improved by using inverse quadratic interpolation instead of the linear interpolation in (4.2). Within inverse quadratic interpolation, location of the minimum is approximated by the bottom of a parabola fitted through three successive previous estimates of the minimum

$$c_k = \frac{f'(b_{k-1})f'(b_k)}{[f'(b_{k-2}) - f'(b_{k-1})][f'(b_{k-2}) - f'(b_k)]}b_{k-2} + \frac{f'(b_{k-2})f'(b_k)}{[f'(b_{k-1}) - f'(b_{k-2})][f'(b_{k-1}) - f'(b_k)]}b_{k-1} + \frac{f'(b_{k-2})f'(b_{k-1})}{[f'(b_k) - f'(b_{k-2})][f'(b_k) - f'(b_{k-1})]}b_k$$

4.1.1 Minimization of a Multi-variable Function

Minimization of the multi-variable function requires search in multidimensional space to be performed. Simple one-dimensional searches, such as bisection or Brent's method described in the previous chapter are no longer a practical solution. However, Newton's secant method (4.1) can be generalized to the case of a function of multiple variables. Let us assume that we have bracketed the minimum of the function f and let $\boldsymbol{x}_k$ belong to the bracket and be current estimate of the minimum. Then, the multi-variable version of (4.1) is

$$\Delta x_k = -\hat{\mathrm{H}}^{-1}(\boldsymbol{x}_0)\nabla f(\boldsymbol{x}_k) \tag{4.3}$$

where $\hat{\mathrm{H}}$ is the Hessian matrix. Minimization of a multi-variable function by using (4.3) suffers the same disadvantages as (4.1), compounded by the fact that evaluation of the Hessian is computationally much more expensive because it requires evaluation of N^2 second derivatives, where N is dimensionality of the parameter space. As was the case for a single-variable function, it is possible to replace the Hessian matrix by a constant, resulting in the multi-variable steepest-descent method, with the same drawbacks as in the single-variable case. Figure 4.2 a) shows a path of the steepest descent starting from $\boldsymbol{x}_0$.

It is also possible to attempt to build up the approximation of the Hessian as the minimization is conducted. This is the strategy employed by the family of the quasi-Newton methods. Usually, minimization is started with an initial Hessian given by the unit matrix $\hat{\mathrm{H}}(\boldsymbol{x}_0) = \hat{\mathrm{I}}$. As minimization proceeds, $\hat{\mathrm{H}}$ is updated and progressively a better approximation of the Hessian is constructed. For quasi-Newton methods, the step is given by

$$\Delta x_k = -\alpha_k \hat{\mathrm{H}}_k^{-1}\nabla f(\boldsymbol{x}_k) = -\alpha_k \boldsymbol{v}_k$$

where $\hat{\mathrm{H}}_k$ is the estimate of the Hessian in the k-th step of the minimization, and α_k is

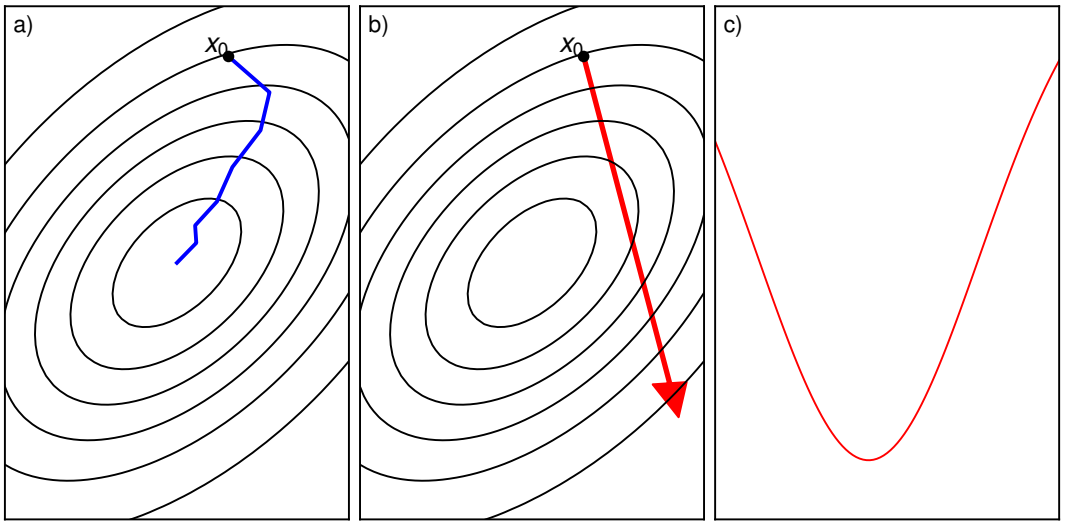

FIGURE 4.2: Minimization of the multi-variable function. Panel a) shows contour plot of the function of two variables and the path of the steepest descent starting from the initial point $\boldsymbol{x}_0$. Panel b) shows direction of the line search starting from $\boldsymbol{x}_0$ and panel c) shows function values along the line search direction.

a number chosen to satisfy Wolfe conditions[15][16].

$$f(\boldsymbol{x}_k + \alpha_k \boldsymbol{v}_k) \leq f(\boldsymbol{x}_k) + a_1 \alpha_k \nabla f(\boldsymbol{x}_k) \cdot \boldsymbol{v}_k$$
$$\nabla f(\boldsymbol{x}_k + \alpha_k \boldsymbol{v}_k) \cdot \boldsymbol{v}_k \leq a_2 \nabla f(\boldsymbol{x}_k) \cdot \boldsymbol{v}_k$$

where $0 < a_1 < 1$ and $a_1 < a_2 < 1$. The first Wolfe condition ensures that the every step Δx_k results in a sufficient decrease of f. Since that will be satisfied by a small enough α_k, the second condition serves to rule out the small steps.

The remaining issue of updating the Hessian estimate, does not have a unique solution in more that one dimension. An often used update formula is the Broyden–Fletcher–Goldfarb–Shanno [17][18][19][20] formula

$$\hat{\mathrm{H}}_{k+1} = \hat{\mathrm{H}}_k + \frac{|y_k\rangle\langle y_k|}{\langle y_k|\Delta x_k\rangle} - \frac{\hat{\mathrm{H}}_k|\Delta x_k\rangle\langle\Delta x_k|\hat{\mathrm{H}}_k^\top}{\langle\Delta x_k|\hat{\mathrm{H}}_k|\Delta x_k\rangle}$$
$$\hat{\mathrm{H}}_{k+1}^{-1} = \left(\hat{\mathrm{I}} - \frac{|\Delta x_k\rangle\langle y_k|}{\langle y_k|\Delta x_k\rangle}\right)\hat{\mathrm{H}}_k^{-1}\left(\hat{\mathrm{I}} - \frac{|y_k\rangle\langle\Delta x_k|}{\langle y_k|\Delta x_k\rangle}\right) + \frac{|x_k\rangle\langle\Delta x_k|}{\langle y_k|\Delta x_k\rangle}$$

where the Dirac notation has been used to distinguish row-vectors and column-vectors and $\boldsymbol{y}_k = \nabla f(\boldsymbol{x}_{k+1}) - \nabla f(\boldsymbol{x}_k)$.

Another minimization strategy is to choose a direction $\boldsymbol{v}_0$ in the parameter space and then search for a minimum along the given direction. This is called a line search. An example is shown in figure 4.2 b) and c). In other words, consider the single-variable function $f_1(t) = f(\boldsymbol{x}_0 + t\boldsymbol{v}_0)$, and then utilize, for example, Brent's method to locate its minimum, $\boldsymbol{x}_1$. Then, starting from $\boldsymbol{x}_1$, one performs the minimum search along some other direction $\boldsymbol{v}_1$ to obtain $\boldsymbol{x}_2$ and so on until $|\nabla f(\boldsymbol{x}_i)|$ becomes smaller than a numerical threshold ε. With an appropriate choice of directions $\boldsymbol{v}_i$, the minimization can be made more efficient and accurate than the steepest descent.

The conjugate gradient method[21] achieves an efficient minimization by performing line searches along the *conjugate* directions. Directions $\boldsymbol{v}_i$ and $\boldsymbol{v}_j$ are conjugate with respect to a symmetric positive definite matrix $\hat{\mathrm{A}}$ if $\boldsymbol{v}_i \cdot \hat{\mathrm{A}}\boldsymbol{v}_j = \delta_{ij}$. That is, the scalar products are taken with respect to the metric given by $\hat{\mathrm{A}}$, instead of the usual Cartesian metric $\hat{\mathrm{A}} = \hat{\mathrm{I}}$. The matrix $\hat{\mathrm{A}}$ is taken to be the Hessian of the quadratic function

$$f_q(\boldsymbol{x}) = \boldsymbol{x} \cdot \hat{\mathrm{A}}\boldsymbol{x} + \boldsymbol{b} \cdot \boldsymbol{x}$$

which approximates the function f in the bracketing region, with f and f_q having identical minima. Due to the positive definiteness of $\hat{\mathrm{A}}$, the function f_q has a minimum $\boldsymbol{x}_q$ satisfying the condition $\nabla f_q(\boldsymbol{x}_q) = \hat{\mathrm{A}}\boldsymbol{x}_q + \boldsymbol{b} = 0$. The strength of the conjugate gradient method lies in the fact that at most N line searches are needed to find a minimum of f_q when searching along the directions conjugate with respect to $\hat{\mathrm{A}}$.

The conjugate gradient algorithm proceeds in the following manner: let $\boldsymbol{x}_0$ be an initial guess for the minimum, and let the initial search direction be $\boldsymbol{v}_0 = \nabla f_q(\boldsymbol{x}_0)$; let us assume the algorithm is in the k-th iteration so that $\boldsymbol{x}_k$ and $\boldsymbol{v}_k$ are estimate for the minimum and direction of the search, respectively; then

1. Perform line search along the line $\boldsymbol{l}(t) = \boldsymbol{x}_k + t\boldsymbol{v}_k$ to find the location of the minimum $\boldsymbol{x}_{k+1} = \boldsymbol{l}(t_{\min})$, where $t_{\min}$ is given by

$$t_{\min} = -\frac{\boldsymbol{v}_k \cdot \nabla f_q(\boldsymbol{x}_k)}{\boldsymbol{v}_k \cdot \hat{\mathrm{A}}\boldsymbol{v}_k} \tag{4.4}$$

   which follows from the condition that $\nabla f_q(\boldsymbol{l}(t_{\min})) = 0$.

2. If $k < N-1$, compute the new search direction $\boldsymbol{v}_{k+1} = -\nabla f_q(\boldsymbol{x}_{k+1}) + \beta_k \boldsymbol{v}_k$, where

$$\beta_k = \frac{\nabla f_q(\boldsymbol{x}_{k+1}) \cdot \hat{\mathrm{A}}\boldsymbol{v}_k}{\boldsymbol{v}_k \cdot \hat{\mathrm{A}}\boldsymbol{v}_k} \tag{4.5}$$

which is a choice that guarantees that the direction $\boldsymbol{v}_{k+1}$ is conjugate to all previous directions $\boldsymbol{v}_i, i < k+1$.

3. If $k = N-1$ we can terminate the minimization since $\boldsymbol{x}_N$ estimated in the step one is minimum.

Here we have to take into account that this refers to the quadratic function f_q which is just an approximation to f. Applying conjugate gradient minimization to f means that the upper limit of N line searches cannot be guaranteed. Also, evaluation of the Hessian is needed in (4.4) and (4.5), which is something we would like to avoid. The use of $\hat{\mathrm{A}}$ in eq. (4.4) can be avoided by employing some one-dimensional minimum search algorithm, such as Brent's algorithm, while the use in eq. (4.5) can be avoided thanks to the fact that

$$\nabla f_q(\boldsymbol{x}_{k+1}) - \nabla f_q(\boldsymbol{x}_k) = \hat{\mathrm{A}}(\boldsymbol{x}_{k+1} - \boldsymbol{x}_k) = c\hat{\mathrm{A}}\boldsymbol{v}_k$$

where c is a constant. This follows from step two of the algorithm where $\boldsymbol{x}_{k+1} = \boldsymbol{x}_k + t_{\min}\boldsymbol{v}_k$. Thus (4.5) can be written as

$$\beta_k = \frac{\nabla f_q(\boldsymbol{x}_{k+1}) \cdot [\nabla f_q(\boldsymbol{x}_{k+1}) - \nabla f_q(\boldsymbol{x}_k)]}{\boldsymbol{v}_k \cdot [\nabla f_q(\boldsymbol{x}_{k+1}) - \nabla f_q(\boldsymbol{x}_k)]} \tag{4.6}$$

so that $\hat{\mathrm{A}}$ is eliminated altogether. This is known as the Hestenes-Stiefel formula. Further utilization of the conjugate property of directions $\boldsymbol{v}_i$ and quadratic form of f_q result in further simplifications

$$\begin{aligned} \beta_k &= \frac{\nabla f_q(\boldsymbol{x}_{k+1}) \cdot [\nabla f_q(\boldsymbol{x}_{k+1}) - \nabla f_q(\boldsymbol{x}_k)]}{|\nabla f_q(\boldsymbol{x}_k)|^2} \\ \beta_k &= \frac{|\nabla f_q(\boldsymbol{x}_{k+1})|^2}{|\nabla f_q(\boldsymbol{x}_k)|^2} \end{aligned} \tag{4.7}$$

which are known as Polak-Ribiere and Fletcher-Reeves formulas, respectively. Formulas (4.6) and (4.7) are equivalent and exact when applied to f_q, but become only approximate and no longer equivalent for general non-quadratic function f. Which formula performs best depends on the properties of the function f.

4.1.2 Fast Inertial Relaxation Engine

The algorithms described so far are local minimization algorithms and they can be guaranteed to succeed only when the minimum is bracketed. In other words, it is necessary to have a good initial guess for the minimum. When starting without a good initial guess, a variety of global minimization algorithms exist. Of interest for this work is the Fast Inertial Relaxation Engine (FIRE) algorithm[22], representing a hybrid of local and global optimization techniques.

The FIRE algorithm relies on the analogy between the energy minimization and downhill movement on the potential energy landscape. According to the analogy, a path $\boldsymbol{x}(t)$ leading to the minimum of a function $f(\boldsymbol{x})$ is given by the modified Newton's second law

$$\frac{\mathrm{d}\boldsymbol{v}(t)}{\mathrm{d}t} = \frac{\boldsymbol{F}(t)}{m} - \gamma(t)|\boldsymbol{v}(t)|\left[\hat{\boldsymbol{v}}(t) - \hat{\boldsymbol{F}}(t)\right] \tag{4.8}$$

where t parametrizes the path (analogous to time), $\boldsymbol{v}(t) = \mathrm{d}\boldsymbol{x}(t)/\mathrm{d}t$ is the velocity along the path, $\boldsymbol{F}(t) = \nabla f(\boldsymbol{x}(t))$ are derivatives of the function to be minimized (analogous to force), $\hat{\boldsymbol{v}}(t)$ and $\hat{\boldsymbol{F}}(t)$ are unit vectors in directions of $\boldsymbol{v}(t)$ and $\boldsymbol{F}(t)$ respectively, and $\gamma(t)$ is a time-dependent scaling function. The first term on the right-hand side of (4.8) is identical to the second Newton's law, while the second term is such that it pulls the minimization path towards the steepest descent path faster than it would be the case with just the first term. The fact that eq. (4.8) contains the second derivative of $\boldsymbol{x}(t)$ means that inertia is used as a means to automatically increase the step size since $\boldsymbol{v}(t)$ is increased at every step with downhill motion.

The downside to this is that, due to inertia, the minimization path can turn in the uphill direction. That is why, it is necessary to ascertain that power the $P(t) = \boldsymbol{v}(t) \cdot \boldsymbol{F}(t)$ is positive, guaranteeing the downhill motion. In case $P(t) < 0$, velocity is set to zero, and the minimization is restarted.

In addition to this, after every step of the minimization, the time step Δt can be increased resulting in larger $\Delta\boldsymbol{x}(t)$. Also, the scaling function $\gamma(t)$ can successively be decreased, since it is important only when the movement is not in the direction of steepest descent. This allows the minimization path to stay as close as possible to the steepest descent path while keeping the minimization steps as large as possible.

4.1.3 Application of Fast Inertial Relaxation Engine to the Full Structural Relaxations Under the Arbitrary Stress Tensor

When we apply (4.8) to the problem of energy minimization of the crystal lattice, we can understand eq. (4.8) as a description of the metadynamical time evolution of the atomic nuclei. This permits energy minimization under application of external forces[23].

Let us consider a crystal lattice with the unit cell vectors $\boldsymbol{a}$, $\boldsymbol{b}$ and $\boldsymbol{c}$, containing N atomic nuclei at positions $\boldsymbol{r}_i$, $i = 1, ..., N$. Positions $\boldsymbol{r}_i$ are related to the fractional positions $\boldsymbol{s}_i$ through

$$\boldsymbol{r}_i = \hat{\mathrm{h}}\boldsymbol{s}_i = \begin{bmatrix} a_x & b_x & c_x \\ a_y & b_y & c_y \\ a_z & b_z & c_z \end{bmatrix} \boldsymbol{s}_i \tag{4.9}$$

where $\hat{\mathrm{h}}$ is the unit cell matrix, whose columns are composed of the unit cell vector components. To perform the full structural relaxation, we consider the internuclear interaction energy to be a function of the extended set of $3N + 9$ coordinates, consisting of $\tilde{\boldsymbol{x}} = (\boldsymbol{s}_i, \hat{\mathrm{h}})$, so that $E = E(\tilde{\boldsymbol{x}})$. Energy minimization according to (4.8) requires evaluation of fictitious forces, $\tilde{\boldsymbol{F}}_k = (\partial E/\partial \boldsymbol{s}_i, \partial E/\partial \hat{\mathrm{h}})$ and we need to express them in terms of the physical forces acting on the lattice, which are given by

$$\boldsymbol{F}_i = \frac{\partial E(\boldsymbol{s}_i, \hat{\mathrm{h}})}{\partial \boldsymbol{r}_i}$$
$$\hat{\sigma} = -\frac{1}{V}\frac{\partial E(\boldsymbol{s}_i, \hat{\mathrm{h}})}{\partial \hat{\varepsilon}}$$

where $\boldsymbol{F}_i$ are forces acting on atomic nuclei, and $\hat{\sigma}$ is matrix of the lattice stress tensor, and $\hat{\varepsilon}$ is matrix of the infinitesimal lattice strain tensor. The strain tensor $\hat{\varepsilon}$ describes an infinitesimal deformation of the crystal lattice

$$\boldsymbol{r}_i \to \boldsymbol{r}_i'(\hat{\varepsilon}) = (1 + \hat{\varepsilon})\boldsymbol{r}_i \tag{4.10}$$

If we take that in the deformed lattice, the unit cell deforms as $\hat{\mathrm{h}} \to \hat{\mathrm{h}}'(\hat{\varepsilon})$, it is easy to see from (4.9) and (4.10) that

$$\hat{\mathrm{h}}'(\hat{\varepsilon}) = (1 + \hat{\varepsilon})\hat{\mathrm{h}} \tag{4.11}$$

The fictitious force components are now

$$\frac{\partial E(\boldsymbol{s}_i, \hat{\mathrm{h}})}{\partial \boldsymbol{s}_i} = \frac{\partial E(\boldsymbol{s}_i, \hat{\mathrm{h}})}{\partial \boldsymbol{r}_i} \frac{\partial \boldsymbol{r}_i}{\partial \boldsymbol{s}_i} = \boldsymbol{F}_i \frac{\partial \boldsymbol{r}_i}{\partial \boldsymbol{s}_i} \tag{4.12}$$

$$\frac{\partial E(\boldsymbol{s}_i, \hat{\mathrm{h}})}{\partial \hat{\mathrm{h}}} = \frac{\partial E(\boldsymbol{s}_i, \hat{\mathrm{h}})}{\partial \hat{\varepsilon}} \frac{\partial \hat{\varepsilon}}{\partial \hat{\mathrm{h}}} = -V\hat{\sigma} \frac{\partial \hat{\varepsilon}}{\partial \hat{\mathrm{h}}} \tag{4.13}$$

From (4.9) and (4.11) we have that

$$\frac{\partial \boldsymbol{r}_i}{\partial \boldsymbol{s}_i} = \hat{\mathrm{h}}$$
$$\frac{\partial \hat{\mathrm{h}}}{\partial \hat{\varepsilon}} = \lim_{\hat{\varepsilon} \to 0} \frac{\partial \hat{\mathrm{h}}'(\hat{\varepsilon})}{\partial \hat{\varepsilon}} = \hat{\mathrm{h}}^\top$$

Combining this with (4.12) results in

$$\frac{\partial E(\boldsymbol{s}_i, \hat{\mathrm{h}})}{\partial \boldsymbol{s}_i} = \boldsymbol{F}_i \hat{\mathrm{h}}$$
$$\frac{\partial E(\boldsymbol{s}_i, \hat{\mathrm{h}})}{\partial \hat{\mathrm{h}}} = -V\hat{\sigma} \left(\hat{\mathrm{h}}^\top\right)^{-1}$$

External forces can be applied by taking $\boldsymbol{F}_i \to \boldsymbol{F}_i - \boldsymbol{F}_i^{\mathrm{ext}}$ and $\hat{\sigma} \to \hat{\sigma} - \hat{\sigma}^{\mathrm{ext}}$. With these expressions all quantities needed for the application of (4.8) can be computed from the forces and the stress tensor obtained in the ab-initio calculations, and full structural relaxation can be performed.

4.2 Diagonalization Algorithms

The goal of diagonalization algorithms is, given a large N by N Hermitian matrix $\hat{\mathrm{A}}$, to find a set of N orthonormal vectors $|x_i\rangle$ for which

$$\hat{\mathrm{A}}|x_n\rangle = \lambda_n |x_n\rangle \tag{4.14}$$

holds, where λ_i are eigenvalues. We have restricted ourselves only to the Hermitian

matrices, since they are important in our case, but the algorithms described don't necessarily need to be restricted to them.

As was the case with the minimization, the idea is to iteratively diagonalize the matrix, starting from an initial trial subspace $\mathbb{V}^0$, consisting of a certain number of trial vectors $|x_i^0\rangle$, and then iteratively expanding the trial subspace, building progressively better approximation of the eigenvalues and the eigenvectors.

The basic idea behind the iterative algorithms is the concept of the power iteration. Let us assume that eigenvalues λ_n are sorted by their absolute values in descending order, so that λ_0 is the highest magnitude eigenvalue. The spectral decomposition of $\hat{\mathrm{A}}$ is given by

$$\hat{\mathrm{A}} = \sum_n \lambda_n |x_n\rangle\langle x_n|$$

Owing to the fact that $|x_n\rangle$ are orthornormal, the spectral decomposition of the p-th power of $\hat{\mathrm{A}}$ is given by

$$\hat{\mathrm{A}}^p = \sum_n \lambda_n^p |x_n\rangle\langle x_n|$$

Let $|y\rangle$ be an arbitrary vector. The ction of $\hat{\mathrm{A}}^p$ on the $|y\rangle$ is

$$\hat{\mathrm{A}}^p|y\rangle = \sum_n \lambda_n^p |x_n\rangle\langle x_n|y\rangle = \lambda_0^p \sum_n \left(\frac{\lambda_n}{\lambda_0}\right)^p |x_n\rangle\langle x_n|y\rangle$$

If $|\lambda_0| > |\lambda_n|$ for $n > 0$, and p is large enough, then $(\lambda_n/\lambda_0)^p \approx 0$ and

$$\hat{\mathrm{A}}^p|y\rangle \approx \lambda_0^p |x_0\rangle\langle x_0|y\rangle = c|x_0\rangle$$

In other words, the action of the p-th power of matrix $\hat{\mathrm{A}}$ will yield the eigenvector of the dominant eigenvalue. This can only be taken to hold approximately, since the computation of large powers of $\hat{\mathrm{A}}$ is impractical, and λ_0 can have a large number of other eigenvalues in its vicinity. Despite of this, the power iteration presents a solid foundation, since instead of relying on just a single eigenvector $\hat{\mathrm{A}}^p|y\rangle$, we can expect to be able resolve a certain number of $K < p$ highest eigenvalues and eigenvectors of $\hat{\mathrm{A}}$, over a subspace

$$\mathbb{V}^p = \mathrm{span}\left(|y\rangle, \hat{\mathrm{A}}|y\rangle, \hat{\mathrm{A}}^2|y\rangle, ..., \hat{\mathrm{A}}^p|y\rangle\right) \tag{4.15}$$

where p is not too large. In realistic calculations, the subspace $\mathbb{V}^p$ is not built by a direct application of powers of $\hat{\mathrm{A}}$ as in (4.15), since in general, the sequence of vectors $\hat{\mathrm{A}}^i|y\rangle, i = 1, ..., p$, is not orthonormal, and the sequence can be made to converge quicker by application of a suitably chosen matrix function $\hat{\mathrm{f}}(\hat{\mathrm{A}})$.

If the highest magnitude eigenvalues are not of interest, it is possible to perform the so-called shift-invert transformation. If, instead of $\hat{\mathrm{A}}$, we consider the matrix $(\hat{\mathrm{A}} - \sigma\hat{\mathrm{I}})^{-1}$, the power iteration will yield eigenvalues closest to σ.

For applications in physics, we are usually interested in the ground state, or certain number of states above the ground state, which means that we need only a certain number of lowest energy eigenvalues of $\hat{\mathrm{A}}$ (highest in absolute value). Thanks to this, a lot of computational effort for large matrices can be saved. Additional simplification arises when the matrix is diagonally dominant, as is usually the case in the ab-initio calculations. Davidson [24] algorithm was devised for such cases. It proceeds in the following manner.

Search starts from the initial trial subspace $\mathbb{V}^0 = \{|x^0\rangle\}$ consisting of a single vector. Let us assume that we are in the k-th iteration, and let the trial subspace be $\mathbb{V}^k = \{|x^0\rangle, ..., |x\rangle^k\}$. All vectors are taken to be normalized. Let $\hat{\mathrm{V}}^k$ be a matrix, whose columns are vectors $|x^i\rangle, i = 0, ..., k$ so that projection of $\hat{\mathrm{A}}$ onto the $\mathbb{V}^k$ is given by $\hat{\mathrm{A}}^k = (\hat{\mathrm{V}}^k)^\dagger \hat{\mathrm{A}} \hat{\mathrm{V}}^k$. Projection $\hat{\mathrm{A}}^k$ is a relatively small matrix, and some of the full diagonalization methods, such as the QR algorithm (Francis1961) (Francis1962) (Kublanovskaya1961), ca be efficiently employed to diagonalize it. Let μ^k be the eigenvalue with the highest absolute value, and let $|w^k\rangle$ be it's eigenvector. By projecting $|w^k\rangle$ back from the $\mathbb{V}^k$ subspace we obtain the current estimates of the eigenvalue and eigenvector of $\hat{\mathrm{A}}$, $\lambda^{k+1} = \mu^k$ and $|x^{k+1}\rangle = (\hat{\mathrm{V}}^k)^\dagger |w^k\rangle$ respectively. Error of the estimated eigenpair is given by the residual vector

$$|r^k\rangle = (\hat{\mathrm{A}} - \lambda^{k+1}\hat{\mathrm{I}})|x^{k+1}\rangle \tag{4.16}$$

If the norm of the residual vector is smaller than the numerical tolerance, then λ^{k+1} is the highest magnitude eigenvalue of $\hat{\mathrm{A}}$ and $\hat{\mathrm{x}}^{k+1}$ is its eigenvector. At the same time, the eigenvalues λ^i for $M < i < k + 1$, with $M > 0$, will be a good approximation of the next $k + 1 - M$ eigenvalues of $\hat{\mathrm{A}}$ sorted by magnitude and $|x^i\rangle$ will be an approximation to their eigenvector.

If, however, $|r^k\rangle$ is above the numerical tolerance, the trial subspace needs to be expanded. The expansion is in the direction of the vector

$$|\tilde{x}^{k+1}\rangle = \hat{\mathrm{M}}^{-1}|r^k\rangle = (\hat{\mathrm{D}} - \lambda^{k+1})^{-1}|r^k\rangle$$

where $\hat{\mathrm{D}}$ is a matrix whose diagonal consists of diagonal matrix elements of $\hat{\mathrm{A}}$. Since the preconditioner $\hat{\mathrm{M}} = \hat{\mathrm{D}} - \mu_k\hat{\mathrm{I}}$ is diagonal, it is trivial to invert it. After this, $|\tilde{x}^{k+1}\rangle$ is orthonormalized with respect to the trial subspace $\mathbb{V}^k$, to obtain $|x^{k+1}\rangle$ and the new trial subspace $\mathbb{V}^{k+1} = \mathbb{V}^k \cup \{|x^{k+1}\rangle\}$ is formed.

Choice of the particularly simple preconditioner $\hat{\mathrm{M}}$ in (4.16) stems from the fact that we have assumed $\hat{\mathrm{A}}$ to be a diagonally dominant matrix. Applicability of the Davidson algorithm can be expanded for other matrix type, by changing the form of the preconditioner.

Another important diagonalization method is the Residual Minimization by Direct Inversion in the Iterative Subspace (RM-DIIS)(Pulay1980). It is particularly well suited to the problems where initial guess for the eigenvectors is already known, and in this case it converges to the correct solution very rapidly.

Let $|x_n\rangle$ be the exact set of eigenvectors of $\hat{\mathrm{A}}$ we want to find and let $|\tilde{x}_n^0\rangle$ be initial guess for those vectors. Let us further assume that RM-DIIS algorithm has performed k iterations and has generated a sequence of trial vectors $|\tilde{x}_n^i\rangle$ from the initial set $|\tilde{x}_n^0\rangle$. The strategy of RM-DIIS algorithm is to generate the next set of trial vectors as a linear combination of all previous trial vectors in a fashion which minimizes the total residual error. We will assume that all vectors are orthonormal.

We have to formulate the residual minimization error equation now. The new set of trial vectors is

$$|\tilde{x}_n^{k+1}\rangle = \sum_{i=1}^{k} c_i|\tilde{x}_n^i\rangle \tag{4.17}$$

while the residual error of a single vector is given by

$$|\Delta\tilde{x}_n^i\rangle = (\hat{\mathrm{A}} - \hat{\mu}_n^i)|\tilde{x}_n^i\rangle \tag{4.18}$$

where $\mu_n^i = \langle\tilde{x}_n^i|\hat{\mathrm{A}}|\tilde{x}_n^i\rangle$ are eigenvalue estimates. Since trial vectors are related to the exact vectors as $|\tilde{x}_n^i\rangle = |x_n\rangle + |\Delta\tilde{x}_n^i\rangle$, we can rewrite (4.17) for the case where $|\tilde{x}_n^{k+1}\rangle$ converges to the exact solution as

$$|x_n\rangle = \sum_{i=1}^{k} c_i |x_n\rangle + \sum_{i=1}^{k} c_i |\Delta\tilde{x}_n^i\rangle$$

In order to for this to be satisfied, $\sum_{i=1}^{k} c_i = 1$ and $\sum_{i=1}^{k} c_i |\Delta\tilde{x}_n^i\rangle = 0$ must hold, which means that residual error minimization is achieved by minimizing

$$L(\boldsymbol{c}, \lambda) = \sum_{i,j=1}^{k} c_i^* c_j \langle \Delta\tilde{x}_n^i | \Delta\tilde{x}_n^j \rangle + \lambda \left(\sum_{i=1}^{k} c_i - 1 \right) \tag{4.19}$$

where $\boldsymbol{c} = (c_1, ..., c_k)$ and λ is the Lagrange multiplier. The minimization of the first term on the right-hand side of (4.19) achieves minimization of the magnitude of error (4.18), while the second term guarantees that coefficients c_i sum to unity. Let us define the overlap matrix $\hat{\mathrm{S}}$ whose matrix elements are $S_{ij} = \langle \Delta\tilde{x}_n^i | \Delta\tilde{x}_n^j \rangle$. Minimization of (4.19) is achieved when derivatives of $L(\boldsymbol{c}, \lambda)$ with respect to all c_i and λ vanish, resulting in the set of linear equations

$$\begin{bmatrix} S_{11} & S_{12} & \cdots & S_{1k} & 1 \\ S_{21} & S_{22} & \cdots & S_{2k} & 1 \\ \vdots & \vdots & \ddots & \vdots & \vdots \\ S_{k1} & S_{k2} & \cdots & S_{kk} & 1 \\ 1 & 1 & \cdots & 1 & 0 \end{bmatrix} \begin{bmatrix} c_1 \\ c_2 \\ \vdots \\ c_k \\ -\lambda \end{bmatrix} = \begin{bmatrix} 0 \\ 0 \\ \vdots \\ 0 \\ 1 \end{bmatrix}$$

which determine the coefficients c_i and thus, a new set of trial vectors $|\tilde{x}_n^{k+1}\rangle$ are obtained. The vectors are orthonormalized and a new iteration can be performed if the magnitude of residual errors (4.18) was larger than the numerical tolerance.

4.3 Summary

In this chapter, a general overview of ideas necessary to computationally treat problems of structure optimization and solution of the Kohn-Sham equations was presented.

Structure optimization requires optimization of energy in the multidimensional parameter space. Three algorithms were outlined, the Conjugate Gradient and the BFGS Quasi-Newton method, as local algorithms for cases where good starting point for the relaxation is available, and a hybrid of local and global minimization approaches, the FIRE. In addition, dynamical nature of the FIRE algorithm has served as a convenient starting point to implement the full structural relaxations under arbitrary stress tensor, which plays an important part of this work.

Further, basic ideas necessary when approaching the problem of diagonalization of large matrices were presented. Two diagonalization algorithms were briefly showcased. A robust, Davidson algorithm, and the less robust, but faster RM-DIIS algorithm, for cases when the Kohn-Sham equations are to be solved when good initial wavefunctions are known.

Chapter 5

Ab-Initio Simulations of the Application of Pressure in $BaFe_2As_2$ and $CaFe_2As_2$

Although it has been known that LaOFeAs is superconducting with T_c of 3.5 K [25], the iron-pnicitides did not attract a lot of attention until 2008, when T_c of 26 K was measured in $LaO_{1-x}F_xFeAs$ [26]. In the subsequent rush of experimental activity, higher and higher critical temperatures have been obtained, either by doping, either by applying pressure, culminating in the, still somewhat controversial, discovery of T_c of 65 K in the monolayer FeSe grown on the $SrTiO_3$ substrate [27, 28], sparking the hope that it might be possible for iron pnictides to bring the T_c high enough so that liquid nitrogen could be used for cooling, which would have big implications for the practical applications.

Since one pressure is one of two principal ways to tune the superconductivity in iron pnictides we have performed the ab-initio simulations of pressure application in order to study how structural and electronic properties of iron pnictides evolve under its effect[23, 29]. These results are presented in this chapter.

The organization of the chapter is as follow. First, we will give a brief overview of general properties of iron pnictide family of materials and then we will focus on the pressure application on the $BaFe_2As_2$ and $CaFe_2As_2$ as representatives of the so-called 122 family. We will first present the results of simulations of hydrostatic pressure and then the results of simulations of uniaxial pressure along all three crystallographic axes. The application of in-plane uniaxial pressure will be discussed in the context of the Ginzburg-Landau theory of phase transition (contributed by Rafael M. Fernandes).

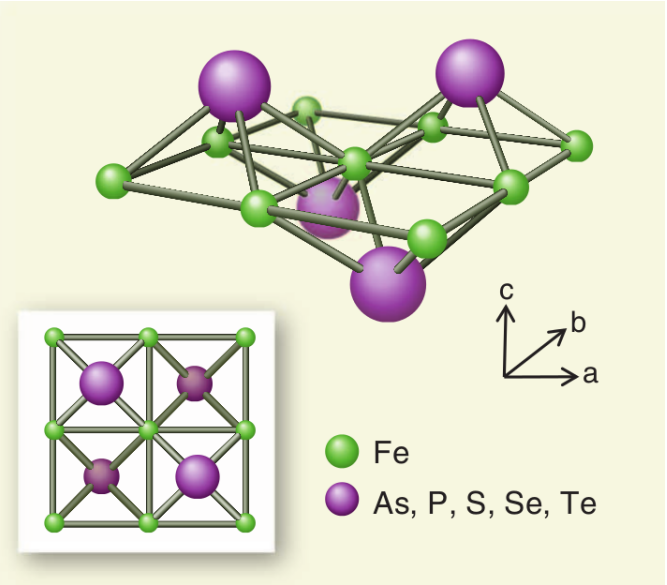

FIGURE 5.1: The schematic view of building blocks of a FeAs layer. (Figure adapted from ref. [30])

5.1 Structure of Iron Pnictides

The basic building block of all iron pnictides is a trilayer consisting of Fe and pnictogen (P, As) or chalcogen (Se, Te, S) atoms (figure 5.1). Each trilayer consists of the central layer Fe atoms, sandwiched between the two layers of pnictogen or chalcogen atoms. Every layer, making up the trilayer is a square lattice of atoms. The arrangment of atoms is such that pnictogen or chalcogen atoms tetrahedrally coordinate the iron atom. The trilayer will subsequently be referred to as the FePn layer, even for the case of iron chalcogenides.

From this building block, different families of structures can be made by stacking the FePn layers in different fashions, and intercalating different atoms between the layers. The principal familes are the so called 11, 111, 1111, 122, 32522 and 21311. The 11 family consists of the FeSe and FeTe compounds. Structurally, they are simply a lattice of vertically stacked FePn layers, with two iron and two chalcogen atoms per unit cell, which is tetragonal. The convention for unit cell notation is such, that **a** and **b** denote the unit cell vectors lying parallel to the FePn plane, while the **c** is perpendicular to it (see fig. 5.1). This convention extends to other families of iron pnictides.

The structures of 11, 111, 1111, 122, 32522 and 21311 families are shown in figure 5.2 along with their superconducting critical temperatures, from left to right respectively. The 1111 family is composed of FePn layers separated by the trilayer of oxygen and

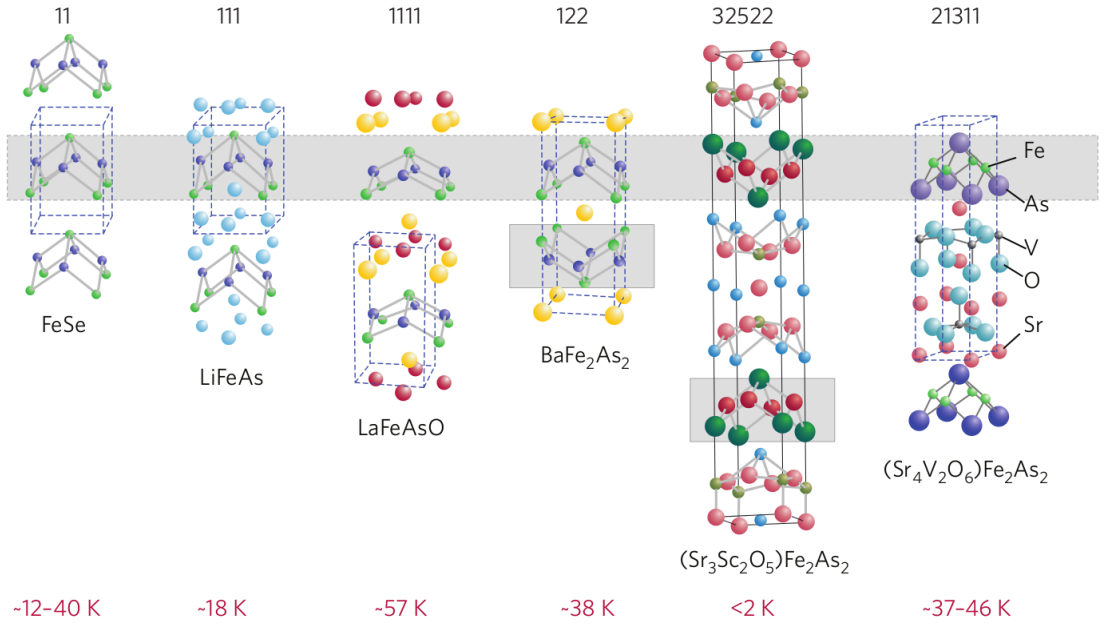

FIGURE 5.2: Structural families of iron pnictides and their respective superconducting critical temperatures. (Figure taken from ref. [31])

rare earth atoms, or the OR layer. Within the OR layer, O atoms are tetrahedrally coordinated by the rare earth atoms, La for example. For the 111 family, the role of the separator of FePn layers is played by the alkaline metals, such as Li, while for the 122 family, that role is played by the alkaline earths, such as Ca or Ba. One distinctive feature of the 122 and 32522 families is that the unit cell contains two FePn layers, shifted by $(\boldsymbol{a} + \boldsymbol{b})/2$. As a result, the 122 and 32522 families are described by the nonsymmorphic space groups, while all other families are described by the symmorphic space groups. Since the 122 family is in the focus of this thesis, more attention will be given to it in the exposition that follows.

5.2 Basic Phenomenology

At ambient pressure and temperature, all iron pnictides are paramagnetic metals with the tetragonal unit cells shown in the figure 5.2. On cooling, when temperature reaches T_S, the structure develops an orthorhombic distortion which is followed by the onset of the spin density wave driven antiferromagnetic order at temperature $T_N \leq T_S$. In the orthorhombic phase, **a** is taken to be the longer axis. The antiferromagnetic order and the orthorhombic distortion are shown on figure 5.3. Magnetic moments of the Fe atoms are aligned in the **ab** plane and they are antiferromagnetically ordered along the

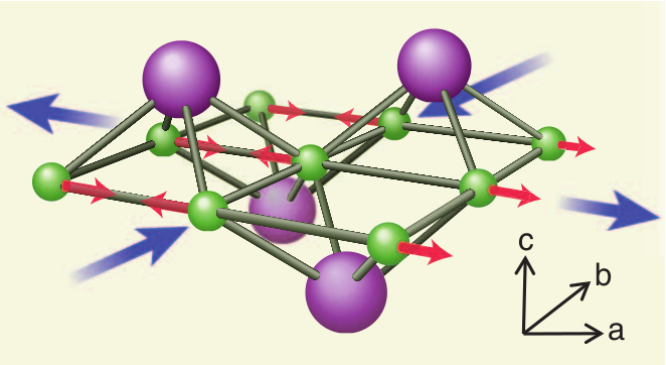

FIGURE 5.3: Schematic view of the magnetically ordered phase in iron pnictides. The red arrows show iron's magnetic moments, while the blue arrows show orthorhombic distortion. (Figure adapted from ref. [30])

a axis and feromagnetically along the **b** axis.

With the application of pressure, or doping, the transition to the AFM orthorhombic phase can be suppressed, and superconductivity can be observed within a range of pressures. The schematic of the typical phase diagram under doping and pressure is shown in the figure 5.4. It has broadly symmetric features with respect to the hole or the electron doping.

Depending on the exact compound, the phase diagram details can vary. For example, the phase diagram on the figure 5.4 shows the region (shaded in light blue) where the compound is in the orthorhombic state, but the antiferromagnetic ordering still did not set in. The size of this region depends on the material, so for example, in LaFeAsO, the onset of the structural transition occurs at 155K and the magnetic ordering sets in at 137K [32], while in $BaFe_2As_2$, the structural and the magnetic phase transitions are almost simultaneous [33]. Although the phase diagram shows the superconductivity regions excluding the magnetic order, in some materials, the coexistence has been found. For example, no coexistence has been observed in the $CeO_{1-x}F_xFeAs$ [34], while in the $Ba(Fe_{1-x}Co_xAs)_2$ [35] the magnetic order has been detected in the superconducting region.

Underlying these observations is the Fermi surface characterized by the cylindrical topology as shown on panel (a) of fig. 5.5 [36, 37]. The Fermi surface shown corresponds to $BaFe_{1.94}Co_{0.06}As_2$ and is composed of Fermi surface sheets arising from the bands dominated by the iron's $3d$ orbitals with some contributions from the $4p$ orbitals of pnictogen and chalcogen atoms. Centered around the Γ point are three hole pockets,

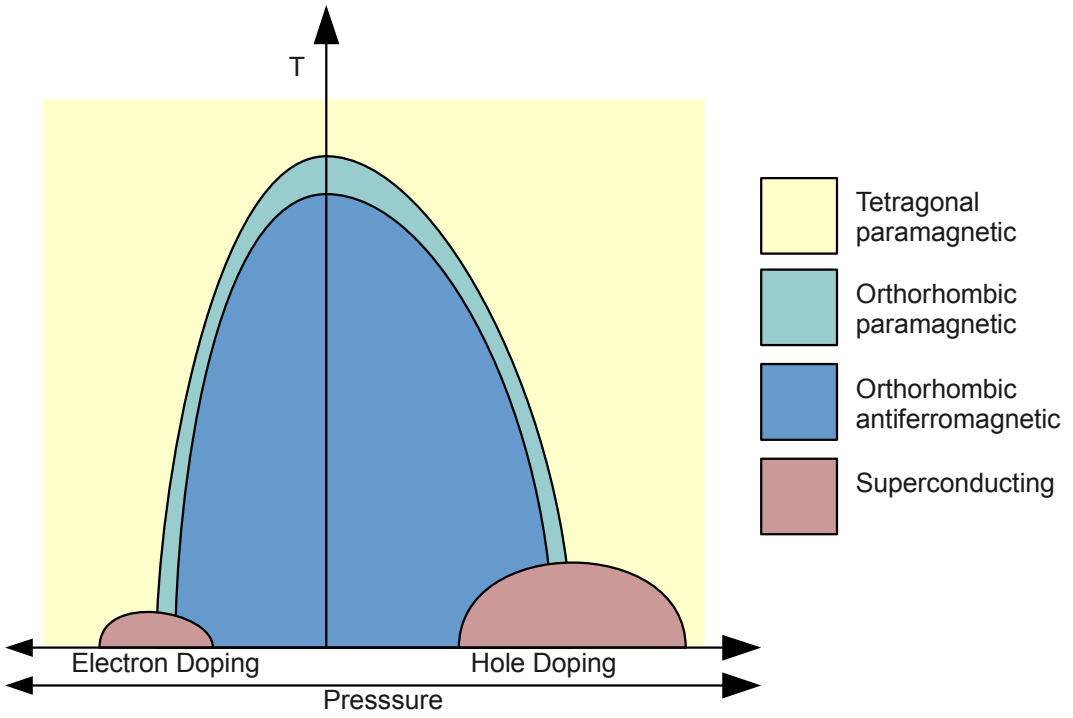

FIGURE 5.4: Schematic view of the typical phase diagram of iron pnictide compounds.

while two electron pockets are centered around the M point in the two iron equivalent Brillouin zone. It is believed that the nesting between the hole and the electron pockets plays an important role in the formation of magnetic order as well as for the superconductivity[36]. However, there are exceptions to this simple picture, notably $K_{0.8}Fe_2Se_2$, which was found to be superconducting in 2010[38], but is lacking the hole cylinder (panel (b) on fig. 5.5).

5.3 Overview of Pressure Application on $BaFe_2As_2$ and $CaFe_2As_2$

One of the families that has been intensively studied under pressure is the 122 family $AEFe_2As_2$ (AE = Ca, Sr, and Ba). $CaFe_2As_2$ at ambient pressure undergoes a first order phase transition from a tetragonal to an orthorhombic phase at 172 K accompanied by a magnetic transition. Initial reports on pressure experiments showed that at $P \sim 0.23$ GPa the orthorhombic and antiferromagnetic phases are suppressed and the system superconducts at low temperatures [39, 40]. Moreover, a compressed tetragonal phase – also called 'collapsed' tetragonal phase – was identified at higher pressures. Subsequent susceptibility and transport measurements under hydrostatic conditions showed

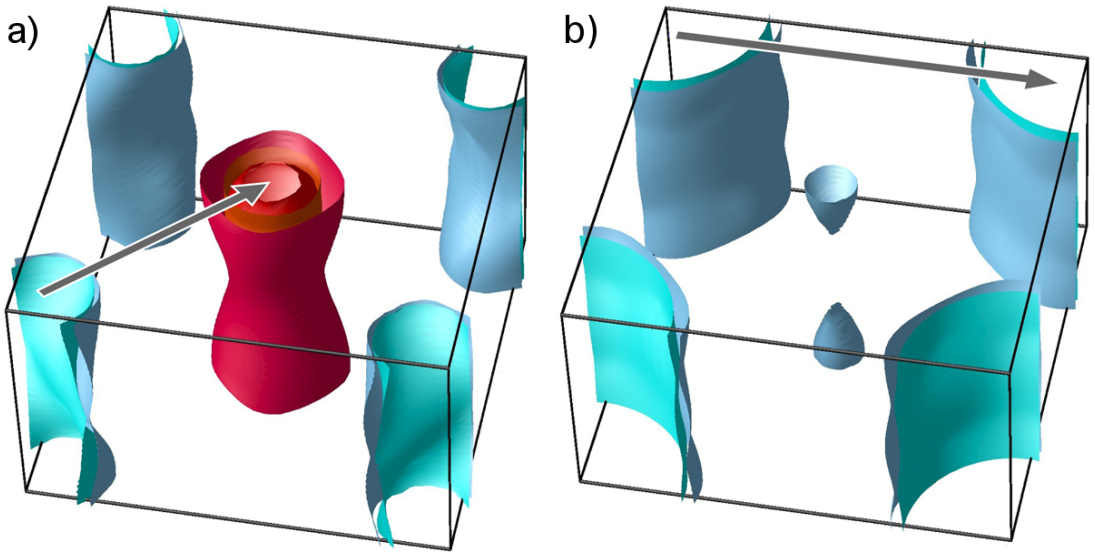

FIGURE 5.5: The Fermi surface of $BaFe_{1.94}Co_{0.06}As_2$ is shown on panel a), while the panel b) shows $K_{0.8}Fe_2Se_2$ in the two iron equivalent Brillouin zone. (figure adapted from [37])

at low temperatures and $P \sim 0.35$ GPa a sharp orthorhombic to collapsed tetragonal phase but no signature of superconductivity [41]. In contrast, recent neutron diffraction experiments on $CaFe_2As_2$ under uniaxial pressure along the c axis [42] indicate for pressures above 0.06 GPa and low temperatures the presence of an intermediate nonmagnetic tetragonal phase between the magnetic orthorhombic and the nonmagnetic collapsed tetragonal phases. This phase was identified by the authors as the phase responsible for superconductivity at $T = 10$ K. Other reports based on muon spin-relaxation measurements suggest the existence of superconductivity in the orthorhombic phase, raising the question whether superconductivity and magnetism can coexist [43].

$BaFe_2As_2$ shows an even more complex behavior under pressure. At ambient pressure it undergoes a phase transition from a metallic tetragonal phase to an orthorhombic antiferromagnetic phase at $T = 140$ K. Under pressure the gradual appearance of a superconducting dome has been observed by various groups [44] though the role of nonhydrostatic conditions is not yet well understood [36]. Recent synchrotron X-ray diffraction experiments under pressure [45] observe at $T = 300$ K a tetragonal to collapsed tetragonal phase transition at $P = 22$ GPa under hydrostatic conditions while this transition appears already at $P = 17$ GPa under nonhydrostatic conditions. On the other hand, the authors of Ref. [46] find at a lower temperature of $T = 33$ K that $BaFe_2As_2$ undergoes a phase transition from a magnetic orthorhombic to a nonmagnetic collapsed tetragonal phase at $P = 29$ GPa and report an anomaly in the As-Fe-As bond angles at 10 GPa that they ascribe to be of electronic origin. In contrast, high-pressure

neutron diffraction experiments [47] performed at $T = 17$ K find a tetragonal phase at 3 GPa and 6 GPa.

These experimental results show that the onset of superconductivity as well as the appearance of several structural phases at low temperatures in $CaFe_2As_2$ and $BaFe_2As_2$ are extremely sensitive to the pressure conditions [42, 48–50] and are a subject of intensive debate.

In particular, uniaxial pressure is currently being intensively discussed as a possible route towards modifying the structural, magnetic and even superconducting properties of these systems. A regular sample below its magnetic and structural transition temperatures displays an equal number of opposite twin orthorhombic domains, effectively canceling out its anisotropic properties. To circumvent this issue and obtain a single orthorhombic domain sample, uniaxial tensile stress has been widely employed to detwin iron pnictides like $BaFe_2As_2$ and $CaFe_2As_2$ [51–57] and unveil its anisotropic properties – which have been argued to originate from electronic nematic degrees of freedom. [58–60] Theoretically, although it is clear that in the tetragonal phase the applied uniaxial pressure acts as a conjugate field to the orthorhombic order parameter, condensing a single domain, [61] the nature of the detwinning process deep inside the orthorhombic phase remains an open question, since different mechanisms might be at play – such as twin boundary motion or reversal of the order parameter inside the domains. [57, 62]

Besides promoting detwinning, uniaxial strain has also been shown to affect the thermodynamic properties of the iron pnictides. Recent neutron scattering experiments on $BaFe_2As_2$ under compressive stress along the in-plane **b** direction reported a progressive shift to higher temperatures of the magnetic transition [54] - a behavior also seen in $BaFe_2\left(As_{1-x}P_x\right)_2$ by thermodynamic measurements. [63] - and an apparent reduction of the magnetic moment [54]. Moreover, Blomberg *et al.* observed a significant uniaxial structural distortion in $BaFe_2As_2$ under tensile stress, suggesting an enhanced response to external strain. [56] More recently, it was found that epitaxially strained thin films of FeSe on a $SrTiO_3$ substrate show an increase in critical superconducting temperatures up to 65 K, the highest reported T_c so far. [64] Clearly, crystal lattice strain plays a key role for the magnetic, structural and superconducting properties in Fe-based superconductors and a better understanding of the microscopic origin of such behavior is desirable.

In view of the controversy caused by the experimental uncertainty about the pressure conditions we performed *ab initio* density functional theory results for the electronic, magnetic and structural behavior of both systems under uniaxial and hydrostatic pressure conditions. Our approach consists of constant pressure structural relaxations, as presented in chapter 4, allowing us to probe the low-temperature portion of the phase

diagram in a relatively simple and straightforward way. With this approach we can treat *nonhydrostatic* conditions which are at the heart of this chapter.

Previous theoretical approaches which have examined the properties of the 122 family under hydrostatic pressure have employed either fixed volume structural optimizations [65] or molecular dynamics [66]. Recently, anisotropic pressure studies on $BaFe_2As_2$ based on ground state geometry calculations of more than 300 structures at different fixed volumes were reported in Ref. [67]. We find that uniaxial pressure along the c axis significantly reduces the transition pressures in both systems. $CaFe_2As_2$ shows for both pressure conditions an orthorhombic to collapsed tetragonal transition, though the transition is less abrupt when uniaxial pressure is applied. For $BaFe_2As_2$ we observe two phase transitions from orthorhombic to collapsed tetragonal through an intermediate nonmagnetic tetragonal phase. An analysis of the electronic bandstructure features near the critical pressures reveals the origin of the sensitivity of the systems to pressure conditions.

We also combine the results of density functional theory calculations with Ginzburg-Landau phenomenology to analyze the effects of uniaxial compressive stress as well as uniaxial tensile stress on the magnetic, electronic and structural properties of $BaFe_2As_2$ and $CaFe_2As_2$ at low temperatures, deep inside the ordered phase. Stress is measured in terms of equivalent hydrostatic pressure, $P = \mathrm{Tr}(\hat{\sigma})/3$, where $\hat{\sigma}$ is the stress tensor matrix and positive and negative pressures correspond to applying compressive and tensile stresses respectively. Our *ab initio*-derived estimates for the elastic constants in the orthorhombic phase agree well with experimental values. While no sign of a true structural or magnetic phase transition is observed in the range of pressures between -2 GPa and 2 GPa, at a critical pressure we observe a reversal of the magnetization, *i.e.* exchange of ferromagnetic (FM) and antiferromagnetic (AFM) directions, simultaneous to a discontinuous change in the orthorhombic order parameter $a-b$, which also changes sign. This behavior has important consequences on the orbital d_{xz} and d_{yz} occupancies and is also related to the shift of the magnetic ordering temperature, as we argue below.

Furthermore, by employing a phenomenological Ginzburg-Landau model, we show that this behavior is intimately connected to the magneto-elastic coupling of the system, which by itself acts as an intrinsic conjugate field to the orthorhombic order parameter. As the applied compressive stress is enhanced towards a critical value, it eventually overcomes the effects of the magneto-elastic coupling, rendering the zero-pressure state energetically unstable and resulting in a simultaneous reversal of the magnetization and the orthorhombic order parameter. Comparison of the DFT-derived critical uniaxial pressures for $CaFe_2As_2$ and $BaFe_2As_2$, combined with the Ginzburg-Landau result that the critical pressure is proportional to the magneto-elastic coupling, suggests that the

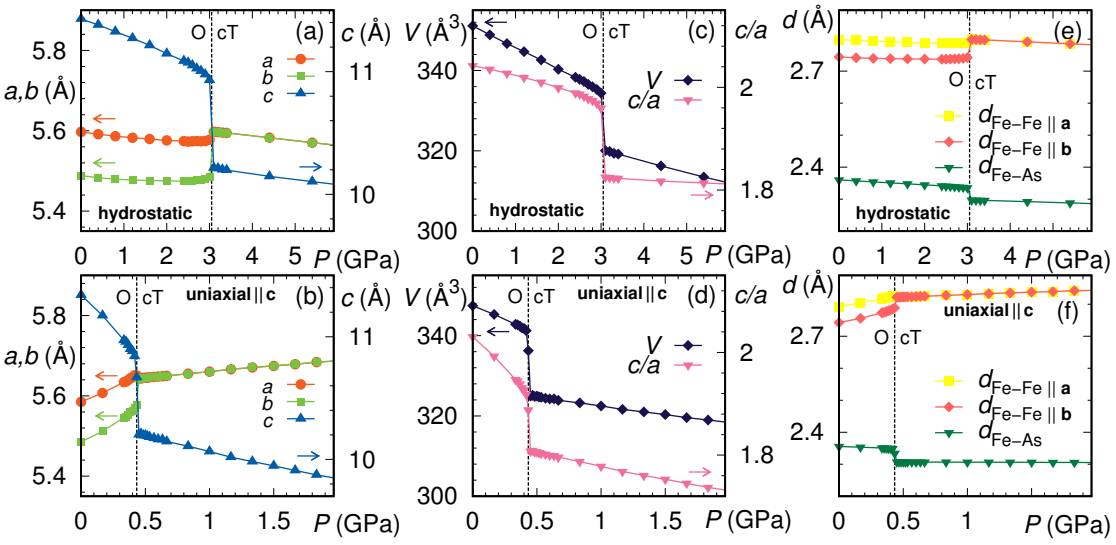

FIGURE 5.6: Structure of $CaFe_2As_2$ under hydrostatic and uniaxial pressure. Lattice parameters, a) and b), volume and axis ratio, c) and d), c) and d), selected bond lengths e) and f).

latter is larger in $CaFe_2As_2$ than in $BaFe_2As_2$. We also propose low-temperature detwinning measurements to compare the experimental critical pressure with our *ab initio* estimates in order to clarify the dominant mechanism behind the detwinning process of orthorhombic iron pnictide crystals.

Calculations were performed using the Vienna ab initio simulations package (VASP) [68] with the projector augmented wave (PAW) basis [10] in the generalized gradient approximation (GGA). Structural relaxations under hydrostatic pressure were carried out with the conjugate gradient (CG) method as implemented in the VASP package. The energy cutoff was set to 300 eV and a Monkhorst-Pack uniform grid of $(6 \times 6 \times 6)$ points was used for the integration of the irreducible Brillouin zone. For relaxations with the CG algorithm two cycles were performed in order to minimize the error caused by the Pulay stress. Note that the reported bond compressions of up to 7% at 50 GPa don't affect the precision of the PAW basis. In order to perform relaxations under uniaxial pressure we modified the fast inertial relaxation engine [22] (FIRE) algorithm to be able to handle full structural relaxations with an arbitrary stress tensor.

5.4 $CaFe_2As_2$ Under Hydrostatic and c-axis Uniaxial Pressure

In Fig. 5.6 we show the evolution of lattice parameters, volume and Fe-Fe, Fe-As distances under hydrostatic and (c-axis) uniaxial pressure for $CaFe_2As_2$. We find a first

order phase transition from a magnetic (stripe order) orthorhombic phase to a nonmagnetic collapsed tetragonal phase at $P_c = 3.05$ GPa ($P_c = 0.48$ GPa) under hydrostatic (uniaxial) pressure and at zero temperature we don't observe any intermediate tetragonal phase under uniaxial stress [42].

In hydrostatic conditions, a and b expand at the orthorhomic to collapsed tetragonal phase transition with b abruptly increasing in value, while c shows a significant collapse of 6.5% (Fig. 5.6 (a)) and the unit cell volume shows a sharp drop of about 4.3% (Fig. 5.6 (c)). The sudden expansion of b can be explained as a consequence of the Pauli principle [66]: As long as an antiferromagnetically ordered moment exists in the orthorhombic phase, Fe $3d$ orbitals may overlap to some degree along b direction, but in the paramagnetic state of the collapsed tetragonal phase, the same orbitals on neighboring Fe sites repel each other. The value of $c/a_t = 2.58$ with $a_t = a/\sqrt{2}$, indicates the onset of a collapsed tetragonal phase. Our results are in good qualitative agreement with experimental [40] observations, except for the overestimation of the critical pressure ($P_c^{\text{exp}} = 0.3$ GPa) also found in previous theoretical studies [65, 66]. Following the changes of the lattice parameters at P_c, the inplane Fe-Fe distances show a sharp increase at P_c while the out-of-plane Fe-As distance decreases (Fig. 5.6 (e)). Using the generalized Birch-Murnaghan $p - V$ equation of state [69] we obtained a bulk modulus $B = 70 \pm 3$ GPa at ambient pressure, while at P_c the bulk modulus jumps from 56 ± 3 to 105 ± 2 GPa. In order to obtain these estimates we performed a series of fits for every phase separately considering every pressure point of our data as a reference pressure. In this way we obtain the bulk modulus as a function of pressure.

In contrast to the hydrostatic case, when uniaxial pressure is applied (Fig. 5.6 (b)) the a and b lattice parameters expand significantly while c is compressed up to $P_c = 0.48$ GPa where a drop for c is observed while a and b continue to expand monotonously. The volume reduces by 3.4% and the ratio $c/a_t = 2.56$ at P_c (Fig. 5.6 (c)) denotes the entrance to a collapsed tetragonal phase, where magnetism is suppressed completely. The phase transition shifts to smaller P_c compared to hydrostatic pressure, which is in very good agreement with experiments under nonhydrostatic pressure conditions [42]. Nevertheless, the authors of Ref. [42] find for pressures above 0.06 GPa a stabilization of the high-temperature tetragonal structure down to temperatures below the superconducting transition. This phase is not seen in our calculations which may be related to the fact that at very low temperatures the tetragonal phase may be disappearing again (Fig. 1 of Ref. [42]).

In order to understand the differences in behavior observed between the hydrostatic and uniaxial pressures, we show in Fig. 5.7 the orbital weighted bandstructure and $k_z = 0$, $k_y = 0$ and $k_x + k_y = 0$ Fermi surface cuts of $CaFe_2As_2$ under hydrostatic

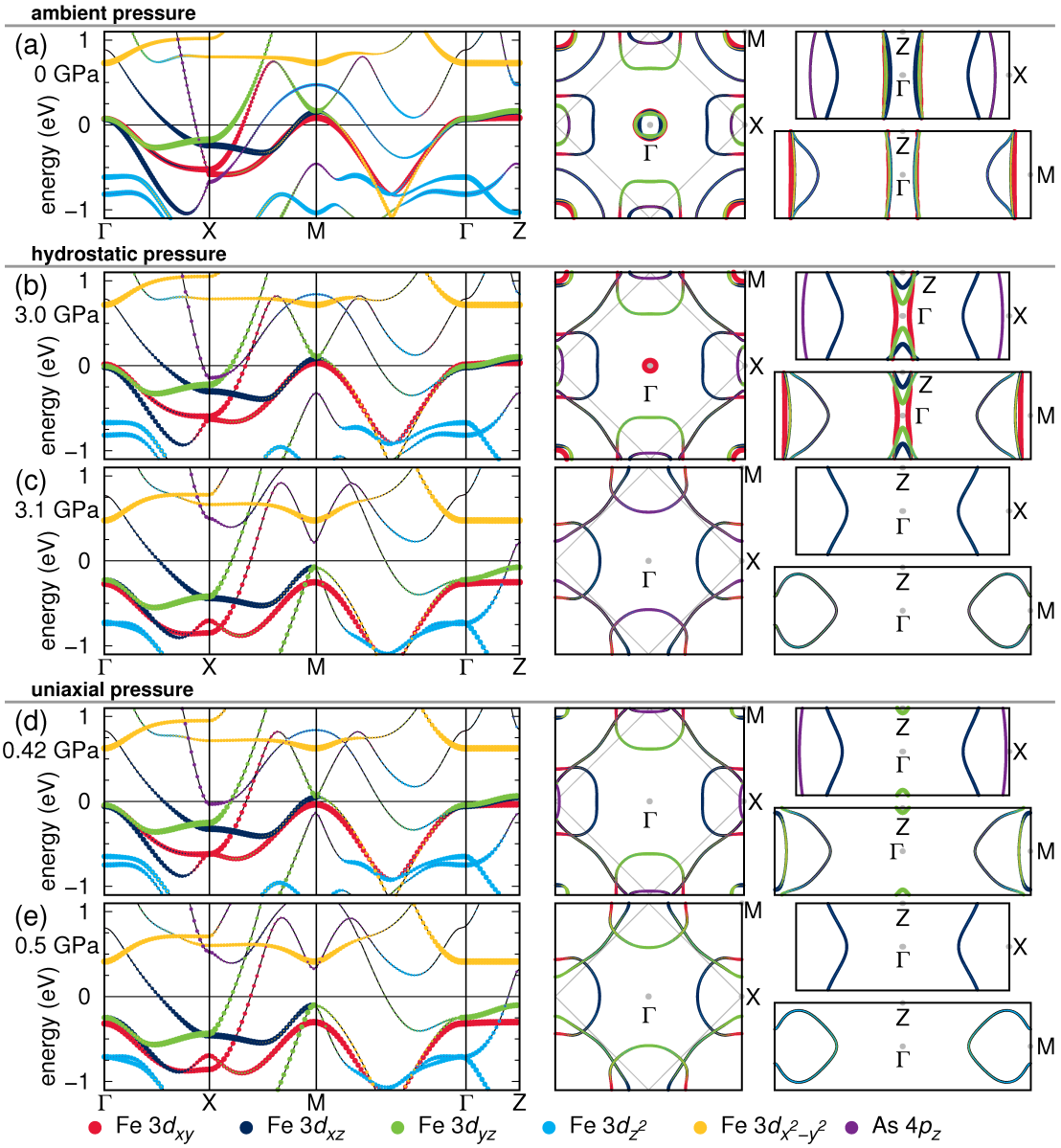

FIGURE 5.7: Bandstructure and $k_z = 0$, $k_y = 0$ and $k_x + k_y = 0$ Fermi surface cuts of $CaFe_2As_2$. For the orbital character, x and y point along the nearest neighbour Fe-Fe connections.

(Fig. 5.7 (b)-(c)) and uniaxial pressure (Fig. 5.7 (d)-(e)) at pressures below and above the phase transition. Bandstructures and Fermi surfaces were calculated using the full-potential local orbital (FPLO) basis [12]. The bandstructure and Fermi surface cuts at ambient pressure are also shown for comparison (Fig. 5.7 (a)). We use the orthorhombic space group $F\,mmm$ for all band structure plots in order to facilitate comparison. The behavior of the electronic structure in the vicinity of the Fermi energy is crucial for understanding the transition. Right below P_c both pressure conditions show a high density of Fe d_{xz}, d_{yz} and $d_{x^2-y^2}$ states at E_F (see in Fig. 5.7 (b) and (d) the Γ-Z

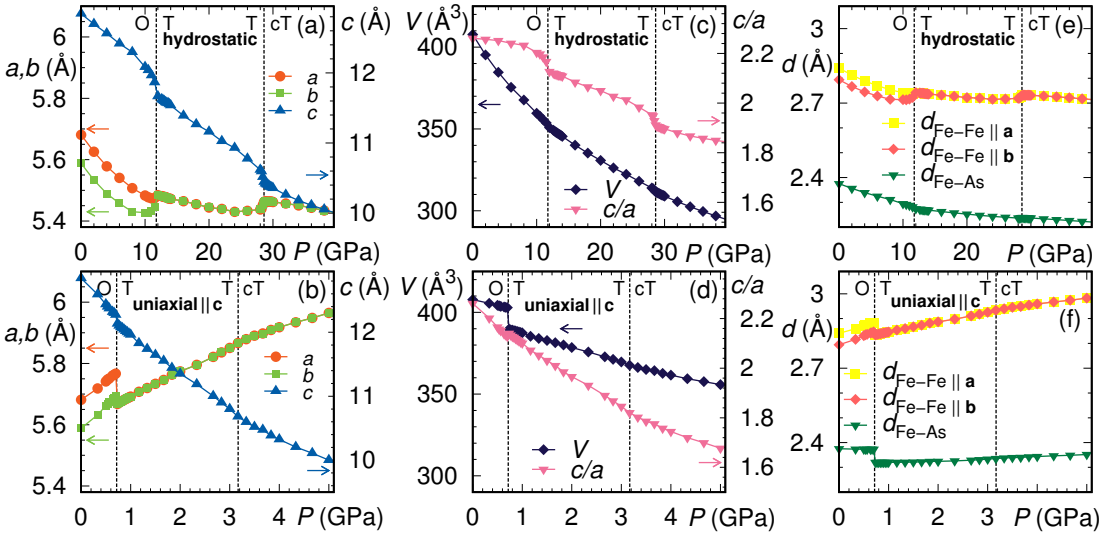

FIGURE 5.8: Structure of $BaFe_2As_2$ under hydrostatic and uniaxial pressure. Lattice parameters, a) and b), volume and axis ratio, c) and d), selected bond lengths e) and f).

path and near M) which are pushed away above P_c (Fig. 5.7 (c) and (e)) and the hole pockets at Γ disappear, suppressing possible nesting conditions. The compression along c enforces the interlayer As p_z-As p_z bonding [70] which can be related to the proximity of the As p_z band to E_F near P_c. Uniaxial stress is for this process more effective than hydrostatic pressure since a similar electronic behavior is reached at much smaller pressures as observed in Fig. 5.7 (d)-(e). In agreement with Ref. [71] the collapsed tetragonal phase sets in as soon as the Fe magnetic moment goes to zero. Note, that the changes in the electronic structure at the phase transition in the uniaxial pressure case (Fig. 5.7 (d) and (e)) are more subtle than for hydrostatic pressure, in agreement with the somewhat less abrupt change of the lattice as shown in Fig. 5.6 (b), (d) and (f).

Also, the shape of the Fermi surface derived from Fig. 5.7 in the collapsed tetragonal phase agrees well with the de Haas van Alphen measurements performed for $CaFe_2P_2$ ($c/a_t = 2.59$) where a highly dispersive topology in the c axis as well as the absence of the hole pocket at the Γ point has been reported [72] (compare Fig. 5.7 (c) and 5.7 (e) with Figs. 2 and 3 of Ref. [72]). The isoelectronic substitution of As by P in $CaFe_2As_2$ corresponds to application of chemical pressure and shows similar features to the collapsed tetragonal phase of $CaFe_2As_2$ obtained after application of (hydrostatic) pressure. The similarity of chemical pressure and applied pressure has already been discussed in Refs. [72] and [47]. In fact, comparison of our obtained $c/a_t = 2.58$ ratio and As position $z_{As} = 0.1358$ (hydrostatic) in the collapsed tetragonal phase of $CaFe_2As_2$ with the measured $c/a_t = 2.59$ and P position $z_P = 0.1357$ of $CaFe_2P_2$ shows the high resemblance between both crystal structures.

5.5 $BaFe_2As_2$ Under Hydrostatic and c-axis Uniaxial Pressure

We now proceed with the analysis of $BaFe_2As_2$. In Fig. 5.8 we present the changes in lattice parameters, volume and atomic distances under hydrostatic and uniaxial pressures for $BaFe_2As_2$. Similar to $CaFe_2As_2$, the critical pressures under uniaxial stress are reduced with respect to hydrostatic conditions. This observation was also reported by recent constant volume density functional theory calculations on $BaFe_2As_2$ under nonhydrostatic pressure [67]. $BaFe_2As_2$, contrary to $CaFe_2As_2$, shows two phase transitions. At $P_{c_1} = 11.75$ GPa ($P_{c_1} = 0.72$ GPa) we find a phase transition from an antiferromagnetic orthorhombic to a nonmagnetic tetragonal phase under hydrostatic (uniaxial) conditions. A second smooth phase transition to a collapsed tetragonal phase is obtained for $P_{c_2} = 28.6$ GPa ($P_{c_2} = 3.17$ GPa) (Fig. 5.8 (c)-(d)) [45]. High-pressure neutron diffraction experiments [47] as well as previous theoretical calculations under hydrostatic pressure conditions also find a phase transition to an intermediate tetragonal phase [65, 66] but recent syncrotron X-ray diffraction experiments under nonhydrostatic conditions see no signature of an intermediate tetragonal phase at low temperatures. Nevertheless, an anomaly in the As-Fe-As bond angles at $P \sim 10$ GPa [46] as well as a loss of magnetic moment [50] have been reported. This could be related to the phase transition that we find at $P_{c_1} = 11.75$ GPa where magnetism is suppressed. At higher pressures the agreement of the onset of the collapsed tetragonal phase with the X-ray diffraction data [46] is very good. Clearly the phase transitions in $BaFe_2As_2$ are less abrupt than in $CaFe_2As_2$.

The ambient pressure bulk modulus is estimated at 67 ± 4 GPa, in good agreement with experimentally reported values [46] of 82.9 ± 1.4 and 65.7 ± 0.8 GPa at 33 K and 300 K, respectively. At P_{c_1}, the bulk modulus abruptly increases from 98 ± 4 to 128 ± 3 GPa and at P_{c_2} it jumps from 150 ± 3 to 173 ± 2 GPa. This is in very good agreement with the experimental estimate of $B = 153 \pm 3$GPa for the collapsed tetragonal phase [46]. We also analyzed the Fe-As bond compressibility for $P = 9$ GPa (hydrostatic) and found $\kappa = 3.5 \times 10^{-3}$ GPa^{-1} which is in excellent agreement with $\kappa = 3.3 \times 10^{-3}$ GPa^{-1} obtained in an extended X-ray absorption fine structure (EXAFS) experiment [73]. In Fig. 5.9 (a), we show the comparison of the measured pressure dependence of the Fe-As bond distances [73] with our results. Due to different temperatures (experiment is performed at room temperature, theory at $T = 0$) our distances are shorter by about 0.02 Å (0.8%), but the overall agreement is good. In Fig. 5.9 (b), we show the comparison to the X-ray diffraction measurement of the Fe-As bond distances [46] over a large pressure range. The comparison is particularly good at low and at high pressures; in the tetragonal phase (11.75 GPa to 28.6 GPa) the deviations are a bit larger.

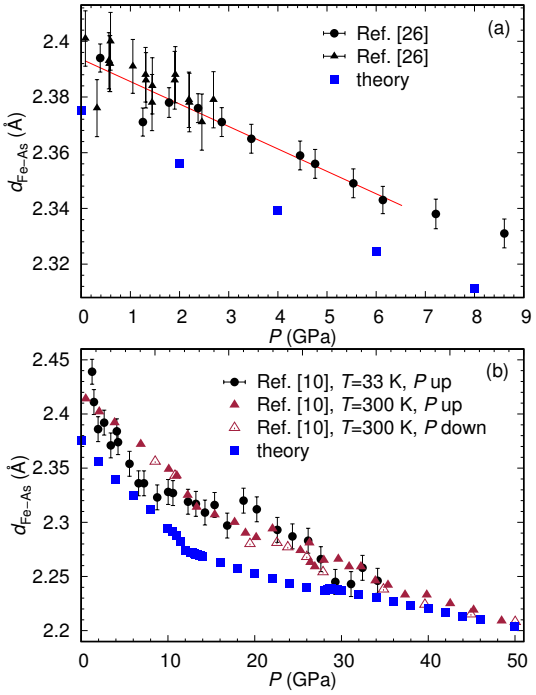

FIGURE 5.9: Comparison of $T = 0$ calculated (squares) and measured Fe-As bond distances in $BaFe_2As_2$ as a function of pressure. (a) d_{Fe-As} from XAFS experiment at $T = 298$ K (triangles, circles) [73]. (b) d_{Fe-As} from X-ray diffraction at $T = 33$ K (circles) and $T = 300$ K (triangles) [46]. P up and down indicate application and release of pressure.

In Fig. 5.10 we present the orbital weighted bandstructure and $k_z = 0$, $k_y = 0$ and $k_x + k_y = 0$ Fermi surface cuts of $BaFe_2As_2$ under hydrostatic (Fig. 5.10 (b)-(c)) and uniaxial pressure conditions (Fig. 5.10 (d)-(e)) at two pressures below and above the orthorhombic to tetragonal phase transition at $P_{c_1} = 11.75$ GPa ($P_{c_1} = 0.72$ GPa). Similar to $CaFe_2As_2$ we observe below P_{c_1} a high density of Fe d_{xz}, d_{yz} and $d_{x^2-y^2}$ states at E_F which is pushed down (less drastically than in $CaFe_2As_2$) for pressures above P_{c_1}. The hole pockets disappear at the Γ point and the Fe magnetic moment goes to zero. Here the As p_z band seems to be little affected at the critical pressure. In contrast, at $P_{c_2} = 28.6$ GPa ($P_{c_2} = 3.17$ GPa) (bandstructure not shown) the As p_z band is pushed towards the Fermi level indicating a strong As p_z-As p_z bonding while entering the collapsed tetragonal phase. These results show that under perfect hydrostatic or perfect uniaxial pressure conditions neither the intermediate tetragonal phase nor the collapsed tetragonal phase fulfill Fermi surface nesting conditions. In fact, we find that the structural parameters measured in Ref. [47] are similar to our calculated parameters far below P_{c_1} in the orthorhombic phase (except for the orthorhombic distorsion), where well defined hole pockets are found at the Γ point.

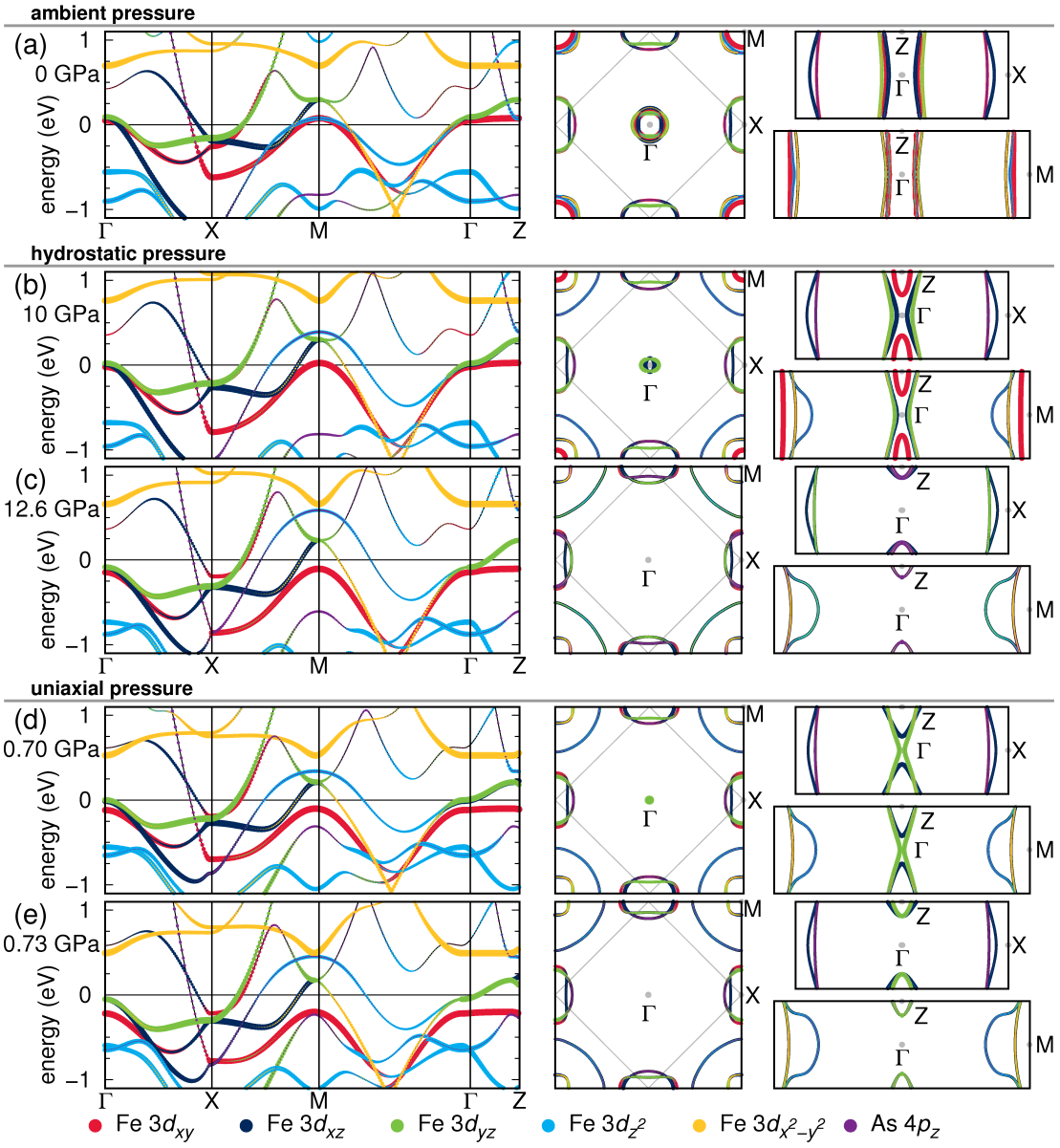

FIGURE 5.10: Bandstructure and $k_z = 0$, $k_y = 0$ and $k_x + k_y = 0$ Fermi surface cuts of $BaFe_2As_2$.

5.6 In Plane Application of Tensile and Compressive Stress on $BaFe_2As_2$

Starting from the low-temperature orthorhombic structure with stripe magnetic order, we performed structure relaxations under applied uniaxial tensile and compressive stresses along **a** (AFM direction), **b** (FM direction) and the plane-diagonal **a**+**b** direction for both $BaFe_2As_2$ and $CaFe_2As_2$ (see inset of Figure 5.11 (a)). We measure stress in units of the equivalent hydrostatic pressure, $P = \mathrm{Tr}(\hat{\sigma})/3$, with $\hat{\sigma}$ denoting the stress tensor matrix. We simulated pressures in the range between −3 GPa and 3 GPa. In the

tensile stress range, below −2.7 GPa we observe in both systems that, for stress along **a**, a sudden expansion in a and contraction in b and c axes occurs. A similar situation arises when pulling apart along **b**. This feature signals the extreme case of absence of bonding within the material, and for this reason this pressure range will be excluded from further discussion.

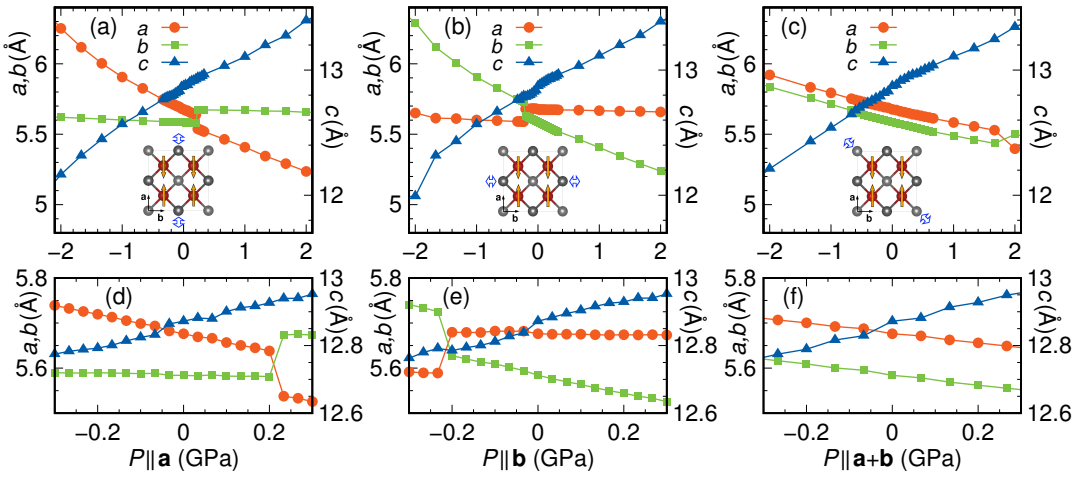

FIGURE 5.11: Evolution of the unit cell parameters in $BaFe_2As_2$ under application of uniaxial stress in the equivalent hydrostatic pressure range $[-2\,\text{GPa}, 2\,\text{GPa}]$ (a) along **a**, (b) along **b** and (c) along **a**+**b**. Panels (d)-(f) show the corresponding zoom of the pressure dependence of the lattice parameters in the range $[-0.3\,\text{GPa}, 0.3\,\text{GPa}]$. Negative pressures correspond to tensile stress while positive pressures correspond to compressive stress. Note, that the relationship between axes and iron moments shown in the inset in (a) is valid for $P \parallel \mathbf{a} < 0.22$ GPa, in (b) for $P \parallel \mathbf{b} > -0.22$ GPa. For a discussion of the reversal of AFM order, see the text.

Figure 5.11 shows the evolution of lattice parameters for $BaFe_2As_2$ as a function of uniaxial stress along **a**, **b** and **a**+**b**. We consider both compressive stress (positive pressure) and tensile stress (negative pressure). At $P = 0$ GPa, we have a (AFM direction) > b (FM direction). $BaFe_2As_2$ remains in the orthorhombic phase with nonzero increasing magnetic moment for large tensile stress (negative pressure). Pulling apart (*i.e.* $P < 0$) along the (longer) AFM direction **a** (Figure 5.11 (a)) the system expands along **a**, strongly compresses along **c** and shows almost no changes along **b**; similarly, pulling apart along the (shorter) FM direction **b** (Figure 5.11 (b)) b expands, c compresses and a shows almost no changes except at the pressure $P = -0.22$ GPa (Figure 5.11 (e)). At this point, $BaFe_2As_2$ shows a sudden jump in the orthorhombicity where **a** becomes the shorter axis and **b** becomes the longer axis. This interchange happens with a rotation of the magnetic order by 90 degrees, *i.e.* the FM direction becomes parallel to the **a** axis while the AFM direction becomes parallel to the **b** axis. We will discuss this feature further below. Note that tensile stress along **a**+**b** acts similarly on both **a** and **b** directions, which expand, while the **c** direction strongly compresses (Figures 5.11 (c) and (f)).

Under application of compressive stress (positive pressure), we observe in all three cases a strong expansion along **c** and a compression along the direction of applied stress (**a**, **b** or **a**+**b**). For the cases where pressure is applied along **a** or **b**, we observe almost no changes or a slight expansion along **b** and **a**, respectively. application of uniaxial stress along b by Dhital et al.. remains in all cases orthorhombic with nonzero decreasing magnetic moment. Since $a > b$ at zero stress, we observe the inversion of axes followed by a jump in orthorhombicity and a 90 degree rotation of the magnetization when stress is applied along **a** at $P = 0.22$ GPa (Figures 5.11 (a) and (d)). This inversion of axes, with $b > a$ for all higher compressive stress values means that the spin configuration shown in the inset of Figure 5.11 (a) should now be turned by 90 degrees, with **b** pointing along the AFM direction. Such an inversion is also observed for compressive stress along **a**+**b** at much larger pressures of $P = 2$ GPa.

Figure 5.12 shows the evolution of magnetic moment, volume and As height in $BaFe_2As_2$ as a function of stress. The three quantities show a clearly monotonic behavior independent of the applied stress direction except for small jumps at the pressures $P = -0.22$ GPa (for stress along **a**) and $P = 0.22$ GPa (for stress along **b**) where the tetragonal condition is almost fulfilled ($a \approx b$) (Figures 5.12 (b), (d), (f)). We also note here how magnetic moments in $BaFe_2As_2$respond to different direction of pressure application. The highest rate of suppression, of roughly $0.1\mu_B$/GPa is achieved when pressure is applied within *ab*-plane, while application of pressure along the **c**-axis actually results in magnetic moment increase by $0.03\mu_B$/GPa. Even though DFT calculations overestimate the value of the ordered Fe magnetic moment at $P = 0$ GPa, it is to be expected that the relative changes in magnetic moment should provide a reliable description of the situation of $BaFe_2As_2$ under pressure effects as shown in previous studies. [29, 65–67]

Except for the pressures $P = -0.22$ GPa (for stress along **a**) and $P = 0.22$ GPa (for stress along **b**), stress always enforces a certain degree of orthorhombicity and the system remains magnetically ordered with a decreasing ordered moment as a function of compressive stress (Figure 5.12 (a)). Moreover, since the c axis continually expands from negative to positive pressures, h_{As} increases accordingly as a function of stress (Figure 5.12 (e)). These features have a direct consequence on the electronic properties of the system.

As an illustration, we show the (non-spin polarized) Fermi surface of $BaFe_2As_2$ under application of uniaxial stress $P = -0.07$ GPa and $P = 1.7$ GPa applied along **a** in Figure 5.13 in the 1Fe/unit cell equivalent Brillouin zone. We would like to note that correlation effects beyond DFT as implemented in DFT+DMFT (dynamical mean field theory), which are known to give a good agreement between the calculated Fermi surfaces

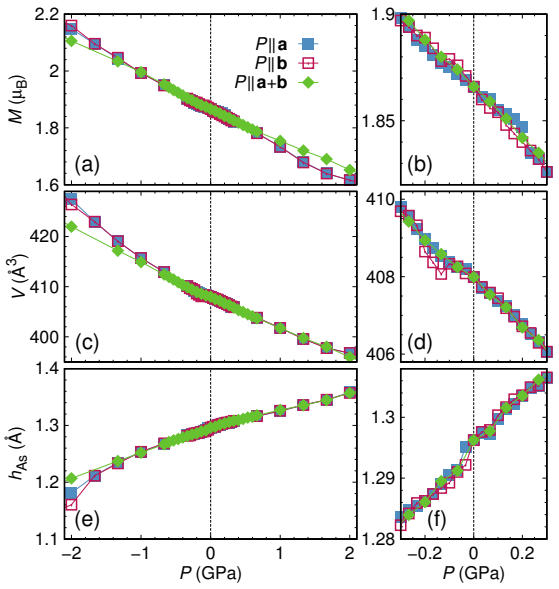

FIGURE 5.12: (a) Evolution of the magnetic moments of iron, (c) of the unit cell volume and (e) of the pnictogen height under uniaxial pressure in the range $[-2\,\text{GPa}, 2\,\text{GPa}]$. Panels (b), (d) and (e) show the corresponding zoom of the pressure dependence of these quantities in the range $[-0.3\,\text{GPa}, 0.3\,\text{GPa}]$. Negative pressures correspond to tensile stress while positive pressures correspond to compressive stress.

and angle-resolved photoemission measurements in the Fe pnictides, [74–78] have not been included here.

Modest tensile stress of 0.07 GPa leads to the disappearance of the $3d_{xy}$ hole pocket around $\bar{\Gamma}$ in the $k_z = 0$ plane (see Figure 5 (a) in Ref. [29]). On the other hand, when compressive stress is applied, the hole pockets around $\bar{\Gamma}$ significantly change in size, and additionally at a pressure of 1.7 GPa, small electron pockets, of majority $3d_{xy}$ and $3d_{z^2}$ character, appear along the $\bar{\Gamma} - \bar{M}$ directions of the BZ (Figures 5.13 (c) and (e)). The increase of the $3d_{xy}$ hole pocket size with increasing uniaxial stress can be explained by the reduction of Fe-Fe distance along the **a** axis, leading to an increased contribution of $3d_{xy}$ - $3d_{xy}$ bonding. In fact, the effects of tensile and compressive stress on the electronic structure shown for the example of stress along **a** can be seen also in our calculations for both stress along **b** and along **a**+**b**.

In Figure 5.14 we analyze the orbitally-resolved density of states at the Fermi level $N(E_\text{F})$. Applying stress both along **a** and **b** has the same effect on the total density of states of both $BaFe_2As_2$ and $CaFe_2As_2$, but there is a selective orbital order as shown in Figure 5.14. $N(E_\text{F})$ is predominantly of $3d_{xz}$ character when $a > b$ and of $3d_{yz}$ character when $a < b$. This means that the dominant character switches from $3d_{yz}$ to $3d_{xz}$ at $\hat{\sigma} \parallel \mathbf{a} \approx 0.22$ GPa, and from $3d_{xz}$ to $3d_{yz}$ at $\hat{\sigma} \parallel \mathbf{b} \approx -0.22$ GPa as expected.

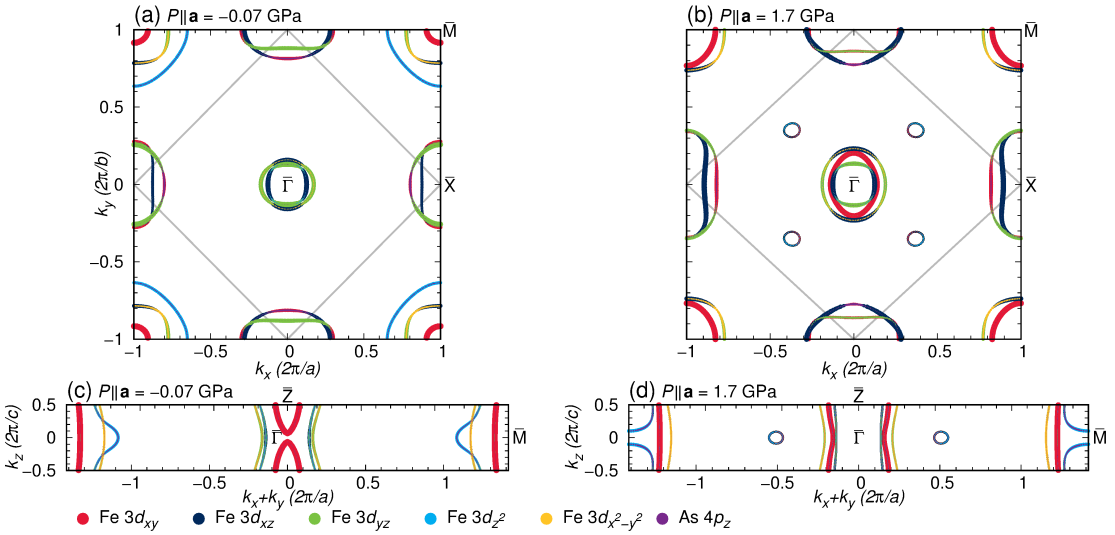

FIGURE 5.13: Evolution of the Fermi surface of $BaFe_2As_2$ under uniaxial stress applied along the **a** axis shown in the 1Fe/unit cell equivalent BZ (see Ref. [79] for the BZ path definition). Panels (a) and (b) show $k_z = 0$ cuts of the Fermi surface at pressures of -0.07 GPaand 1.7 GPa respectively, while panels (c) and (d) show vertical cuts along the diagonal of the BZ for pressures of -0.07 GPa and 1.7 GPa. Grey lines on panels (a) and (b) denote boundaries of the 2 Fe/unit cell BZ.

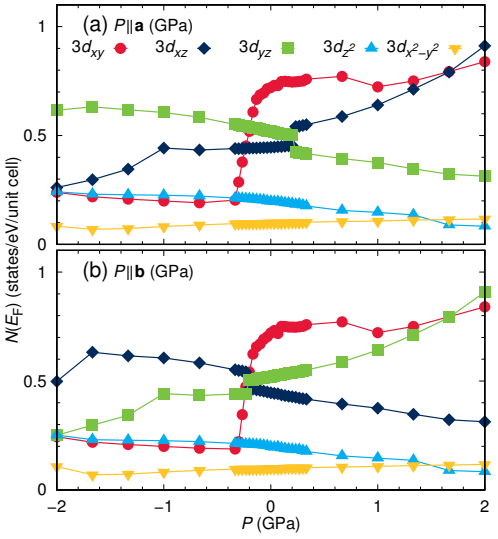

FIGURE 5.14: Evolution of the orbital resolved density of states of $BaFe_2As_2$ at the Fermi level $N(E_F)$ with stress (a) applied along **a**, and (b) along **b**. Lines joining the calculated points are a guide for the eye.

5.7 In Plane Application of Tensile and Compressive Stress on $CaFe_2As_2$

The lattice parameters of $CaFe_2As_2$ under application of compressive stress along **a**, **b** and **a**+**b** directions show a similar overall behavior compared to $BaFe_2As_2$ (see Figure 5.15) except for some important shifts of the pressures at which the system exchanges

the FM and AFM directions. When stress is applied along the **a** direction, we observe at $P = 0.67$ GPa a jump in the orthorhombic order parameter, with a sign-change, accompanied by a reversal of the magnetic AFM and FM directions. However, analogously to the case of $BaFe_2As_2$, this is not followed by a suppression of the magnetic moments of iron. In fact, the c axis expands with applied stress and at $P = 0.67$ GPa the c lattice parameter in $CaFe_2As_2$ is too large for the formation of an interlayer As-As covalent bond, necessary for a transition to a collapsed tetragonal phase and suppression of magnetic moments as observed under hydrostatic or c-axis uniaxial pressure. [29, 40, 66**?**] For tensile stress along the (shorter) **b** direction, the reversal of AFM and FM directions happens at $P = -0.33$ GPa followed by a jump in the orthorhombicity. Magnetic response of $CaFe_2As_2$is highly anisotropic aswell, but contrary to the case of $BaFe_2As_2$, magnetic moments in $CaFe_2As_2$are most effectively suppressed when pressure is applied along **c**, with rate of around $0.1\mu_B$/GPa, while application of pressure within ab-plane results in suppression of around $0.2\mu_B$/GPa.

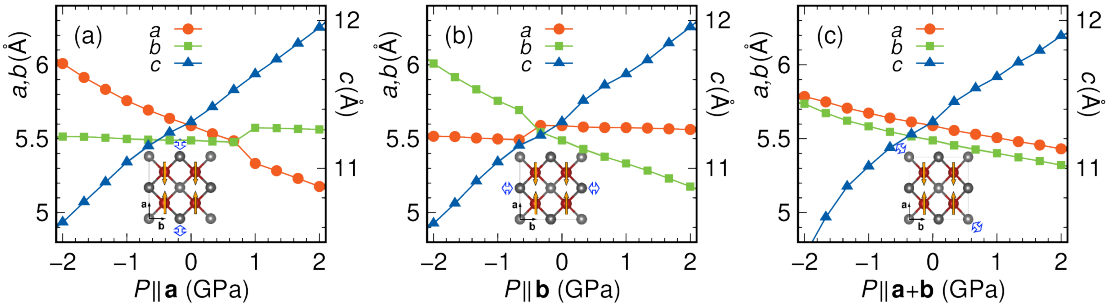

FIGURE 5.15: Evolution of the unit cell parameters in $CaFe_2As_2$ under the application of uniaxial stress in the range $[-2\,\text{GPa}, 2\,\text{GPa}]$ (a) along **a**, (b) along **b** and (c) along **a**+**b**. Negative pressures correspond to tensile stress while positive pressures correspond to compressive stress. Note, that the relationship between axes and iron moments shown in the inset in (a) is valid for $P \parallel \mathbf{a} < 1$ GPa, in (b) for $P \parallel \mathbf{b} > -0.6$ GPa.

In order to investigate the possibility of a structural and/or magnetic phase transition at higher pressures, we concentrate now on compressive stress along the diagonal of the ab-plane. We find that orthorhombicity is preserved up to 7.7 GPa, where a sharp transition to a tetragonal phase appears. This transition is of first-order type like the orthorhombic to collapsed tetragonal phase transition under application of hydrostatic or uniaxial pressure along the **c** axis [29] but in this case, changes of magnetic and structural properties take opposite directions; the **c** axis undergoes a sudden expansion of about 9.5%, and **a** and **b** axes contract while the iron magnetic moments order ferromagneticaly and sharply increase in value by around 25%. Interestingly though, contrary to the application of hydrostatic and uniaxial pressure along **c** axis, the volume change here is significantly smaller, namely an expansion by about 0.9%.

5.8 Elastic Constants in the Orthorhombic Phase and Magnetic Moment Suppression Rates

Using data for the response to the uniaxial stress along **a**, **b** and **c** [29] axes we can directly evaluate the elastic constants C_{ij} in $BaFe_2As_2$ and $CaFe_2As_2$ corresponding to the orthorhombic deformations. We define elastic constants to be such that

$$\sigma_i = \sum_j C_{ij} u_j,$$

where σ_i and u_j are stress and strain tensor components respectively, and indices i and j can be xx, yy, zz. Strains are defined to be $u_{xx} = (a - a_0)/a_0$, $u_{yy} = (b - b_0)/b_0$ and $u_{zz} = (c - c_0)/c_0$, where a_0, b_0 and c_0 are equilibrium unit cell dimensions ($P = 0$ GPa). We first directly obtain $S_{ij} = [C^{-1}]_{ij}$ by performing linear fits to $u_i(\sigma_j)$ and C is then obtained by inverting the resulting matrix. For $BaFe_2As_2$, the elastic constant matrix is

$$C = \begin{bmatrix} 95.2 \pm 4.3 & 20.4 \pm 3.4 & 40.8 \pm 4.5 \\ 27.3 \pm 4.8 & 130.8 \pm 6.1 & 64.0 \pm 7.0 \\ 43.7 \pm 4.5 & 47.7 \pm 4.6 & 81.0 \pm 5.6 \end{bmatrix} \text{GPa}$$

Utilizing Voigt and Reuss averages, [80] defined as

$$B_{\text{Voigt}} = \frac{1}{9}(C_{11} + C_{22} + C_{33} + 2(C_{12} + C_{13} + C_{23}))$$
$$B_{\text{Reuss}} = (S_{11} + S_{22} + S_{33} + 2(S_{12} + S_{13} + S_{13}))^{-1}$$

it is possible to estimate the bulk modulus. Voigt and Reuss averages yield 61.9 ± 5.1 GPa and 69.3 ± 7.5 GPa, respectively, which is in good agreement with our previous estimate [29] and the experimental value of 59 ± 2 GPa. [81] For $CaFe_2As_2$, the elastic constant matrix is given by

$$C = \begin{bmatrix} 148.7 \pm 18.5 & 45.6 \pm 12.3 & 55.5 \pm 12.7 \\ 63.9 \pm 21.4 & 182.4 \pm 18.4 & 81.2 \pm 17.5 \\ 61.4 \pm 14.7 & 63.1 \pm 11.4 & 68.8 \pm 11.3 \end{bmatrix} \text{GPa}$$

which results in bulk modulus of 84.3 ± 14.8 GPa and 77.7 ± 17.2 GPa using Voigt and Reuss averages, respectively. Both values are in good agreement with experimentally determined values of 82.9 ± 1.4 GPa [46] and the estimate based on fits to Birch-Murnaghan equation of state. [29]

It is interesting to compare this data with the estimates of the magnetic moment suppression rates. In general, for small applied pressure, magnetic moments is suppressed at

	$\Delta m/\Delta P[\mu_B/\text{GPa}]$ ($BaFe_2As_2$)	$\Delta m/\Delta P[\mu_B/\text{GPa}]$ ($CaFe_2As_2$)
P_{hyd}	-0.08	-0.05
$P_{\boldsymbol{a}}$	-0.09	-0.01
$P_{\boldsymbol{b}}$	-0.13	-0.02
$P_{\boldsymbol{c}}$	0.03	-0.13
$P_{\boldsymbol{a+b}}$	-0.12	-0.02

TABLE 5.1: Magnetic moment suppression rates in $BaFe_2As_2$ and $CaFe_2As_2$

a linear rate. The estimates for the suppression rate under different pressure conditions are summarized in table 5.1.

Although suppression rates under hydrostatic pressure are roughly comparable in $BaFe_2As_2$ and $CaFe_2As_2$ at 0.08 and 0.05 μ_B/GPa respectively, there is a marked difference in response to the uniaxial pressure where large anisotropy can be observed. While for $BaFe_2As_2$ the greatest suppression rates are achieved for in-plane application of pressure, in $CaFe_2As_2$ the largest suppression rates is achieved for application of pressure along the **c** axis. In both cases, the maximal suppression rate is around 0.13 μ_B/GPa. Remarkably, our calculations seem to indicate that application of **c** axis uniaxial pressure in $BaFe_2As_2$ weakly increases the magnetic moments, by around 0.03 μ_B/GPa. In-plane application of pressure in $CaFe_2As_2$ results in the maximal suppression rate of around 0.02 μ_B/GPa, which is a factor six reduction when compared to the **c** axis pressure application.

Compared with the elastic constants, it is noticeable that the relative softness of the magnetic moment parallels the relative softness of elastic constants in the corresponding direction of pressure application. In case of $CaFe_2As_2$ the magnetic moments are softest when pressure is applied along the **c** axis which is a direction of structural instability in the 122 family, explaining why the orthorhombic to collapsed tetragonal phase transition is so abrupt.

5.9 Phenomenological Ginzburg-Landau model

To aid the interpretation of the *ab initio* results, we develop a phenomenological magneto-elastic Ginzburg-Landau model to capture the physics of the simultaneous sign-changing jump of the orthorhombicity and reversal of the AFM and FM directions. As pointed out by Refs. [58, 60, 82], the magnetic structure of the iron pnictides consists of two interpenetrating Nèel sublattices, with magnetizations $\mathbf{M}_1$ and $\mathbf{M}_2$ of equal amplitude that can point either parallel or anti-parallel to each other (see Figure 5.16).

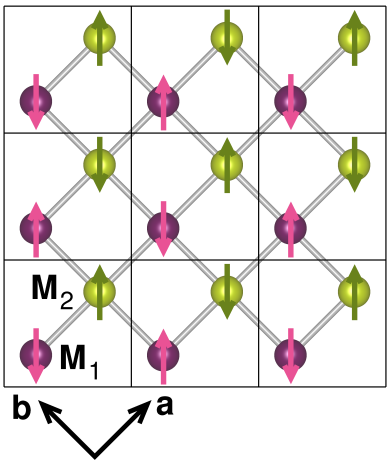

FIGURE 5.16: Magnetic structure of the iron pnictides consisting of two interpenetrating Nèel sublattices, with magnetizations $\mathbf{M}_1$ and $\mathbf{M}_2$.

By including also the orthorhombic order parameter $\delta = (a-b)/(a+b)$, we obtain the Ginzburg-Landau free energy:

$$\begin{aligned} F =& \frac{a_m}{4}\left(M_1^2+M_2^2\right)+\frac{u_m}{16}\left(M_1^2+M_2^2\right)^2-\frac{g_m}{4}\left(\mathbf{M}_1\cdot\mathbf{M}_2\right)^2 \\ &+\frac{a_s}{2}\delta^2+\frac{u_s}{4}\delta^4+\frac{\lambda}{2}\delta\left(\mathbf{M}_1\cdot\mathbf{M}_2\right)+\sigma\delta \end{aligned} \tag{5.1}$$

Here, $a_m \propto T - T_N$, $a_s \propto T - T_s$, $u_m, u_s > 0$, and $g_m > 0$. The last condition ensures that the ground state is the striped magnetic configuration (*i.e.* collinear $\mathbf{M}_1$ and $\mathbf{M}_2$). We also must have $u_m > g_m$ in order for the magnetic free energy to be bounded. $\lambda > 0$ is the magneto-elastic coupling and σ is the stress field conjugate to the orthorhombic order parameter. The sign of λ is set to describe the experimental observation that ferromagnetic bonds are shorter than anti-ferromagnetic bonds. Although this model does not take into account the physics of the magnetically-driven structural transition, which comes from fluctuations beyond the Ginzburg-Landau analysis we perform below, [60] it captures the main features of the *ab initio* results.

The magnetic ground state is completely determined by the magnitude $M = |\mathbf{M}_1| = |\mathbf{M}_2|$ and the relative angle θ between $\mathbf{M}_1$ and $\mathbf{M}_2$. Then, minimization of the free energy leads to three coupled equations for M, θ, and δ:

$$\frac{\partial F}{\partial M} = \left(a_m+\lambda\delta\cos\theta\right)M+\left(u_m-g_m\cos^2\theta\right)M^3=0 \tag{5.2}$$

$$\frac{\partial F}{\partial \delta} = a_s\delta+u_s\delta^3+\frac{\lambda}{2}M^2\cos\theta+\sigma=0 \tag{5.3}$$

$$\frac{\partial F}{\partial \theta} = \frac{g_m}{4}M^4\sin 2\theta-\frac{\lambda}{2}M^2\delta\sin\theta=0 \tag{5.4}$$

The last equation allows three possible solutions: $\theta = 0$, $\theta = \pi$, and $\cos\theta = \lambda\delta/\left(g_m M^2\right)$.

We focus only on the $\theta = 0, \pi$ solutions, since they are the energy minimum at zero stress. In the ordered phase, where $a_m, a_s < 0$, we obtain the self-consistent equation for δ:

$$-\left(|a_s| + \frac{\lambda^2}{2\left(u_m - g_m\right)}\right)\delta + u_s\delta^3 = -\frac{\lambda\,|a_m|\cos\theta}{2\left(u_m - g_m\right)} - \sigma \tag{5.5}$$

For $\sigma = 0$, the mean-field equations and the free energy are invariant upon changing $\delta \to -\delta$ and $\theta \to \theta + \pi$. Thus, we have two degenerate solutions: $\delta > 0$ and anti-parallel $\mathbf{M}_1$ and $\mathbf{M}_2$, $\theta = \pi$, (denoted hereafter δ_+) or $\delta < 0$ and parallel $\mathbf{M}_1$ and $\mathbf{M}_2$, $\theta = 0$ (denoted hereafter δ_-). The presence of a finite strain σ lifts this degeneracy. After defining:

$$\begin{aligned}
\delta_0 &= \sqrt{\frac{|a_s|}{u_s} + \frac{\lambda^2}{2u_s\left(u_m - g_m\right)}} \\
h_+ &= \frac{1}{u_s\delta_0^3}\left(\frac{\lambda\,|a_m|}{2\left(u_m - g_m\right)} - \sigma\right) \\
h_- &= \frac{1}{u_s\delta_0^3}\left(\frac{\lambda\,|a_m|}{2\left(u_m - g_m\right)} + \sigma\right)
\end{aligned} \tag{5.6}$$

the self-consistent equations for the two solutions δ_+ and δ_- become simply:

$$-\left(\frac{\delta_\pm}{\delta_0}\right) + \left(\frac{\delta_\pm}{\delta_0}\right)^3 = \pm h_\pm \tag{5.7}$$

and we obtain analytic expressions for the two possible solutions:

$$\begin{aligned}
\delta_\pm\left(h_\pm\right) = \pm\,\delta_0 \Bigg[&\left(\frac{h_\pm}{2} + \sqrt{\frac{h_\pm^2}{4} - \frac{1}{27}}\right)^{\frac{1}{3}} \\
&+ \left(\frac{h_\pm}{2} - \sqrt{\frac{h_\pm^2}{4} - \frac{1}{27}}\right)^{\frac{1}{3}}\Bigg]
\end{aligned} \tag{5.8}$$

The interplay between the external stress field σ and the magneto-elastic coupling λ becomes evident in Eqs. (5.6)-(5.8). For $\sigma = 0$, λ acts as an external field of the same magnitude for both the δ_+ and δ_- solutions, *i.e.* it gives rise to non-zero $h_+ = h_-$ in the equations of state (5.7), making these two solutions degenerate. Now, consider that for $\sigma = 0$ the system chooses the minimum δ_+ (*i.e.* $\delta > 0$ and $\theta = \pi$). By increasing the external stress to a small value $\sigma > 0$, the effective field h_+ is suppressed, whereas the field h_- is enhanced. Although the solution δ_- (*i.e.* $\delta < 0$ and $\theta = 0$) has a lower energy, the solution δ_+ is still a local minimum, since the effective field h_+ is still finite. This situation persists until σ increases to the point where the field h_+ becomes negative and large enough to make the δ_+ solution not a local minimum.

In particular, to determine when the δ_+ solution ceases to be a local minimum, we analyze when one of the eigenvalues of the Hessian matrix $\left(\partial^2 F/\partial q_i \partial q_j\right)$ becomes negative (with generalized coordinates $q_i = M,\ \delta,\ \theta$). The three eigenvalues μ_i are given by:

$$\begin{aligned}\mu_\pm = &\frac{1}{2}\left[a_s + 3u_s\delta^2 + 2M^2\left(u_m - g_m\right)\right] \\ &\pm \frac{1}{2}\sqrt{\left[a_s + 3u_s\delta^2 - 2M^2\left(u_m - g_m\right)\right]^2 + 4\lambda^2 M^2} \\ \mu_0 = &\frac{M^2}{2}\left(g_m M^2 - \lambda\delta\cos\theta\right)\end{aligned} \tag{5.9}$$

For the δ_+ ($\delta > 0,\ \theta = \pi$) solution, the only eigenvalue that can become negative with increasing σ is μ_-. We find that this happens when the condition $\frac{\delta_+}{\delta_0} = -\frac{3}{2}h_+$ is met, corresponding to an effective field $h_+ = -\frac{2}{3\sqrt{3}}$, *i.e.* to the critical stress:

$$\begin{aligned}\sigma_c = &\frac{\lambda\left|a_m\right|}{2\left(u_m - g_m\right)} \\ &+ \frac{2u_s}{3\sqrt{3}}\left(\frac{\left|a_s\right|}{u_s} + \frac{\lambda^2}{2u_s\left(u_m - g_m\right)}\right)^{3/2}\end{aligned} \tag{5.10}$$

At $\sigma = \sigma_c$, the solution $\delta > 0,\ \theta = \pi$ is not a local minimum any longer and the system jumps to the new minimum with $\delta < 0,\ \theta = 0$, where not only the sign of the orthorhombicity is reversed, but also the angle between the magnetizations of the two sublattices (*i.e.* the AFM and FM directions). This behavior is shown in Figure 5.17 for a particular set of parameters.

To compare with the DFT results, we performed a slight modification with respect to the calculations presented in the previous section. To ensure that the external stress couples mainly to the orthorhombic mode δ and not to the longitudinal elastic mode ϵ, such that it does not change the volume of the system, we simultaneously applied positive (compressive) pressure along **a** and equal-amplitude negative (tensile) pressure along **b**. By doing this, we avoid terms such as $M^2\epsilon$ in the free energy, rendering the comparison between the *ab initio* and the Ginzburg-Landau results more meaningful.

The *ab initio* obtained behavior of δ as function of σ, defined in the way described above, is shown also in Figure 5.17.

We find a qualitative agreement with the Ginzburg-Landau results, showing that the external stress indeed competes with the magneto-elastic coupling, helping the system to overcome the energy barrier between the δ_+ ($\delta > 0,\ \theta = \pi$) and δ_- ($\delta < 0,\ \theta = 0$) solutions. A quantitative comparison becomes difficult because the DFT calculations are performed deep in the ordered phase, where higher order terms in the Ginzburg-Landau expansion become more important. Furthermore, it is also possible that some of the magnetic parameters (a_m, u_m and g_m) have themselves some implicit pressure

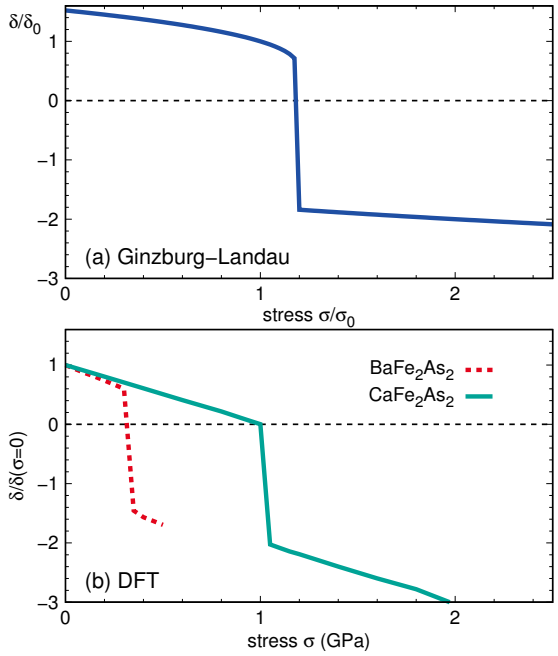

FIGURE 5.17: (a) Orthorhombic order parameter $\delta = \frac{a-b}{a+b}$ (in units of $\delta_0 = \sqrt{\frac{|a_s|}{u_s} + \frac{\lambda^2}{2u_s(u_m-g_m)}}$) as function of the applied stress σ (in units of $\sigma_0 = \frac{\lambda|a_m|}{2(u_m-g_m)}$). We used parameters such that $\frac{\lambda|a_m|}{2(u_m-g_m)u_s\delta_0^3} = 2$. The jump happens when the $\delta > 0$ solution is no longer a local minimum, and is accompanied by a reversal of the angle between the two-sublattice magnetizations $\mathbf{M}_1$ and $\mathbf{M}_2$, *i.e.* a reversal of the AFM and FM directions. (b) DFT results for the strain-dependent orthorhombic order parameter $\delta \equiv \frac{a-b}{a+b}$. The blue curve is for $BaFe_2As_2$ and the red curve, for $CaFe_2As_2$.

dependence in this regime. Nevertheless, we can use Eq. (5.10) as a benchmark to discuss differences in the $BaFe_2As_2$ and $CaFe_2As_2$ compounds. Clearly, Eq. (5.10) shows that σ_c increases with increasing magneto-elastic coupling. Therefore, the fact that σ_c is three times larger for $CaFe_2As_2$ than for $BaFe_2As_2$ suggests that, all other parameters being equal, the magneto-elastic coupling is larger in $CaFe_2As_2$ than in $BaFe_2As_2$. This may have important impact on the coupled magnetic and structural transitions displayed by these compounds, as discussed in Refs. [60, 82, 83], and as such deserves further investigation in the future.

5.10 Summary

In summary, we have presented finite pressure density functional theory calculations which allow the investigation of *nonhydrostatic* pressure conditions. Our finite pressure relaxed structures show good agreement with the available experimental data (volume, Birch-Murnaghan values and compressibilities) though our magnetic moments in the orthorhombic phase are larger than the observed experimental values. We expect that this overestimation affects mostly the values of P_c. Comparison of our calculated Fe-As

bond distances at different pressures with measured distances [73] shows good agreement. Also, available de Haas van Alphen measurements performed for $CaFe_2P_2$ [72] agree well with our predicted Fermi surface shapes for $CaFe_2As_2$ in the collapsed tetragonal phase. This overall agreement with experimental observations demonstrates that the presented constant pressure calculations provide a reliable theoretical prediction of structures under nonhydrostatic pressure conditions, allowing for arbitrary stress tensors in future studies. Such calculations can complement experiments and help identify the precise degree of hydrostaticity. We find that uniaxial stress along the c axis considerably reduces the critical pressures for $CaFe_2As_2$ and $BaFe_2As_2$. This behavior can be understood by the fact that the phase transitions are strongly dictated by the electronic properties in the vicinity of the Fermi energy, as shown by our electronic structure analysis. While $CaFe_2As_2$ undergoes a magnetic orthorhombic to a non-magnetic collapsed tetragonal phase for both pressure conditions and no indication of an intermediate tetragonal phase is observed under uniaxial stress, $BaFe_2As_2$ shows two phase transitions from a magnetic orthorhombic to a collapsed tetragonal phase through an intermediate nonmagnetic tetragonal phase for both pressure conditions. All nonmagnetic phases show a disappearance of the hole pockets at the Γ point suppressing possible Cooper pair scattering channels between electron and hole pockets. Such scattering channels have been discussed to be important for the superconductivity in $BaFe_2As_2$ [84]. More experiments need to be done in order to understand the origin of the superconducting phase observed in these materials under various pressure conditions.

We have also analyzed the effects of tensile and compressive stress along **a**, **b** and **a**+**b** on $BaFe_2As_2$ and $CaFe_2As_2$ by means of DFT calculations under constant stress conditions with the help of the FIRE algorithm, combined with a phenomenological Ginzburg-Landau model. Starting from the low-temperature magnetically ordered orthorhombic phase, we found in the pressure range between -2 GPa and 2 GPa no real structural phase transitions in both systems except for a pronounced orthorhombicity jump accompanied by a 90 degree rotation of the magnetic order. FM and AFM directions are interchanged, as are the orbital occupations d_{xz} and d_{yz}. This inversion of axes is a direct consequence of the interplay between the intrinsic magneto-elastic coupling and the applied stress, as revealed by our Ginzburg-Landau analysis. The proportionality between the critical stress where this inversion happens and the value of the magneto-elastic coupling suggets that in $CaFe_2As_2$ the magnetic and structural degrees of freedom are more strongly coupled than in $BaFe_2As_2$, which may be related to the differences observed in their magnetic and structural transitions. [83] We also point out that the estimates for the bulk moduli of $BaFe_2As_2$ and $CaFe_2As_2$ derived from our *ab initio* results are in good agreement with the experimental measurements.

Our calculations also provide important insight on the impact of uniaxial stress on the magnetic properties of the pnictides. Fig. 5.12 shows that the magnetic moment at zero temperature always decreases (increases) with compressive (tensile) stress, regardless of the axis that is perturbed. Unlike the jump in the orthorhombicity and the reversal of the FM and AFM directions, this is a consequence not of the magneto-elastic coupling, but of the changes in the pnictogen height promoted by the uniaxial stress. This is an important prediction of our first-principle calculations that can be tested experimentally. Interestingly, recent neutron diffraction experiments [54] on $BaFe_2As_2$ observed that upon application of compressive stress along the b axis, the magnetic moment is suppressed from $1.04\mu_B$ to $0.87\mu_B$. Given the small values of applied pressure, it could be that this suppression is due to a reduction of the volume fraction of the domains whose moments are oriented out of the scattering plane, as pointed out by the authors of Ref. [54]. Nevertheless, in view of our current results, it would be interesting to either apply higher pressures to completely detwin the samples at low temperatures or to apply tensile stress to make a comparison with the case of compressive stress. We note that Ref. [54] also found an enhancement of the magnetic transition temperature T_N in the same detwinned samples. Phenomenological models [63, 82, 85] attribute this effect to changes in the magnetic fluctuation spectrum of the paramagnetic phase promoted by the uniaxial stress. In this regard, it would be interesting in future *ab initio* studies to systematically investigate the changes in the nesting feature of the Fermi surface (Fig. 5.13) as function of the uniaxial stress - specifically, changes in the (π, π) susceptibility peak.

Finally, we comment on the impact of our results to the understanding of the detwinning mechanism of iron pnictide compounds. In the tetragonal phase, rather small uniaxial stress $P < 10$ MPa is enough to completely detwin the sample, giving rise to a single domain. [54, 57, 62] This can be understood as fluctuations above the structural transition temperature giving rise to long-range order in the presence of a symmetry-breaking field. [60] The situation is however very different deep in the orthorhombic phase, where twin domains are already formed. Experimentally, it is known that larger pressures are necessary to completely detwin the system in this case, [57, 62] although specific values have not been reported, to our knowledge. One possible detwinning mechanism is the reversal of the orthorhombicity of one domain type, while the domain walls remain pinned. This corresponds precisely to the situation studied here, where the orthorhombicity jumps at a certain critical uniaxial pressure. Our *ab initio* results show that such a critical pressure for $BaFe_2As_2$ would be around 200 MPa – one order of magnitude larger than the pressure values necessary to detwin the sample in the tetragonal phase.

Of course, other mechanisms can also give rise to detwinning in the ordered phase, such as domain wall motion. Therefore, we propose controlled detwinning experiments at low

temperatures in $BaFe_2As_2$ to measure the critical pressure necessary to form a single domain. Values comparable to the ones discussed here would be a strong indication for reversal of the order parameter inside fixed domains. Which mechanism is at play in the iron pnictides may have important consequences for the understanding of the impact of the external stress on the anisotropic properties measured in detwinned samples – particularly the in-plane resistivity anisotropy, [56, 57, 60] which is likely affected by domain wall scattering. [86]

Chapter 6

Band Structure Unfolding

Often, when one wants to compare electronic properties of qualitatively similar crystal structures, with unit cells of different size, a difficulty arises because structure with larger unit cell will have more complicated band structure, making comparison more difficult and obscuring important features shared with the crystal possessing a simpler unit cell. This is especially true when doped compounds or crystals with any kind of defects are of interest.

To go around this difficulty, we have developed an unfolding procedure which can leverage both translational and point group symmetry to effectively reduce the unit cell by an integer factor, resulting in a reduction of a number of bands by the same factor.

In this chapter we will first explain how bandstructure folding occurs and then we will present a simple method by which the unfolding can be achieved. This method proceeds through a simple transformation between two Bloch basii and is similar to the other recently developed methods [87–93]. We then presents our more general method, based on group theory considerations. This method was inspired by the proposal to use the glide mirror group to unfold the tight-binding model of LaFeAsO[79]. And finally, we apply the method to various problems which arise when studying the iron pnictide family of materials.

This chapter requires some level of familiarity with the representation theory of space groups. Since this is not a very common topic outside the specialized area of crystallography a short overview of group theory and representation theory of space groups is given in appendix A.

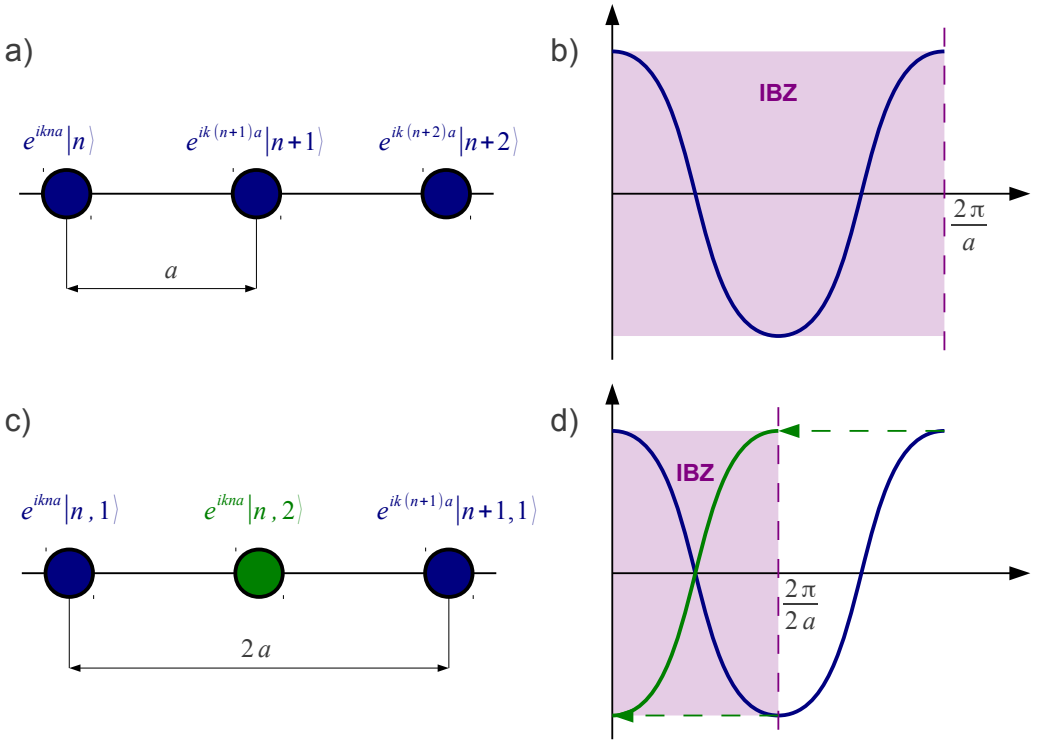

FIGURE 6.1: Simple example of band structure folding in one dimension. Panel (a) shows a unit cell consisting of one atom. Above each atom, its contribution to the Bloch state is shown. The resulting one band bandstructure is on panel (b). The panels (c) and (d) show what happens when the unit cell is doubled. In this case, each unit cell has two atoms, indexed with 1 and 2. Resulting in a folded bandstructure as-shown on panel (d).

6.1 Problem of Folding

Before detailing out the unfolding procedure we have to clarify the folding. Figure 6.1 shows a simple example of a one dimensional crystal with a unit cell consisting of a single atom. If we assume one localized state $|n\rangle$ at every atomic site n, with N being the total number of sites, then the resulting Bloch states are of the form

$$|k\rangle = \sum_{n=1}^{N} e^{ikna}|n\rangle.$$

There will be a total of N Bloch states, characterized by the wave numbers $k \in [0, .., 2\pi/a)$. Since for every k there is only one Bloch state, the Hamiltonian will be one-dimensional and as a result there will be only one band, shown on Figure 6.1 (a).

If we now take the same one dimensional crystal, and double the unit cell so that it contains two atoms, marked as 1 and 2 (see Figure 6.1 c), the resulting Bloch states are

$$|q,\mu\rangle = \sum_{n=1}^{N/2} e^{2iqna}|n,\mu\rangle$$

where $\mu = 1, 2$ indexes atoms in the unit cell. Since the Bloch states $|q,\mu\rangle$ span the same space as states $|k\rangle$, there will have to be N of them, as in the case of one atom per unit cell, but now there will be half as much wave numbers $q \in [0, .., \pi/a)$ and for every q there will be two states $|q, \mu = 1, 2\rangle$. Because of this, the corresponding Hamiltonian at q will be two dimensional and as a result the bandstructure will have two bands (Figure 6.1 d).

However, these two bands hold no more information than the one band shown on Figure 6.1 (a) to which there is a one to one correspodence shown by dashed green arrows, which is called folding. The goal of the unfolding procedure we have developed is to find the inverse mapping.

6.2 Transformation of the Bloch Basis

Let us remove the constraint of a one dimensional crystal with one atom per unit cell and consider a crystal lattice with N unit cells located at sites $\boldsymbol{R}_n$, with $n = 1, ..., N$, with each unit cells containing M orthonormal atomic orbitals $|\mu\rangle$ located at positions $\boldsymbol{r}_\mu$ relative to the $\boldsymbol{R}_n$. Here we allow the possibility of multiple orbitals occupying the same site, since we would like to describe the multi-orbital systems. Let $\hat{\mathrm{H}}$ be the Hamiltonian. At an arbitrary k-point $\boldsymbol{k}$ of the Brillouin Zone, bands are obtained by diagonalizing the projection of the Hamiltonian to the subspace spanned by the Bloch states

$$|\boldsymbol{k},\mu\rangle = \frac{1}{\sqrt{N}} \sum_{n=1}^{N} e^{i\boldsymbol{k}\cdot\boldsymbol{R}_n}|\boldsymbol{R}_n,\mu\rangle \tag{6.1}$$

where the index μ enumerates the atomic orbitals within the unit cell. Projection of the Hamiltonian, is achieved by the following relation

$$\hat{\mathrm{H}}_{\boldsymbol{k}} = \hat{\mathrm{P}}_{\boldsymbol{k}}\hat{\mathrm{H}}\hat{\mathrm{P}}_{\boldsymbol{k}} = \sum_{\mu,\nu=1}^{M} |\boldsymbol{k},\mu\rangle\langle\boldsymbol{k},\mu|\hat{\mathrm{H}}|\boldsymbol{k},\nu\rangle\langle\boldsymbol{k},\nu| \tag{6.2}$$

where the projectors $\hat{\mathrm{P}}_{\boldsymbol{k}}$ are given by

$$\hat{\mathrm{P}}_{\boldsymbol{k}} = \sum_{\mu=1}^{M} |\boldsymbol{k},\mu\rangle\langle\boldsymbol{k},\mu| \tag{6.3}$$

In this case, there will be N k-points within the BZ and at each k-point there will be M bands.

If we now divide the same crystal lattice into smaller number of larger unit cells, we will obtain a lattice described by N/s vectors $\boldsymbol{S}_p$, and Ms atomic orbitals within each unit cell, where $s > 1$. The resulting Supercell Brillouin Zone (SBZ) will be covered with the N/s k-points, and there will be Ms bands.

The resulting increase in number of bands represents the bandstructure folding.The goal of the procedure presented here is to obtain the bandstructure in the BZ starting from the bandstructure obtained in the SBZ. This can be achieved by projecting and determining matrix elements of the relation (6.2) in the subspace spanned by the supercell Bloch states

$$|\boldsymbol{q}, \mu, i\rangle = \sqrt{\frac{s}{N}} \sum_{p=1}^{N/s} e^{i\boldsymbol{q}\cdot\boldsymbol{S}_p} |\boldsymbol{S}_p, \mu, i\rangle \tag{6.4}$$

where $\boldsymbol{q}$ is from SBZ, and $i = 1..s$ enumerates copies of the orbitals from unit cell in the supercell (See figure 6.2).

Since, practically, in our calculations we start from the Hamiltonian evaluated in the supercell basis, we can achieve this, by simply finding the matrix elements of the projectors (6.3) in the basis (6.4). Those are given by

$$P^{\alpha\beta,ij}_{\boldsymbol{k},\boldsymbol{q}} = \langle \boldsymbol{q}, \alpha, i|\hat{\mathrm{P}}_{\boldsymbol{k}}|\boldsymbol{q}, \beta, j\rangle = \sum_{\mu=1}^{M} \langle \boldsymbol{q}, \alpha, i|\boldsymbol{k}, \mu\rangle\langle \boldsymbol{k}, \mu|\boldsymbol{q}, \beta, j\rangle = \sum_{\mu=1}^{M} \left(a^{\mu\alpha,i}_{\boldsymbol{k},\boldsymbol{q}}\right)^* a^{\mu\beta,j}_{\boldsymbol{k},\boldsymbol{q}} \tag{6.5}$$

Coefficients $a^{\mu\alpha,i}_{\boldsymbol{k},\boldsymbol{q}}$ are given by

$$a^{\mu\alpha,i}_{\boldsymbol{k},\boldsymbol{q}} = \langle \boldsymbol{k}, \mu|\boldsymbol{q}, \alpha, i\rangle = \frac{\sqrt{s}}{N} \sum_{n=1}^{N} \sum_{p=1}^{N/s} e^{-i\boldsymbol{k}\cdot\boldsymbol{R_n}} e^{i\boldsymbol{q}\cdot\boldsymbol{S_p}} \langle \boldsymbol{R}_n, \mu|\boldsymbol{S}_p, \alpha, i\rangle \tag{6.6}$$

To evaluate scalar products, instead of summing over the unit cells in the first sum, we sum over supercells, and then over the replicas of the unit cells within the supercell. This results in the following changes

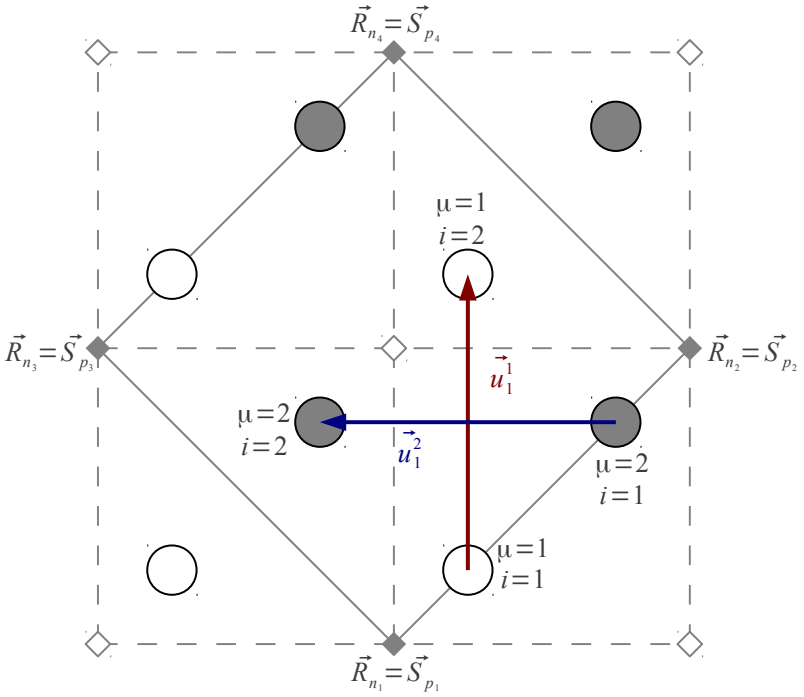

FIGURE 6.2: Unit cell boundaries are given by dashed gray lines, while supercell boundaries are given by solid gray lines. Grey diamonds mark unit cell sites which will become supercell locations while white diamonds mark unit cell sites which will be internal to the supercell. Colored vectors denote how the unit cell orbitals are duplicated in the supercell.

$$\sum_{n=1}^{N} \longrightarrow \sum_{r=1}^{N/s} \sum_{j=1}^{s}$$
$$\boldsymbol{R}_n \longrightarrow \boldsymbol{S}_r + \boldsymbol{u}_j^{\mu}$$
$$|\boldsymbol{R}_n, \mu\rangle \longrightarrow |\boldsymbol{S}_r, \mu, j\rangle$$

where every vector $\boldsymbol{R}_n$ is decomposed into a sum of supercell location $\boldsymbol{S}_p$ and position of the unit cell replica relative to the supercell location $\boldsymbol{u}_j^{\mu}$ (this position depends on the orbital index μ because for different orbitals the unit cell replicas might be positioned differently with respect to the supercell origin $\boldsymbol{S}_p$ as shown on figure 6.2). With these changes taken into account it is easy to evaluate $a_{\boldsymbol{k},\boldsymbol{q}}^{\mu\alpha}$

$$a^{\mu\alpha}_{\boldsymbol{k},\boldsymbol{q}} = \frac{\sqrt{s}}{N}\sum_{j=1}^{s} e^{-i\boldsymbol{k}\cdot\boldsymbol{u}^{\mu}_{j}} \sum_{r=1}^{N/s}\sum_{p=1}^{N/s} e^{-i\boldsymbol{k}\cdot\boldsymbol{S}_r} e^{i\boldsymbol{q}\cdot\boldsymbol{S}_p} \langle \boldsymbol{S}_r, \mu, j | \boldsymbol{S}_p, \alpha, i\rangle = \\ \frac{\sqrt{s}}{N}\sum_{j=1}^{s} e^{-i\boldsymbol{k}\cdot\boldsymbol{u}^{\mu}_{j}} \sum_{r=1}^{N/s}\sum_{p=1}^{N/s} e^{-i\boldsymbol{k}\cdot\boldsymbol{S}_r} e^{i\boldsymbol{q}\cdot\boldsymbol{S}_p} \delta_{rp}\delta_{\mu\alpha}\delta_{ij} = \\ \frac{\sqrt{s}}{N} e^{-i\boldsymbol{k}\cdot\boldsymbol{u}^{\mu}_{i}} \delta_{\mu\alpha} \sum_{p=1}^{N/s} e^{-i(\boldsymbol{k}-\boldsymbol{q})\cdot\boldsymbol{S}_p} = \frac{1}{\sqrt{s}} e^{-i\boldsymbol{k}\cdot\boldsymbol{u}^{\mu}_{i}} \delta_{\mu\alpha}\delta_{\boldsymbol{k}_f,\boldsymbol{q}} \quad (6.7)$$

where $\boldsymbol{k}_f$ is the vector $\boldsymbol{k}$ refolded back to the supercell Brillouin zone. Putting (6.7) into (6.5) gives the final result

$$P^{\alpha\beta,ij}_{\boldsymbol{k},\boldsymbol{q}} = \frac{1}{s} e^{i\boldsymbol{k}\cdot(\boldsymbol{u}^{\alpha}_{i}-\boldsymbol{u}^{\beta}_{j})} \delta_{\alpha\beta}\delta_{\boldsymbol{k}_f,\boldsymbol{q}} \quad (6.8)$$

Unfolding of the band structure can then be achieved in practical ab-initio calculations by operating with the matrix defined by (6.8) onto a column containing projections of the Hamiltonian eigenvectors $|\boldsymbol{k}, n\rangle$ onto some set of orthonormal localized states $|\mu\rangle$, which is usually provided by most density-functional theory codes.

6.3 Group Theoretical Formulation of the Unfolding

The important aspect of the Bloch basis (6.1) and the projectors (6.3) is that they are concepts deeply rooted in the symmetry principles. Let us consider the same crystal lattice as in the previous section. The lattice remains invariant when translated by $\boldsymbol{R}_n$. Thus, the electronic Hamiltonian from (1.4), must be invariant under the same set of translations. One of the basic statements of group theory in physics is that the eigenstates of the Hamiltonian can be classified according to the irreducible representations of its group of symmetries [94]. This stems from the fact that the operators representing the action of the symmetry operations commute with the Hamiltonian, which in turn means that irreducible subspaces for a given group of symmetries will be invariant under the action of the Hamiltonian.

The well known result[95] is that the translation group $\mathbb{T}$ of the periodic lattice of N sites will have N inequivalent irreducible representations $D^{(\boldsymbol{k})}$, where $\boldsymbol{k}$ belongs to the first Brillouin zone. The translations are represented by $\hat{\mathrm{D}}^{(\boldsymbol{k})}(\boldsymbol{R}_n) = e^{-i\boldsymbol{k}\cdot\boldsymbol{R}_n}$. For every irreducible representation $D^{(\boldsymbol{k})}$, a projector onto the corresponding irreducible space can be defined

$$\hat{\mathrm{P}}_{\boldsymbol{k}} = \frac{1}{N}\sum_{n=1}^{N} e^{i\boldsymbol{k}\cdot\boldsymbol{R}_n}\hat{\mathrm{T}}(\boldsymbol{R}_n)$$

This is just another way to define a projector given in (6.3). The projection of the Hamiltonian by the projectors $\hat{\mathrm{P}}_{\boldsymbol{k}}$ brings the Hamiltonian to the block diagonal form

$$\hat{\mathrm{H}} = \begin{bmatrix} \hat{\mathrm{H}}_{\boldsymbol{k}_1} = \hat{\mathrm{P}}_{\boldsymbol{k}_1}\hat{\mathrm{H}}\hat{\mathrm{P}}_{\boldsymbol{k}_1} & & & \\ & \hat{\mathrm{H}}_{\boldsymbol{k}_2} & & \\ & & \ddots & \\ & & & \hat{\mathrm{H}}_{\boldsymbol{k}_N} \end{bmatrix}$$

since $\boldsymbol{k}$-th irreducible subspace of the translation group is invariant under the action of the Hamiltonian. As a consequence, the Hamiltonian diagonalization is achieved by separate diagonalization of every sub-block $\hat{\mathrm{H}}_{\boldsymbol{k}_i}$.

The Bloch states (6.1) are a result of the action of the projectors $\hat{\mathrm{P}}_{\boldsymbol{k}}$ onto a set of localized states $|\mu\rangle$, centered around origin of the lattice at positions $\boldsymbol{r}_\mu$ since $|\boldsymbol{R}_n, \mu\rangle = \hat{\mathrm{T}}(\boldsymbol{R}_n)|\mu\rangle$.

Let us now assume that the lattice possesses symmetries additional to those contained in $\mathbb{T}$. In that case, the full group of symmetries will in general be a spacegroup $\mathbb{S}$ such that $\mathbb{T} \triangleleft \mathbb{S}$. The irreducible representations of $\mathbb{S}$ can be induced from the irreducible representations of $\mathbb{T}$ as shown in the Appendix A. Let the operators $\hat{\mathrm{C}}_i = [\hat{\mathrm{U}}_i|\boldsymbol{\tau}_i], i = 1, ..., F$ be the left coset representatives of $\mathbb{S}$ with respect to $\mathbb{T}$, where $\hat{\mathrm{U}}_i$ is a point group operation and $\boldsymbol{\tau}_i$ is a fractional translation. We allow $\hat{\mathrm{C}}_i$ to be the pure fractional translations, but not the pure point group operations since the goal of unfolding is to increase the translational periodicity of the lattice. An element of $\mathbb{S}$ can be written as

$$\hat{\mathrm{S}}_{n,i} = \hat{\mathrm{C}}_i\hat{\mathrm{T}}(\boldsymbol{R}_m) = [\hat{\mathrm{U}}_i|\hat{\mathrm{U}}_i\boldsymbol{R}_m + \boldsymbol{\tau}_i] = [\hat{\mathrm{U}}_i|\boldsymbol{R}_n + \boldsymbol{\tau}_i]$$

and is represented by

$$\hat{\Delta}^{(\boldsymbol{k},\alpha)}(\hat{\mathrm{S}}_{n,i}) = e^{-i\boldsymbol{k}\cdot(\boldsymbol{R}_n+\boldsymbol{\tau}_i)}\hat{\Delta}_{\mathrm{C}}^{(\boldsymbol{k},\alpha)}(\hat{\mathrm{U}}_i) \tag{6.9}$$

To simplify, we will assume that $\boldsymbol{k}$ in (6.9) is a high symmetry point for all $\hat{\mathrm{U}}_i$. In this case, the irreducible representations of the little co group $\Delta_{\mathrm{C}}^{(\boldsymbol{k},\alpha)}$ will be one dimensional. Since the irreducible representations are unitary, this means that $\hat{\Delta}_{\mathrm{C}}^{(\boldsymbol{k},\alpha)}(\hat{\mathrm{U}}_i)$ will be roots of unity and we can write

$$\hat{\Delta}_{\mathrm{C}}^{(\boldsymbol{k},\alpha)}(\hat{\mathrm{U}}_i) = \mathrm{e}^{i\alpha f_i/F} \tag{6.10}$$

for appropriately chosen $0 \leq f_i < F$. The numbers f_i, with respect to addition modulo F make up a group isomorphic to the little co group. Since, with this parametrization, $\hat{\Delta}_{\mathrm{C}}^{(\boldsymbol{k},0)}(\hat{\mathrm{U}}_i) = 1$ for every i, index $\alpha = 0$ will correspond to the unit representation of the little co-group.

In cases where $\hat{\mathrm{C}}_i$ are pure fractional translations, which corresponds to the case of the translational unfolding described in the previous section, it is not necessary to use the induction procedure described in the appendix A.3 . The fractional translations $\boldsymbol{\tau}_i$ modulo $\mathbb{T}$ comprise an Abelian group $\mathbb{T}_{\mathrm{f}}$ which is either cyclic, or a direct product of one or more cyclic groups and thus its irreducible representations are easily found. Since $\mathbb{S} = \mathbb{T}\mathbb{T}_{\mathrm{f}}$, irreducible representations of $\mathbb{S}$ are a simple product of irreducible representations of $\mathbb{T}$ and $\mathbb{T}_{\mathrm{f}}$.

Finally, when (6.9) an (6.10) are taken into account, a generalization of the projectors (6.3) can be written

$$\hat{\mathrm{P}}_{\boldsymbol{k}\alpha} = \frac{1}{NF}\sum_{n=1}^{N}\sum_{i=1}^{F} \mathrm{e}^{i\alpha f_i/F} e^{i\boldsymbol{k}\cdot(\boldsymbol{R}_n+\boldsymbol{\tau}_i)}[\hat{\mathrm{U}}_i|\boldsymbol{R}_n + \boldsymbol{\tau}_i] \tag{6.11}$$

The very important fact here is that there are now NF projectors $\hat{\mathrm{P}}_{\boldsymbol{k}\alpha}$, which means that the Hamiltonian can be put into the block diagonal form with NF instead of N blocks which was the case with the projectors (6.3). This means that every block will result in N/F bands and the unfolding can be achieved.

In order to be able to use the projectors (6.11) to generate the generalization of the Bloch states (6.4), we have to determine how operators $[\hat{\mathrm{U}}_i|\boldsymbol{R}_n + \boldsymbol{\tau}_i]$ act on the localized states $|\mu\rangle$. Since the action of translation by a lattice vector is already know, we are only concerned here with the action of point group operator and the fractional translation $\hat{\mathrm{C}}_i = [\hat{\mathrm{U}}_i|\boldsymbol{\tau}_i]$. The action of point group operators $\hat{\mathrm{U}}_i$ will transform the localized states within the unit cell into each other, while the action of fractional translations $\boldsymbol{\tau}_i$ can move localized states from one unit cell into another. However, since in the projector (6.11) we sum over all operations of $\mathbb{S}$, we can just shift the indexing, so that the transformed localized states are translated back into the original unit cell. Now, the total action of $\hat{\mathrm{C}}_i$ can just be written as

$$\hat{\mathrm{C}}_i|\boldsymbol{R}_n, \mu\rangle = \sum_{\nu=1}^{M}|\boldsymbol{R}_n, \nu\rangle W_{\nu\mu}(\hat{\mathrm{C}}_i) \tag{6.12}$$

so that the generalization of the Bloch basis (6.4) will be

$$|\boldsymbol{k},\mu,\alpha\rangle = \frac{1}{NF}\sum_{n=1}^{N}\sum_{i=1}^{F}\sum_{\nu=1}^{M} \mathrm{e}^{i\alpha f_i/F} e^{i\boldsymbol{k}\cdot(\boldsymbol{R}_n+\boldsymbol{\tau}_i)}|\boldsymbol{R}_n,\nu\rangle W_{\nu\mu}(\hat{\mathrm{C}}_i) \tag{6.13}$$

In order to be able to unfold, as in the previous section, we need to determine the matrix elements of the projectors (6.11) in the Bloch basis (6.4)

$$P^{\mu\nu}_{\boldsymbol{k}\alpha} = \langle \boldsymbol{k},\mu|\hat{\mathrm{P}}_{\boldsymbol{k}\alpha}|\boldsymbol{k},\nu\rangle = \frac{1}{NF}\sum_{n=1}^{N}\sum_{i=1}^{F}\sum_{\nu=1}^{M} \mathrm{e}^{i\alpha f_i/F} e^{i\boldsymbol{k}\cdot(\boldsymbol{R}_n+\boldsymbol{\tau}_i)}\langle \boldsymbol{k},\mu|[\hat{\mathrm{U}}_i|\boldsymbol{R}_n+\boldsymbol{\tau}_i]|\boldsymbol{k},\nu\rangle$$

where the matrix elements of the space group operators are

$$\langle \boldsymbol{k},\mu|[\hat{\mathrm{U}}_i|\boldsymbol{R}_n+\boldsymbol{\tau}_i]|\boldsymbol{k},\nu\rangle = \frac{1}{N}\sum_{p=1}^{N}\sum_{q=1}^{N} e^{i\boldsymbol{k}\cdot(\boldsymbol{R}_q-\boldsymbol{R}_p)}\langle \boldsymbol{R}_p,\mu|[\hat{\mathrm{U}}_i|\boldsymbol{R}_n+\boldsymbol{\tau}_i]|\boldsymbol{R}_q,\nu\rangle$$

Since

$$\langle \boldsymbol{R}_p,\mu|[\hat{\mathrm{U}}_i|\boldsymbol{R}_n+\boldsymbol{\tau}_i]|\boldsymbol{R}_q,\nu\rangle = \sum_{\gamma=1}^{M}\langle \boldsymbol{R}_p,\mu|\boldsymbol{R}_q+\boldsymbol{R}_n,\gamma\rangle W_{\gamma\nu}(\hat{\mathrm{C}}_i) = \delta(\boldsymbol{R}_p-\boldsymbol{R}_n-\boldsymbol{R}_q)W_{\mu\nu}(\hat{\mathrm{C}}_i)$$

When all of this is put together, the final expression for the projector matrix elements is simplified to

$$P^{\mu\nu}_{\boldsymbol{k}\alpha} = \frac{1}{\sqrt{F}}\sum_{i=1}^{F} \mathrm{e}^{i\alpha f_i/F} e^{i\boldsymbol{k}\cdot\boldsymbol{\tau}_i} W_{\mu\nu}(\hat{\mathrm{C}}_i) \tag{6.14}$$

For the case of the translational unfolding the expression (6.14) is identical to (6.8). However, the meaning of the terms in (6.14) is much more obvious. Once the irreducible representations of the space group $\mathbb{S}$ are known, in order to evaluate the projector matrix elements, it is necessary to evaluate the matrices $\hat{\mathrm{W}}(\hat{\mathrm{C}}_i)$.

Let us assume that every unit cell contains P sites $\boldsymbol{s}_p$. Every site $\boldsymbol{s}_p$ is the center of the M_p localized states $|p,\alpha\rangle$. where $\alpha = 1,...,M_p$ and $\sum_{p=1}^{P} M_p = M$. We can now

understand the index μ of the localized state $|\mu\rangle$ as a composite index $\mu = (p, \alpha)$. The action of the operators $\hat{\mathrm{C}}_i$ permutes the sites $\boldsymbol{s}_p$ so that it's action on the sites can be represented by the permuation matrix $\hat{\mathrm{K}}$ whose matrix elements are

$$K_{pq} = \delta(\boldsymbol{s}_q - [\hat{\mathrm{C}}_i \boldsymbol{s}_p]_{\mathrm{mod}\mathbb{T}})$$

where $[\hat{\mathrm{C}}_i \boldsymbol{s}_p]_{\mathrm{mod}\mathbb{T}}$ denotes the action of $\hat{\mathrm{C}}_i$ on the sites $\boldsymbol{s}_p$ modulo lattice translation, ie. the position $\hat{\mathrm{C}}_i \boldsymbol{s}_p$ is translated back into the original unit cell.

In addition to the permutation action, the point group part $\hat{\mathrm{U}}_i$ of the operators $\hat{\mathrm{C}}_i$ has an action on states at every site given by the matrix $\hat{\mathrm{L}}^p(\hat{\mathrm{U}}_i)$. Practically, index α in $|p, \alpha\rangle$ usually stands for the angular momentum quantum numbers $\alpha = (l, m)$. This means that the matrices $\hat{\mathrm{L}}^p(\hat{\mathrm{U}}_i)$ are transformation matrices in the spherical harmonic basis. Finally, the matrix elements of $\hat{\mathrm{W}}(\hat{\mathrm{C}}_i)$ are given by

$$W_{\mu\nu}(\hat{\mathrm{C}}_i = [\hat{\mathrm{U}}_i|\boldsymbol{\tau}_i]) = K_{pq}(\hat{\mathrm{C}}_i) L^p_{\alpha\beta}(\hat{\mathrm{U}}_i)$$

where $\mu = (p, \alpha)$ and $\nu = (q, \beta)$.

If we now turn back to the representative of an arbitrary operation from $\mathbb{S}$

$$\hat{\Delta}^{(\boldsymbol{k},\alpha)}(\hat{\mathrm{S}}_{n,i}) = \mathrm{e}^{i\alpha f_i/F} e^{-i\boldsymbol{k}\cdot(\boldsymbol{R}_n + \boldsymbol{\tau}_i)}$$

we can see that the induced irreducible representations are differentiated by the factor α in the first exponential term. This means that, for any two induced irreducible representations $\Delta^{(\boldsymbol{k},\alpha)}$ and $\Delta^{(\boldsymbol{k},\beta)}$, we can find a $\boldsymbol{k}_{\alpha\beta}$ from the Brillouin zone, such that

$$\begin{aligned} \boldsymbol{k}_{\alpha\beta} \cdot \boldsymbol{R}_n &= 0 \\ \boldsymbol{k}_{\alpha\beta} \cdot \boldsymbol{\tau}_i &= (\beta - \alpha) f_i / F \end{aligned} \tag{6.15}$$

which then implies

$$\Delta^{(\boldsymbol{k},\beta)} = \Delta^{(\boldsymbol{k}+\boldsymbol{k}_{\alpha\beta},\alpha)}$$

In other words, we can always choose one particular induced irreducible representation and then reproduce all other irreducible representations just by shifting the bands through the vectors $\boldsymbol{k}_{\alpha\beta}$. This shifting will ofcourse move the bands past the boundaries

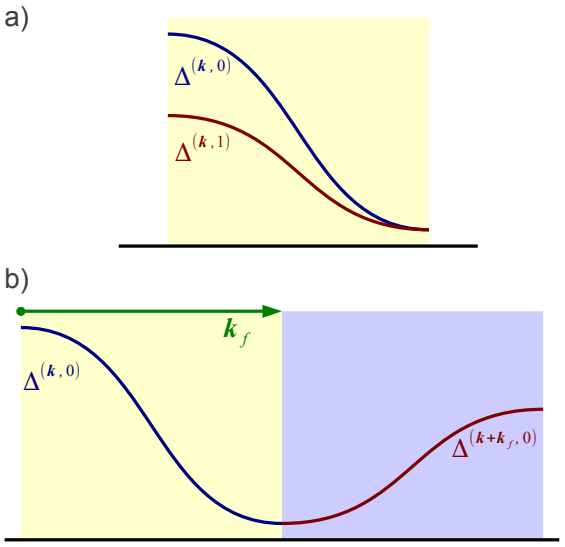

FIGURE 6.3: The unfolding of the Brillouin zone. Panel a) shows the folded bandstructure and bands belonging to the two different irreducible representations. On the panel b) one irreducible representation is reproduced from the other resulting in the unfolded bandstructure and the unfolded Brillouin zone

of the Brillouin zone and will result in the extended Brillouin zone, which will correspond to the unfolded Brillouin zone. The relations (6.15) then define the folding vectors. This is schematically shown on the figure 6.3.

The important distinction with respect to the translational unfolding with the projectors (6.8) is that the unfolding is formulated now as a projection onto the irreducible subspace which has a well understood physical meaning. The projector (6.8) is a special case of the translational unfolding where the induced unit representation is extended into the unfolded Brillouin zone. Another important distinction is that, due to the definition of the projectors (6.11), it is possible to apply unfolding to any observable, provided we know how it transforms under the action of operators from $\mathbb{S}$.

In order to arrive at (6.10) we have assumed that $\boldsymbol{k}$ is a high symmetry point for all $\hat{\mathrm{U}}_i$ so that the irreducible representations of the little co-group are one dimensional. The requirement of one dimensionality is imposed so that the irreducible representations of $\mathbb{S}$ would not contain more than one wave vector since the physical meaning of the unfolding would not be clear in that case. This imposes a limitation onto the unfolding where point group operations are employed because we have to restrict the unfolding only onto high symmetry wave vectors. This limitation is not that severe because for materials whose electronic properties are predominantly one or two dimensional, it is possible to extend the unfolding to the rest of the Brillouin zone as will be shown for the iron pnictides.

6.3.1 Unfolding of Tight-Binding Models

The unfolding formalism presented in the previous section can be employed to unfold tight-binding models. Let us assume that we have a tight-binding model associated with the Bloch basis (6.4). The matrix elements of the Hamiltonian are given by

$$[\hat{\mathrm{H}}_{\boldsymbol{k}}]_{\mu\nu} = \langle\mu|\hat{\mathrm{P}}_{\boldsymbol{k}}\hat{\mathrm{H}}\hat{\mathrm{P}}_{\boldsymbol{k}}|\nu\rangle = \langle\mu|\hat{\mathrm{H}}\hat{\mathrm{P}}_{\boldsymbol{k}}|\nu\rangle = \sum_{n=1}^{N} e^{i\boldsymbol{k}\cdot\boldsymbol{R}_n}\langle\boldsymbol{0},\mu|\hat{\mathrm{H}}|\boldsymbol{R}_n,\nu\rangle \tag{6.16}$$

where we have used the fact that $[\hat{\mathrm{P}}_{\boldsymbol{k}},\hat{\mathrm{H}}] = 0$ and that projectors are idempotent. We can now define a set of hopping energy matrices $\hat{\mathrm{t}}(\boldsymbol{R}_n)$ with matrix elements given by

$$t(\boldsymbol{R}_n)_{\mu\nu} = \langle\boldsymbol{0},\mu|\hat{\mathrm{H}}|\boldsymbol{R}_n,\nu\rangle \tag{6.17}$$

so that the tight-binding Hamiltonian (6.16) is

$$\hat{\mathrm{H}}_{\boldsymbol{k}} = \sum_{n=1}^{N} e^{i\boldsymbol{k}\cdot\boldsymbol{R}_n}\hat{\mathrm{t}}(\boldsymbol{R}_n) \tag{6.18}$$

Since we have seen that the unfolding is block diagonalizing the Hamiltonian at every $\boldsymbol{k}$, it will do the same for the hopping energy matrices, since according to (6.18) they share the same block diagonal structure of the Hamiltonian which means that we can formulate the tight-binding model of the smaller dimensionality.

The simple way to arrive at a prescription for tight-binding model unfolding is to write $\hat{\mathrm{H}}_{\boldsymbol{k}\alpha} = \hat{\mathrm{P}}_{\boldsymbol{k}\alpha}\hat{\mathrm{H}}\hat{\mathrm{P}}_{\boldsymbol{k}\alpha}$ in the form analogous to (6.18)

$$\begin{aligned}[\hat{\mathrm{H}}_{\boldsymbol{k}\alpha}]_{\mu\nu} = \langle\mu|\hat{\mathrm{H}}\hat{\mathrm{P}}_{\boldsymbol{k}\alpha}|\nu\rangle = \\ \frac{1}{F}\sum_{n=1}^{N}\sum_{i=1}^{F}\sum_{\gamma=1}^{M}\mathrm{e}^{i\alpha f_i/F}e^{i\boldsymbol{k}\cdot(\boldsymbol{R}_n+\boldsymbol{\tau}_i)}\langle\boldsymbol{0},\mu|\hat{\mathrm{H}}|\boldsymbol{R}_n,\gamma\rangle W_{\gamma\nu}(\hat{\mathrm{C}}_i) = \\ \frac{1}{F}\sum_{n=1}^{N}\sum_{i=1}^{F}\sum_{\gamma=1}^{M}\mathrm{e}^{i\alpha f_i/F}e^{i\boldsymbol{k}\cdot(\boldsymbol{R}_n+\boldsymbol{\tau}_i)}t_{\mu\gamma}(\boldsymbol{R}_n)W_{\gamma\nu}(\hat{\mathrm{C}}_i)\end{aligned} \tag{6.19}$$

On the other hand, for the unfolded tight-binding model, the expression analogous to (6.18) is

$$\hat{\mathrm{H}}_{\boldsymbol{k}\alpha} = \sum_{n=1}^{N}\sum_{i=1}^{F} e^{i\boldsymbol{k}\cdot(\boldsymbol{R}_n+\boldsymbol{\tau}_i)}\hat{\mathrm{t}}_{\alpha}(\boldsymbol{R}_n+\boldsymbol{\tau}_i)$$

By comparing to (6.19) we can read off the relation between $\hat{\mathrm{t}}(\boldsymbol{R}_n)$ and $\hat{\mathrm{t}}_\alpha(\boldsymbol{R}_n + \boldsymbol{\tau}_i)$

$$\hat{\mathrm{t}}_\alpha(\boldsymbol{R}_n + \boldsymbol{\tau}_i) = \frac{1}{F} \mathrm{e}^{i\alpha f_i/F} \hat{\mathrm{t}}(\boldsymbol{R}_n) \hat{\mathrm{W}}(\hat{\mathrm{C}}_i) \tag{6.20}$$

The exponential prefactor is a problem since it can cause the hopping energies to be complex in the unfolded tight binding model. However, this prefactor is the only thing differentiating irreducible components of the unfolded hopping energy matrices and it amounts to an overall $\boldsymbol{k}$-independent unitary transformation of the Hamiltonian. Furthermore, in the unfolded picture, we extend a single irreducible representation past the Brillouin zone boundaries, so that in the tight-binding model picture, we expect to have a single set of hopping energies, independent of the irreducible representation, which manifestly does not hold here because the exponential prefactor depends on α. Because of this, we can drop the exponential and define the irreducible representation-independent unfolded hopping energy matrices as

$$\hat{\mathrm{t}}(\boldsymbol{R}_n + \boldsymbol{\tau}_i) = \frac{1}{F} \hat{\mathrm{t}}(\boldsymbol{R}_n) \hat{\mathrm{W}}(\hat{\mathrm{C}}_i) \tag{6.21}$$

where the indices μ and ν of the hopping energy matrix now run only over a single block $\hat{\mathrm{H}}_{\boldsymbol{k}\alpha}$ in the block-diagonalized Hamiltonian.

6.4 Applications of The Bands Structure Unfolding

The iron pnictide family of the materials provides an excellent proving grounds for the unfolding method presented here. All iron pnictides are built up from the layers consisting of the iron atoms tetrahedrally coordinated by the pnictogen atoms as shown on Fig 6.4 (a). Different families of the iron pnictide materials are differentiated by the stacking sequence of the iron pnictogen layers, as well as by the content of the spacer layers. For most of the iron pnictide families, minimal translationally invariant unit cell consists of two iron and two pnictogen atoms. This unit cell can further be reduced by considering the glide-mirror operations, which combine the translations between the nearest-neighbor iron atoms with reflections in the xy-plane, thus mapping two translationally inequivalent irons and pnictogens into each other.

For the first example, we will consider a simple case of the translational unfolding, where the translation group $\mathbb{T}$ is expanded by fractional translations $\hat{\mathrm{C}}_i = [1|\boldsymbol{\tau}_i]$. For example, let us consider the supercell of the tetragonal FeSe Fig 6.4 (a). The suprecell consists

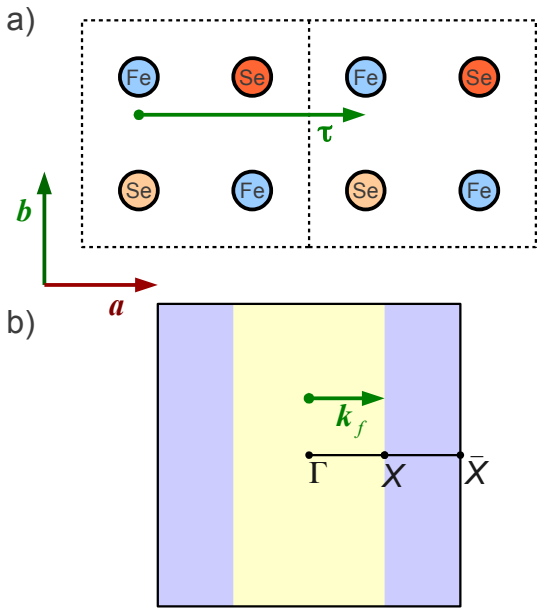

FIGURE 6.4: Unit cel l a nd Brillo uin zo ne of the tet ragon al FeSe , dou bled along the $\boldsymbol{a}$-axis. (a) Supercell consisting of two unit cells of tetragonal FeSe. Fractional translation $\boldsymbol{\tau}$ is shown in green color. The iron atoms lie in the same plane, parallel to the plane of the drawing, while the lighter colored selenium atoms are vertically displaced above the plane, and the darker colored ones are below. (b) $k_z = 0$ plane of the Brillouin zone corresponding to the single unit cell of FeSe. Yellow filling marks the Brillouin zone corresponding to the supercell. The folding vector $\boldsymbol{k}_f$ is shown in green color.

of the unit cell doubled along the $\boldsymbol{a}$ axis of FeSe. The bandstructure along the path $\Gamma - X$ shown in Fig 6.4 (b), corresponding to the FeSe supercell is shown on Fig 6.5 (a). To unfold the bands, we employ an additional symmetry the supercell has, on top of the translational symmetry $\mathbb{T}$, and that is the fractional translation $\boldsymbol{\tau} = \boldsymbol{a}$. With this, the factor group $\mathbb{S} : \mathbb{T}$ is isomorphic to the cyclic group of order two, with the generator $[1|\boldsymbol{\tau}]$. With this, from every irreducible representation of $\mathbb{T}$, two irreducible representations with $\alpha = 0$ and $\alpha = 1$ are induced (for details see Appendix B.1).

The resulting projections of bands onto the irreducible representations are shown in Fig 6.5 (b) and (c), while the unfolded picture, where the irreducible representation $\Delta^{(\boldsymbol{k},0)}$ is extended outside the supercell Brillouin zone is shown in Fig 6.5 (d). Evidently $\Delta^{(\boldsymbol{k}+\boldsymbol{k}_f,0)} = \Delta^{(\boldsymbol{k},1)}$, with $\boldsymbol{k}_f = (\pi/a, 0, 0)$.

The unfolding shown on (Fig) is perfect, because the fractional translation $[1|\boldsymbol{\tau}]$ is an exact symmetry of the supercell and every band will belong to only one of the irreducible representations of $\mathbb{S}$. In the realistic case, where the operations $\hat{\mathrm{C}}_i$ are only approximate symmetries, the bands will have nonzero projections onto multiple irreducible representations, although usually, only one of the irreducible representations will be dominantly

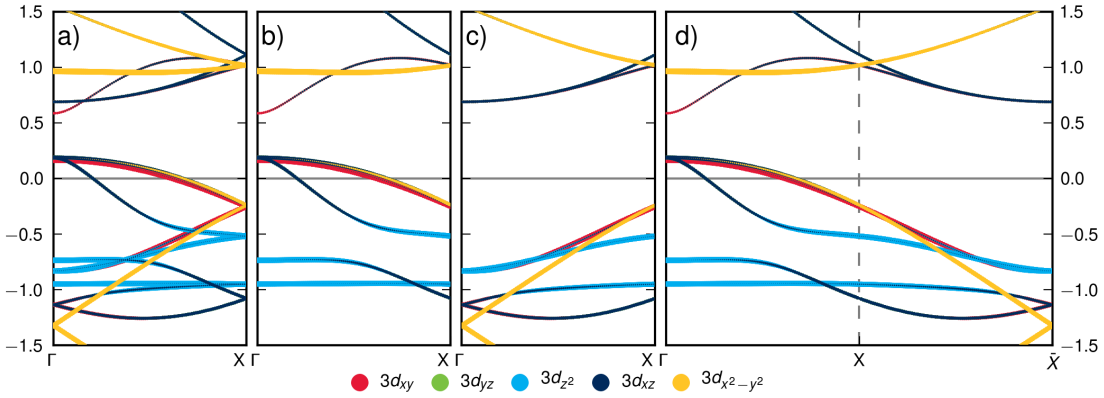

FIGURE 6.5: Unfolding of the tetragonal FeSe doubled along the $\boldsymbol{a}$-axis. (a) The folded bandstructure. (b) Projection of bands onto $\Delta^{(\boldsymbol{k},0)}$. (c) Projection of bands onto $\Delta^{(\boldsymbol{k},1)}$. (d) Unfolded picture. Irreducible representation $\Delta^{(,0)}$ is extended past the boundaries of the Brillouin zone by the folding vector $\boldsymbol{k}_f = (\pi/a, 0, 0)$.

present in every band.

Such situation occurs, for example, when studying the doped compounds. We have chosen to study the phosphorus doped $CaFe_2As_2$. We have already seen in chapter 5 that when the pressure is applied, $CaFe_2As_2$ undergoes a magnetostructural phase transition from the magnetically ordered orthorhombic phase, to the non-magnetic, collapsed tetragonal phase. It is also possible to induce the orthorhombic to collapsed tetragonal phase transition in $CaFe_2As_2$ by applying the chemical pressure. For, example, substitutional doping of phosphorus into the arsenic sites, causes $CaFe_2As_2$ to enter the collapsed tetragonal phase at the doping level of around 5%[96]. To fully understand how chemical pressure is related to the application of physical pressure, we have performed a sequence of full structural relaxations of P-doped $CaFe_2As_2$. To achieve varying levels of doping, we have used supercells of different size.

We have found that ab-initio calculations predict that P-doped $CaFe_2As_2$ undergoes orthorhombic to collapsed tetragonal phase transition for the doping level between 9.375% and 12.5% in accordance with the experiment. In order to analyze the electronic structure in the collapsed tetragonal phase of the P-doped $CaFe_2As_2$, we have to perform the unfolding of the bandstructure.

The relaxed $Ca(FeAs_{1-x}P_x)_2$ has an orthorhombic unit cell, where the phosphorus atom is breaking the translational symmetry as shown on Fig 6.6. The unit cell of $Ca(FeAs_{1-x}P_x)_2$ is a supercell consisting of the four primitive unit cells of $CaFe_2As_2$. This unit cell contains a total of eight iron atoms. The corresponding fractional translations are $\boldsymbol{\tau}_1 = (\boldsymbol{a} + \boldsymbol{b})/2$, $\boldsymbol{\tau}_2 = (\boldsymbol{a} + \boldsymbol{c})/2$ and $\boldsymbol{\tau}_3 = \boldsymbol{\tau}_1 + \boldsymbol{\tau}_2$, where $\boldsymbol{a}$, $\boldsymbol{b}$ and $\boldsymbol{c}$ are the unit vectors of the supercell, as shown on Fig 6.6. These fractional translations map the two translationally inequivalent iron atoms to the eight iron atoms of the supercell. .

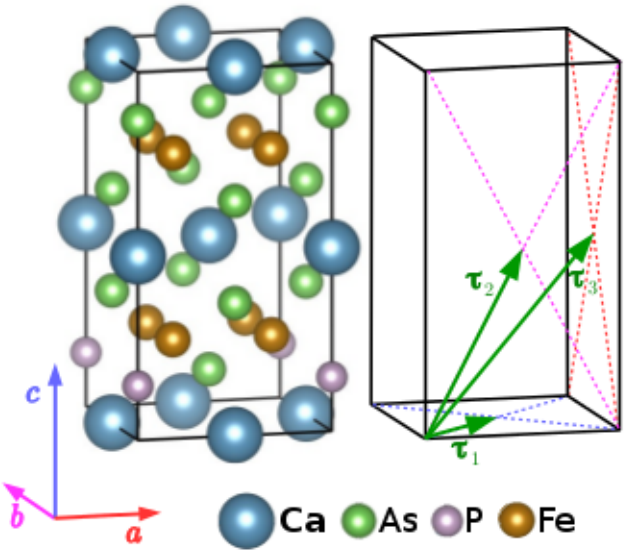

FIGURE 6.6: The unit cell of $Ca(FeAs_{1-x}P_x)_2$. The fractional translations $\boldsymbol{\tau}_i$ are shown in green color.

The corresponding bandstructure is shown on Fig 6.7 (a). The bandstructure is calculated along the path given by $(0,0,0) - (2\pi/a,0,0) - (2\pi/a,2\pi/a,0) - (0,0,0) - (0,0,2\pi/c)$. Four irreducible representations can be induced (for details see Appendix B.2). We will select the irreducible representation $\Delta^{(\boldsymbol{k},0)}$ and extend it to the unfolded Brillouin zone. The resulting unfolded bandstructure, obtained by extending the irreducible representation $\Delta^{(\boldsymbol{k},0)}$ is shown in Fig 6.7 (b). Despite the fact that the fractional translations $\boldsymbol{\tau}_i$ are not the exact symmetries of $Ca(FeAs_{1-x}P_x)_2$, the band projections onto different irreducible representations are still mostly orthogonal, having relatively clean unfolded bands as a result. This allows us to clearly see disappearance of the hole pockets centered around Γ, since the set of three hole t_{2g} bands is pushed bellow the Fermi level by around 0.2eV. Comparison of the unfolded bands to the bandstructure of the collapsed tetragonal phase of $CaFe_2As_2$ under pressure[29] confirms that phosphorus doping and application of the hydrostatic pressure affects the structural and electronic properties of $CaFe_2As_2$ in a remarkably similar way.

As a final example, we will demonstrate how inclusion of the point group operations can be used to unfold the bandstructure past the limit imposed by the translational symmetry. Simultaneously, we will showcase the use of (6.20) and (6.21) for the unfolding of the tight-binding models.

We have used the projective Wannier funtions, as implemented in the FPLO code[12], to obtain the 16 band tight-binding model of the FeSe structure obtained in the ab-initio simulation of the hydrostatic pressure application of 10GPa. The tight-binding model consists of five $3d$ orbitals per iron site, and three $4p$ orbitals per selenium site.

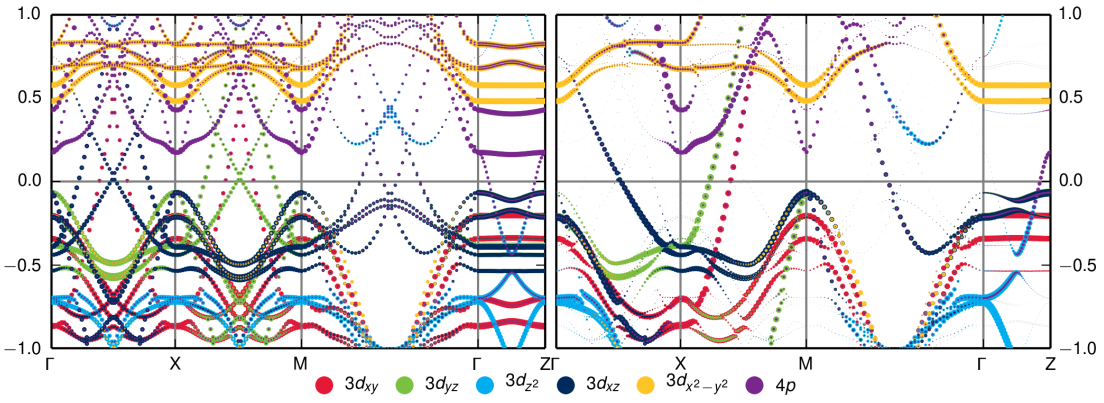

FIGURE 6.7: Unfolding of $Ca(FeAs_{1-x}P_x)_2$ bandstructure. (a) Bandstructure o f t he $Ca(FeAs_{1-x}P_x)_2$ supercell. (b) The unfolded bandstructure obtained from $\Delta^{(\boldsymbol{k},0)}$.

As was already mentioned, the two translationally nonequivalent iron sites can be mapped onto each other with the help of the glide mirror operations $\hat{C}_i = [\hat{\sigma}_z|\boldsymbol{\tau}_i]$ with $i = 1, 2$. The fractional translations $\boldsymbol{\tau}_i$ connect the nearest neighbor iron atoms, as shown on Fig 6.4 (a), while $\hat{\sigma}_z$ is a reflection in the xy-plane. To unfold, we can choose one of $\hat{C}_i$ and then induce the irreducible representations of $\mathbb{S} = \mathbb{T} \cup \mathbb{T}\hat{C}_i$. In accordance with [79], we call $\mathbb{S}$ the glide-mirror group. Since the factor group is of index two, two one-dimensional irreducible representations will be induced in the $k_z = 0$ plane of the Brillouin zone (for details see Appendix B.3). Because the electronic dispersion in the FeSe is much weaker along the $\boldsymbol{k}_z$ axis, we can expect that irreducible representations induced in the $k_z = 0$ plane will give good unfolding across the rest of the Brillouin zone.

In these two irreducible representations, the glide mirror operation will have the same representation as did the fractional translation in the example of doubled unit cell of FeSe. However, what differentiates the case of the glide-mirror unfolding, from the purely translational unfolding, is the orbitally selective action of the matrices $\hat{W}(\hat{C}_i)$ in (6.11). Namely, in the case of translational unfolding, matrices $\hat{W}(\hat{C}_i)$ act the same on all orbitals, while in the case of glide-mirror unfolding, they act differently, depending on whether the orbitals are symmetric or antisymmetric with respect to the reflections in the xy-plane. For example, $3d_{z^2}$ orbital will stay invariant, while $3d_{xz}$ will pick up a minus sign under the action of $\hat{\sigma}_z$.

We have used (6.20) to create the two sets of hopping energies, corresponding to two induced irreducible representations. These two sets correspond to the same 8 band tight-binding model, up to the unitary transformation. The bandstructure calculated from the 16 band and two 8 band tight-binding models along the path in the $k_z = 0$ plane of the Brillouin zone is shown on Fig 6.8 (a). The corresponding Fermi surface

slice in the $k_z = 0$ plane is shown in Fig 6.8 (c). It is evident that the unfolding to the 8 band model is perfect in the $k_z = 0$ plane. Since the $k_z = \pm\pi/c$ planes are also the high-symmetry planes for the reflections in the xy-plane, the unfolding will be perfect there too. We can thus expect the largest deviations from the perfect unfolding around the $k_z = \pm\pi/2c$ plane. This can be seen in the bandstructure shown in Fig 6.8 (b), taken along the path shown in Fig 6.8 (a) shifted by $(0, 0, \pi/2c)$. The deviations of the unfolded bands are evident. However, the deviations of the top ten bands, which are the bands dominated by the $3d$ orbital character, are much smaller than in the bands dominated by the $4p$ orbital character. This is a consequence of the crystal structure, since the iron atoms are stationary under the action of $\hat{\sigma}_z$, while the selenium atoms are not. Owing to this property, Fermi surface can be unfolded almost exactly across the entire Brillouin zone. The Fermi surface slice in the $k_z = \pi/2c$ is shown in Fig 6.8 (d), while the vertical slice in the $k_y = 0$ plane is shown in Fig 6.8 (e). It is remarkable that the full three dimensional structure of the innermost Fermi surface pocket, centered at Γ, is retained with high accuracy in the unfolded model, despite the fact that the basis for the unfolding is purely two-dimensional. Similar behavior is observed in other memebers of the iron-pnictide family.

This result has an important implication for the one-iron vs. two-iron discussion in the iron pnictides[93]. When the unfolding is considered as a projection onto the irreducible subspace of the glide-mirror group, we come to the conclusion opposite of [93]. As long as we are interested in a range of energies within 1eV from the Fermi surface, a one-iron tight-binding model can be used without significantly impacting the overall accuracy of the calculation.

In addition, we arrive to a different conclusion from [93] about the reason why the neutron scattering intensities seem to indicate the picture consistent with the one-iron picture[97][98]. Again, this can naturally be interpreted as a consequence of the fact that transitions between the states belonging to different irreducible subspaces are forbidden as long as the interaction Hamiltonian has the approximate glide mirror symmetry.

6.5 Summary

In summary, we have demonstrated that more rigorous group theoretic treatment of bandstructure unfolding shows that it can be understood as projection onto induced irreducible representations of the supergroup of the original translation group. The unfolded Brillouin zone arises as a consequence of the fact that different induced irreducible representations become identical when shifted by an appropriate vector in the

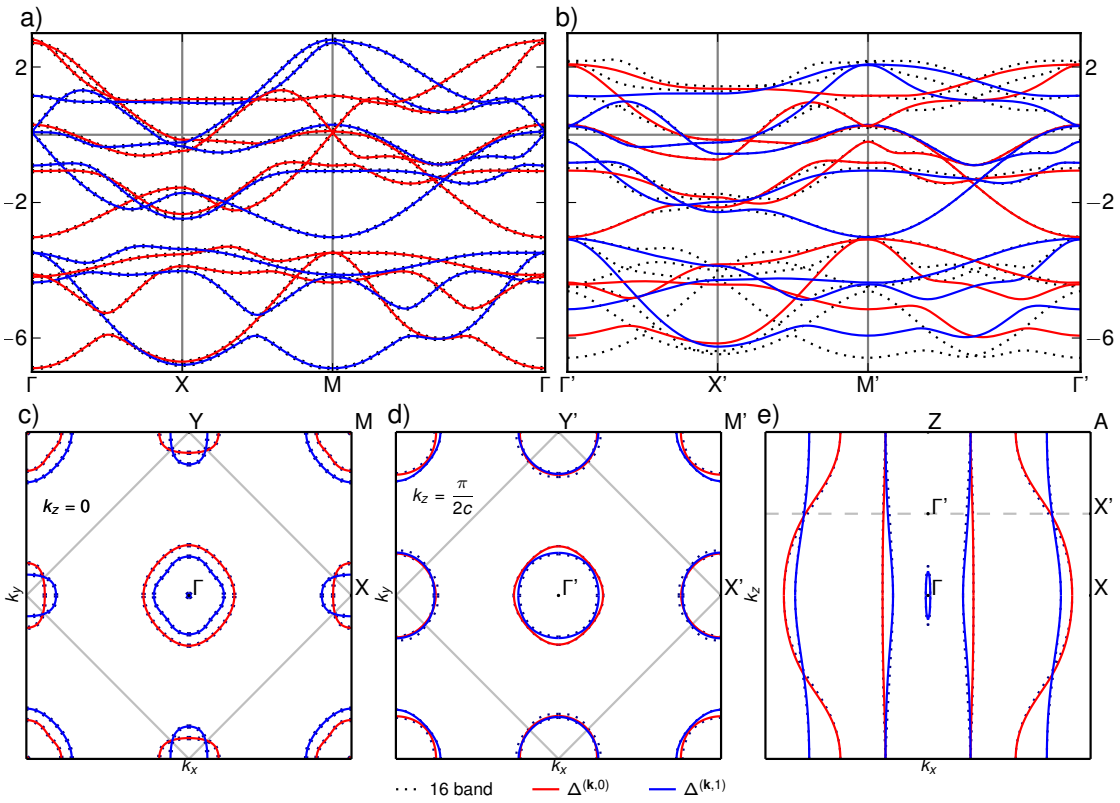

FIGURE 6.8: Unfolding of the 16 band tight-binding model of FeSe with the help of glide-mirror operations. (a) Bandstructure along the path in the $k_z = 0$ plane of the one iron equivalent Brillouin zone. (b) Bandstructure along the path parallel to the path shown in (a), but shifted along the $\boldsymbol{k}_z$-axis by $\pi/2c$. (c) Fermi surface cut at $k_z = 0$ plane of the one iron equivalent Brillouin zone of FeSe. The solid grey line shows the boundary of the two iron Brillouin zone. (d) Fermi surface cut at $k_z = \pi/2c$ plane of the one iron equivalent Brillouin zone of FeSe. (e) Fermi surface cut at $k_y = 0$ plane of the one iron equivalent Brillouin zone of FeSe. The dashed grey line shows the location of $k_z = \pi/2c$.

Brillouin zone. Due to the projective definition, the unfolding procedure can be generalized to arbitrary quantities in the reciprocal space. Also, the unfolding artefacts in the cases where the unfolding is inexact, arise because bands have nonzero projections onto multiple irreducible representations.

When point group operations are used, the unfolding is exact only in the high-symmetry k-points of the Brillouin zone. It is nonetheless possible to extend the unfolding onto the entire Brillouin zone as long as the bandstructure is dominantly dispersive only along the corresponding high-symmetry lines or planes in the Brillouin zone. By making sure this constraint is satisfied, it is possible to formulate tight-binding models of reduced dimensionality without the loss of accuracy.

On the example of FeSe, we have shown how an 8 band tight-binding model can be constructed by unfolding the 16-band tight-binding model with the help of glide-mirror

operations. The resulting unfolded model produces the almost exactly unfolded Fermi surface. Similar results in other iron-pnictides confirm that one-iron tight-binding models can reliably be used in the vicinity of the Fermi level.

Chapter 7

Contributed Work

Besides the main topic of this thesis, the iron pnictide materials, other important calculations were performed in order to investigate the giant volume collapse observed in MnS_2[99] as well as the nature of the electronic properties of the alkaline doped picene[100] which has been suggested to superconduct.

A short overview will be given of the basic properties of MnS_2, followed by the overview of the results of ab-initio simulations of the hydrostatic pressure application on MnS_2, which represent the author's original contribution to ref. [99]. These results will be put in the overall context of the research presented in ref. [99].

Finally, we will outline the properties of alkali doped picene and the motivation for the research presented in ref. [100]. The author's original contribution consists of prediction of structures of picene doped with various alkaline atoms.

7.1 Giant Volume Collapse in MnS_2

The MnS_2 has long been known to undergo a structural phase transition under application of pressure, where the remarkable volume collapse of around 15% has been observed at around 11 GPa[101, 102]. Such volume collapses in the transition metals are usually driven by the transitions in the spin state of the system, where the crystal field splitting is competing with the Hund's rule and the Coulomb interaction. This is expected to be the case for MnS_2, since it possesses the pyrite structure (spacegroup $Pa\bar{3}$) in which every manganese atom is octahedrally coordinated by six sulfur atoms.

As a result of the octahedral symmetry, the energy levels corresponding to the $3d$ atomic orbitals of iron atoms are split into a set of three degenerate t_{2g} and two degenerate e_g

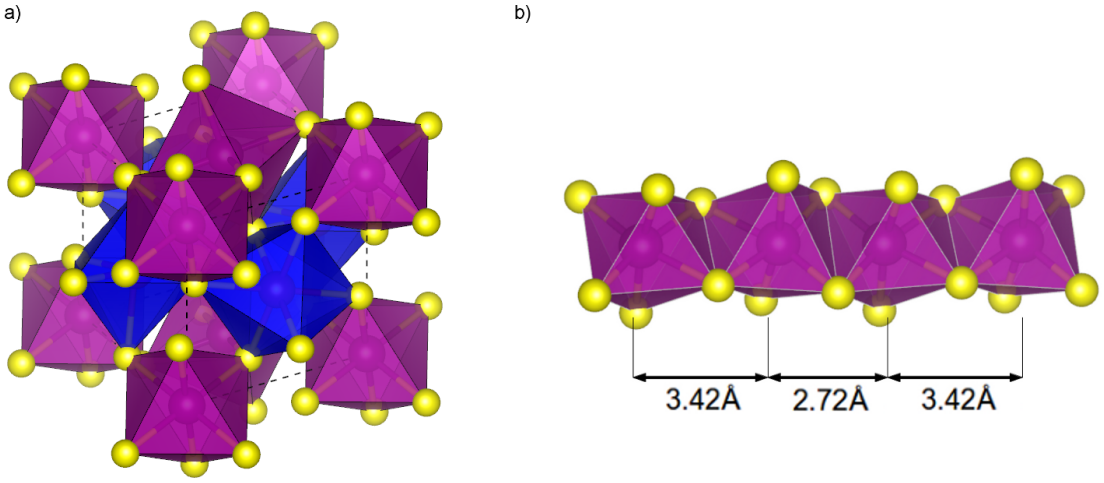

FIGURE 7.1: Structures of high pressure and low pressure phases of MnS_2. Panel (a) shows the ambient pressure pyrite structure of MnS_2 characterized by the corner sharing octahedra. Panel (b) shows a chain of edge sharing octahedra in the high-pressure arsenopyrite structure of MnS_2.

levels so that at ambient pressure MnS_2, iron atoms have a spin of 5/2. This is the high-spin $t_{2g}^3 e_g^2$ state which is stabilized by the Hund's rule coupling.

When hydrostatic pressure is applied, the sulfur atoms approach the iron atoms, increasing the crystal field splitting, which makes the low-spin $t_{2g}^5 e_g^0$ more favorable. In the low-spin state, iron atoms have spin of 1/2.

This high-spin to low-spin transition has been conjectured to be behind the 15% volume collapse at 11 GPa[101]. However, subsequent measurements have identified presence of a disordered phase at high-pressure.

Motivated by this finding, the experimental group of S. Kimber and collaborators has applied pressure to MnS_2 using gas-loaded diamond anvil cells and x-ray diffraction was used to determine the resulting crystal structures [99]. The pyrite structure remains stable, with no reduction in crystallinity until the pressure of 11.7 GPa, which is confirmed by the sharp peaks in the x-ray diffraction pattern. When pressure is increased to 11.85 GPa, the well defined peaks in the x-ray diffraction pattern are replaced by a series of broad maxima, making structure determination impossible.

Due to the poor quality of the x-ray diffraction data, the candidate structure was determined by employing the ab-initio simulations. A candidate structure was obtained by K. Muthukumar from around 2800 structures generated by Universal Structure Predictor: Evolutionary Xtallography (USPEX)[103, 104] and locally optimized by VASP.

The resulting structure was a so called arsenopyrite structure (spacegroup $P2_1/c$) which was successfully matched to the x-ray diffraction pattern obtained from the 20 GPa

structure of MnS_2, recrystallized by the application of the in-situ laser heating. While the pyrite structure is characterized by the MnS_4 octahedra sharing a single corner with the nearest neighbor octahedron, the arsenopyrite structures features chains of edge sharing octahedra, as shown in figure 7.1.

This indicates that there are two competing metastable phases of MnS_2. To determine the regions of stability of both phases, ab-initio pressure simulations were performed with VASP package. Both the pyrite and arsenopyrite crystal structures of MnS_2 were subjected to pressures in the 0-20 GPa range. Figure 7.2 shows the results. Panel (a) shows volume of the experimentally determined unit cell. The volume collapse of 22% is evident. From panel (b) which shows enthalpy calculated by the ab-initio pressure simulations we can see that the pyrite phase is the stable phase in the 0-10 GPa range while arsenopyrite phase becomes more stable in the 10-20 GPa range, putting the transition pressure at 10 GPa. Panels (c) and (d) show the excellent agreement of ab-initio and experimental Mn-Mn and Mn-S distances. To further validate the stability of the arsenopyrite phase phonon dispersion was calculated for the 20 GPa structure using Phonopy package [105]. No soft modes could be observed along the path spanning the high-symmetry points of the Brillouin zone.

In ab-initio simulations, type III antiferromagnetic order [106] was imposed. Magnetic moments of the manganese atoms are around 4 μ_B in the pyrite phase, while in the arsenopyrite phase they assume the value of around 1 μ_B, confirming the high-spin to low-spin transition.

Additional important feature of the arsenopyrite phase is dimerization of chains of the edge-sharing octahedra (panel (b) in fig. 7.1), where the shorter dimer is hosting a spin singlet. This can clearly be observed on fig. 7.2 (c), where two distinct Mn-Mn bond lengths appear in the arsenopyrite phase. The formation of dimerized chains opens up the possibility to discuss this phase transition in the framework of a Peierls-type distortion. However, this is ruled out by the fact that dimers in MnS_2 are better described as a 3D network, which is confirmed by the tight-binding fit yielding intradimer and interdimer hopping parameters of 0.37 eV and 0.15 eV respectively. This is consistent with the physics of a valence bond solid which explains why such a dramatic change occurs at the phase transition. In addition, formation of Mn-Mn dimers provides enough stabilization energy to offset the penalty coming from the huge increase in density.

These findings imply that a qualitatively new mechanism is responsible for the volume collapse in MnS_2. This is important result for the investigations of the Earth's mantle where minerals containing the magnetic metals might undergo volume collapse under pressure. Although Mn_2 is geologically not abundant, the volume collapse mechanism described here is applicable to other isoelectronic magnetic cations such as Fe^{3+}.

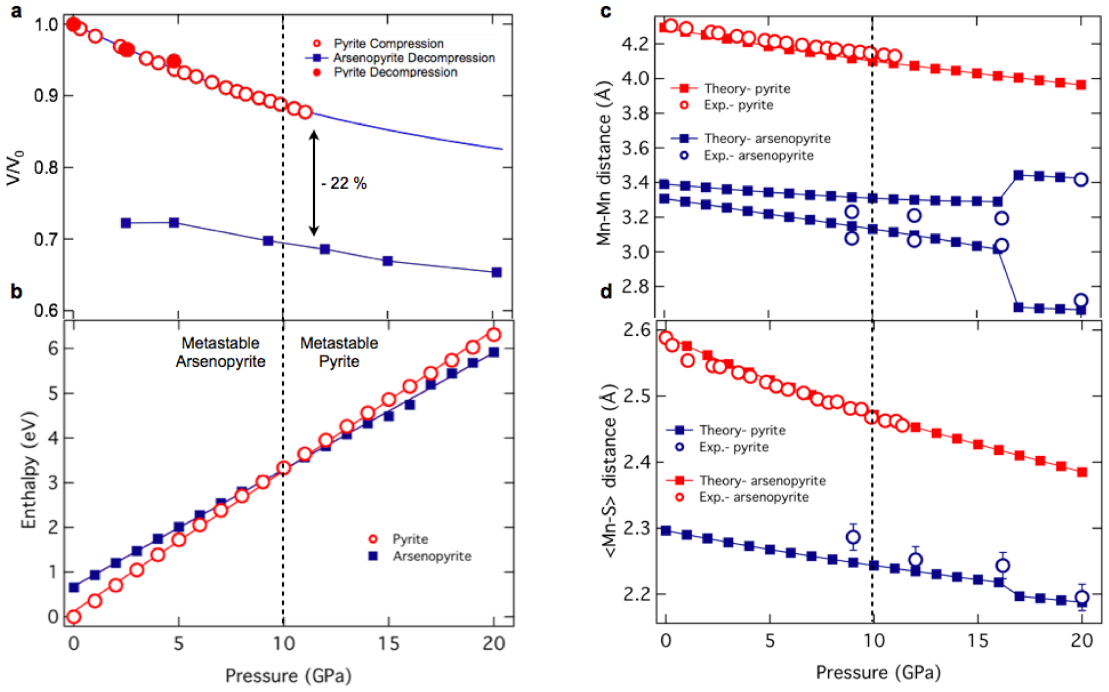

FIGURE 7.2: Structural parameters of MnS_2 under hydrostatic pressure. (a) Pressure evolution of the exprimentally determined unit cell volume (symbols) overlayed on top of the volume obtained by fitting the Birch-Murnaghan equation of state to the experimtal data (lines) (b) Ab-initio enthalpy in the pyrite and arsenopyrite phase. (c) Mn-Mn distance comparison of the ab-initio and experimental structures in pyrite and arsenopyrite phase. (d) Mn-S distance comparison of the ab-initio and experimental structures in pyrite and arsenopyrite phase.

7.2 Alkaline Doped Picene

Since the observation of the superconductivity in the potassium doped picene [107, 108] the nature of the electronic structure of potassium doped picene has remained an open issue. The calculations based on the density functional theory suggest that the intercalation of a potassium atom into the picene would result in the metallic state, while the different photoemission measurements seem to indicate contradictory findings. The inability to observe the metallic state predicted by the density functional theory in some photoemission measurements raises the question of the role of the electronic correlations, making the case of potassium doped picene important in the more general discussion of the role of the electronic correlations versus electron-phonon interaction in the organic superconductors.

For this reason, joint theoretical and photoemission study has been performed [100]. The photoemission study has examined the potassium doped picene films for doping levels of one, two and three potassium atoms per picene molecule. The photoemission study was unable to observe metallic state for any of the doping levels.

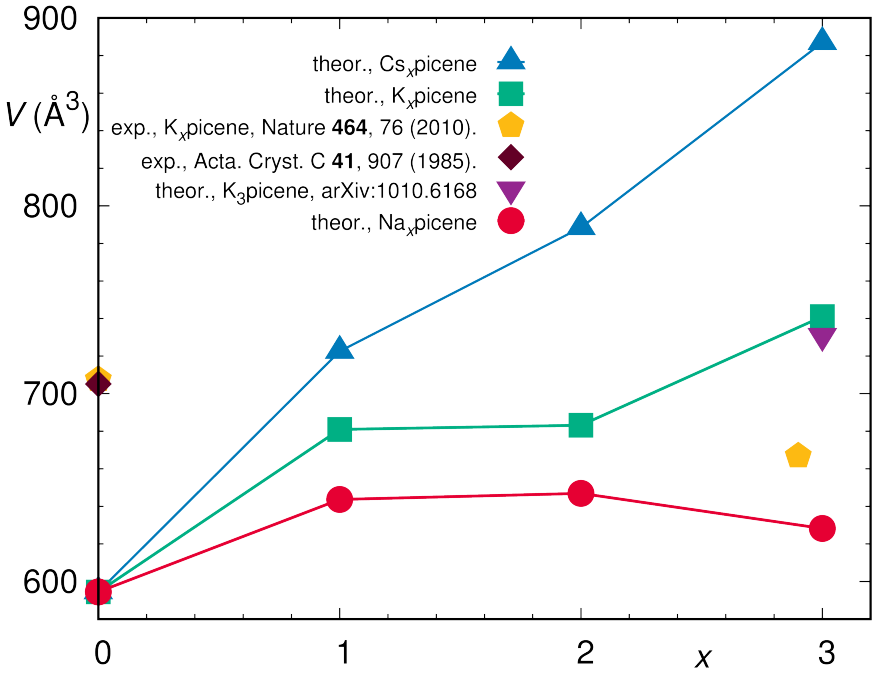

FIGURE 7.3: Unit cell volume of A_x picene, with A=Na, K, Cs and $x = 0, 1, 2, 3$.

To clarify the experimental findings further it was necessary to perform the ab-initio calculations. To do so, the structures parameters of potassium doped picene had to be determined, since no structural parameters were experimentally known for doped cases, with the exception of unit cell volume of K_3 picene [107] (it should be noted here that doping concentrations are only nominal since structure characterization of potassium doped picene is very hard to accomplish). To check for consistency, in addition to potassium, cesium and sodium were also intercalated between the picene molecules at concentrations of one, two and three atoms per picene molecule. The resulting unit cell volumes are shown in fig. 7.3 and the evolution of equilibrium K_x picene structure with increase of x is shown in fig. 7.4.

It is evident that unit cell volumes increase with the size of the dopant atom. Interesting feature is that unit cell volume remains constant when dopant concentration is increased from one atom per picene molecule to two atoms per picene molecule in cases of sodium and potassium and that it drops when going from Na_2 picene to Na_3 picene. This indicates that provision of additional electrons in the intercalation space increases picene-picene intermolecular bonding but is offset by the increase of the dopant atom size.

For the pristine picene, there is a large discrepancy between the unit cell volume predicted by our calculation and the experimentally determined value [109] and the theoretical study [110]. The probable reason is that PAW basis is ill suited to describe large amounts of empty space between the picene molecules. We expect however that this

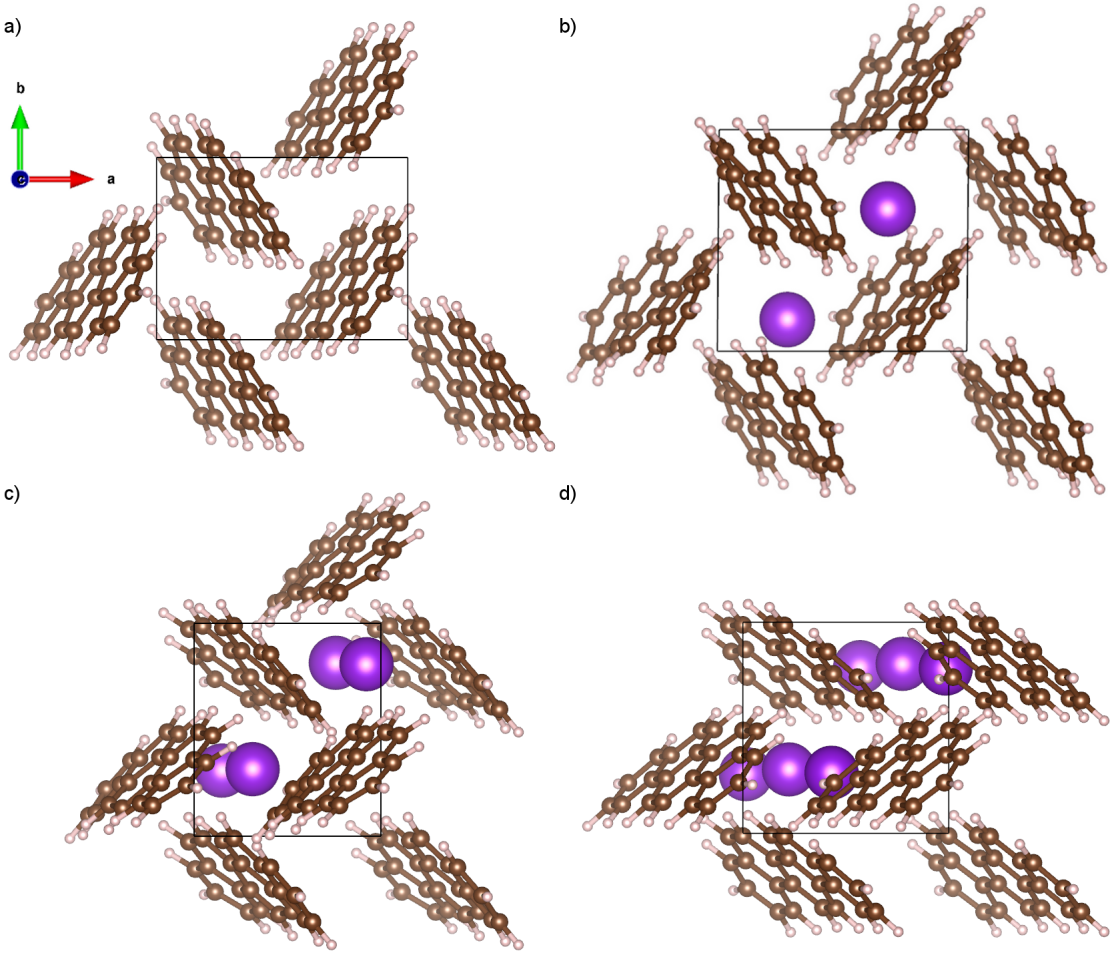

FIGURE 7.4: Crystal structures of K_x picene for $x = 0, 1, 2, 3$ in panels (a), (b), (c) and (d) respectively. View is along the **c** unit cell vector.

deficiency will be less prominent when alkaline atoms are intercalated which seems to be corroborated for the case of K_3 picene.

The density functional theory predicts the ab-initio structures of K_x picene to be metallic for odd x and seminconducting for even x. Since density functional theory cannot account for electronic correlations, it was necessary to include them by performing a calculation within the framework of the dynamical mean field theory, conducted by H. Lee. When electronic correlations are taken into account, band gap opens in the spectral function for all ab-initio K_x picene structures, confirming the experimental finding.

7.3 Summary

This section has given a short overview of calculations performed by the author which have contributed to studies which were not the main focus of this thesis.

In case of the giant volume collapse in MnS_2, the unknown high-pressure arsenopyrite structure was successfully determined. The ab-initio simulations of pressure application have shown that volume collapse of 22% is a consequence of the high-spin to low-spin transition, stabilized by the formation of the valence bond solid in the high pressure phase. This is a qualitatively new mechanism with the important implications for the physics of the Earth's mantle.

In the case of potassium doped picene, the experimentally unavailable crystal structures have been obtained through the ab-initio structure optimization. The dynamical mean field theory calculation has been able to support the photoemission findings which were important for the ongoing controversy about the status of the superconductivity in the potassium doped picene.

Chapter 8

Summary and Outlook

The structural and the electronic properties of iron pnictides can be tuned to a great effect by the application of pressure. The outcome is highly dependent on the exact nature of pressure conditions. In order to be able to study the effects of nonhydrostatic pressure we have developed an original method in chapter 4 which leverages the metadynamics of the Fast Inertial Relaxation Engine algorithm by expanding the space of atomic degrees of freedom with crystal lattice degrees of freedom.

In chapter 5 we have applied this method to study how hydrostatic and uniaxial pressure affects the structural and electronic properties of $BaFe_2As_2$ and $CaFe_2As_2$. We have found that application of hydrostatic and **c**-axis uniaxial pressure result in the suppression of magnetic ordering both in $BaFe_2As_2$ and $CaFe_2As_2$. While $CaFe_2As_2$ undergoes transition to the collapsed tetragonal phase upon suppression of the magnetic order, $BaFe_2As_2$ first undergoes additional transition to the intermediate tetragonal phase. Our findings are inconsistent with the reports of the intermediate tetragonal phase in $CaFe_2As_2$. The transition from orthorhombic to the collapsed tetragonal phase is followed by a change in the Fermi surface topology whereby the hole pocket cylinders centered around the Γ-point disappear suppressing the possible channels for Cooper pair scattering. These findings, along with the estimates of the bulk modulus and elastic constants are in a good agreement with the experimental findings proving that our method of uniaxial pressure simulation is reliable and that it can be applied in the future studies.

We have also found that in-plane application of both tensile and compressive stress is not sufficient to suppress the magnetic moments and cause the transition into the tetragonal phase. Instead, what is observed is abrupt change in orthorhombicity, whereby the ferromagnetic and antiferromagnetic directions are interchanged. The Ginzburg-Landau analysis has revealed the interplay between the intrinsic magneto-elastic coupling and stress as a direct cause of such behavior. We also find that $BaFe_2As_2$ and $CaFe_2As_2$

have qualitatively very different response to the applied pressure. While the $BaFe_2As_2$ shows the greatest rate of suppression of the magnetic moment for in-plane application of stress, the $CaFe_2As_2$ shows the greatest rate of suppression for the pressure applied along the **c**-axis which is also a direction of structural instability, explaining why the phase transition is much more abrupt in $CaFe_2As_2$ than in $BaFe_2As_2$.

Important problem facing the ab-initio structure prediction in iron-pnictides is the overestimation of the critical pressure caused by the overestimation of the magnetic moments in the Generalized Gradient Approximation. Thus, for the future study, it would be interesting to attempt to use the exchange field downscaling to reduce the magnetic moments and obtain more accurate results.

Doping, or chemical pressure is another way to tune the structural and electron properties of iron-pnictides and is largely unexplored by the ab-initio simulations. Especially interesting question to study is the role of vacancies in iron-selenide compounds such as FeSe and KFe_2Se_2 as well as behavior of uniaxially strained FeSe on $SrTiO_3$ substrates where the largest T_c has been reported.

One problem for the study of the electronic properties of these structures is that in doped structures, structures with vacancies or structures on substrates, the original translational symmetry of the iron-pnictogen(chalcogen) layer is broken, necessitating the use of large supercells. This results in folding of the bandstructure, which makes analysis of the electronic structure difficult.

In chapter we have developed a solution to this problem by applying group theoretical considerations. Careful application of the group theory has allowed us to interpret the unfolding of bandstructure as projection onto the irreducible subspaces of a spacegroup. With this, a unified framework was obtained whereby point group operations can be included into the unfolding and the unit cell effectively reduced under certain conditions, which is important feature for model calculations. Another benefit of our group theoretical approach to unfolding is that the magnetic symmetries can be treated on equal footing with the geometric symmetries, represented by Shubnikov groups, allowing exact unfolding of the spin-polarized bandstructures, which is the goal for a future study.

Appendix A

Irreducible Representations of Space Groups

Examination of folding of bandstructures requires construction of the irreducible representations of space groups. Since construction of irreducible representations of space groups can be a very involved issue on its own, this section will give a brief overview of the required group theory concepts, followed by the application to the induction of irreducible representations of space groups. Exposition here mostly follows ref. [111] with additional details supplemented from refs. [95, 112–114].

A.1 Basic Overview of Group Theory

A group $\mathbb{G}$ is any set where an operation called group multiplication is defined with the following properties:

1. The group is closed under the multiplication, that is $g_1 g_2 \in \mathbb{G}, \forall g_1, g_2 \in \mathbb{G}$
2. There is an identity element $e \in \mathbb{G}$, such that $eg = g, \forall g \in \mathbb{G}$
3. For every $g \in \mathbb{G}$ there is unique inverse g^{-1} such that $gg^{-1} = e$
4. Multiplication is associative $g_1(g_2 g_3) = (g_1 g_2)g_3, \forall g_1, g_2, g_3 \in \mathbb{G}$

The number of elements in a group is called group order and is denoted by $|\mathbb{G}|$. If every element of a group $\mathbb{G}$ is a product of elements g_i, where $i = 1..M < |\mathbb{G}|$, we call the elements g_i group generators. For every generator g of a finite group, a positive integer

n exists, such that $g^n = e$. Group with just one generator is called cyclic group, and in such a group, every element is a power of the generator. If all elements of the group commute under the multiplication, the group is called Abelian. Every cyclic group is Abelian.

If any subset of the group $\mathbb{H} \subset \mathbb{G}$ is a group on its own, it is called a subgroup and is denoted $\mathbb{H} < \mathbb{G}$. The order of the subgroup is a divisor of the group order and the number $|\mathbb{G}|/|\mathbb{H}| = |\mathbb{G} : \mathbb{H}|$ is called index of the subgroup $\mathbb{H}$. Every subgroup $\mathbb{H} < \mathbb{G}$ defines a decomposition of the group into a set of disjoint left(right) cosets $\mathbb{G} = \oplus_{i=1}^{|\mathbb{G}:\mathbb{H}|} g_i\mathbb{H}$ ($\mathbb{G} = \oplus_{i=1}^{|\mathbb{G}:\mathbb{H}|} \mathbb{H}g_i$), where $g_i \notin \mathbb{H}$. Cosets are not unique, and depend on the choice of g_i. For every two left cosets $g_i\mathbb{H}$ and $g_j\mathbb{H}$, the product $g_i\mathbb{H}g_j\mathbb{H} = g_k\mathbb{H}$ will be a left coset too (where product of cosets is defined as $g_i\mathbb{H}g_j\mathbb{H} = \oplus_{h,h' \in \mathbb{H}} g_i h g_j h'$). The same holds for right cosets. The set of cosets with coset multiplication forms a group of order $|\mathbb{G} : \mathbb{H}|$, called a factor group $\mathbb{F} = \mathbb{G}/\mathbb{H}$.

If a mapping f between the two groups $f : \mathbb{G} \to \mathbb{F}$ is given, such that it preserves the structure of multiplication, that is $f(g_1)f(g_2) = f(g_1g_2), \forall g_1, g_2 \in \mathbb{G}$, then the mapping f is called homomorphism, and the groups $\mathbb{G}$ and $\mathbb{F}$ are homomorphic. If f is bijective, it is an isomorphism, and if $\mathbb{F} = \mathbb{G}$, it is an automorphism. Every automorphism is an isomorphism.

Every element g of the group defines an automorphism f_g, called conjugation defined as $f_g(h) = ghg^{-1}$. If a subset $\mathbb{H} \subset \mathbb{G}$ of the group is closed under the conjugation by all group elements, it is called a conjugacy class and every group can be partitioned into a set of disjoint conjugacy classes. If, additionally, a conjugacy class $\mathbb{H}$ is a subgroup, it is called an invariant subgroup and denoted $\mathbb{H} \triangleleft \mathbb{G}$. A group $\mathbb{G} = \mathbb{H}_1\mathbb{H}_2$ is a direct product of its disjoint (with the exception of the unit element) invariant subgroups $\mathbb{H}_1$ and $\mathbb{H}_2$ if every element of $\mathbb{G}$ can be written as a product of elements from $\mathbb{H}_1$ and $\mathbb{H}_2$.

If there is a decomposition series of a group $\mathbb{G}$, given by $\mathbb{G}_0 \triangleleft \mathbb{G}_1 \triangleleft ... \triangleleft \mathbb{G}$, where at every decomposition step, the factor group is Abelian, the group is called solvable. This is important concept, since all space groups are solvable, and there is always $\mathbb{G}_0$ which is cyclic. Furthermore for all space groups, the order of factor groups of the decomposition $|\mathbb{G}_{i+1} : \mathbb{G}_i|$ is either two or three, and consequently, all factor groups are also cyclic.

A.2 Representation Theory

A homomorphism $D : \mathbb{G} \to \mathbb{L}(\mathbb{V})$ from the group $\mathbb{G}$ onto a set of linear operators $\mathbb{L}$ acting over an n-dimensional vector space $\mathbb{V}$, is called a representation of the group of dimension n. If $D(\mathbb{G})$ is injective, the representation is called faithful. This distinction

is made, because representations don't need to be faithful, and, for example, mapping, such that every group element is represented by unity, is also a representation, called unit representation.

If we fix a basis in $\mathbb{V}$, elements of $\mathbb{L}(\mathbb{V})$ will be represented by n-dimensional matrices, thus mapping every $g \in \mathbb{G}$ onto a matrix $\hat{\mathrm{D}}(g) \in \mathbb{L}(\mathbb{V})$. Any nonsingular linear operator $S : \mathbb{V} \to \mathbb{U}$, represented by a matrix $\hat{\mathrm{S}}$, defines an isomorphic representation D' over a vector space $\mathbb{U}$ through the relation $\hat{\mathrm{D}}'(g) = \hat{\mathrm{S}}\hat{\mathrm{D}}(g)\hat{\mathrm{S}}^{-1}, \forall g$. We say then, that representations D and D' are equivalent, since the multiplication rule between matrices is the same in both representations. In general, for every representation of the group, there will be infinitely many equivalent representations.

In group theory applications in physics, the vector space $\mathbb{V}$ can be, for example, a Hilbert space containing quantum mechanical states of the system, or in case of a geometrical problem, an Euclidean space. Since symmetries of the system are isometries of the relevant configuration space, only representations by (anti)unitary matrices are of interest.

Additionally, if $\hat{\mathrm{D}}(g)$ represents a symmetry of the system, it should commute with the Hamiltonian of the system which means that any invariant subspace of $\hat{\mathrm{D}}(g)$ will also be an invariant subspace of the Hamiltonian, allowing us to analyze the eigenvalue spectrum of the system without having to solve the Schrödinger equation, which might be a difficult task. It is thus useful to determine all nontrivial subspaces of $\mathbb{V}$ which are invariant under all $\hat{\mathrm{D}}(g)$. If there are no such subspaces, then the representation D is called irreducible, otherwise, the representation is reducible. Irreducible representations will be denoted by $D^{(\boldsymbol{\mu})}$, where the index μ is used to enumerate nonequivalent irreducible representations.

Thus, if we have a reducible representation, we can decompose it into a sum of irreducible representations. We understand this in a sense of decomposition of $\mathbb{V}$ into irreducible subspaces $\mathbb{V}_\mu$ as $\mathbb{V} = \oplus_{\mu,t_\mu} \mathbb{V}_{\mu t_\mu}$. An additional index t_μ is used here, because when $\mathbb{V}$ is decomposed, matrices of D will be represented by block-diagonal matrices, where the μ-th block will correspond to the irreducible representation $D^{(\mu)}$, which can occur more than once, so that the index $t_\mu = 1...a_\mu$ is needed to enumerate multiple occurrences of the block $D^{(\mu)}$. We can thus symbolically write decomposition of D as $D = \oplus_\mu a_\mu D^{(\mu)}$.

A.3 Induction of Irreducible Representations

The task is now to determine all nonequivalent unitary irreducible representations. For a finite group, there will be a finite number of such irreducible representations. In general, the number of nonequivalent irreducible representations will be equal to the number of conjugacy classes of the group.

When a group is a direct product of two or more of it's invariant subgroups, it's irreducible representations are simply a tensor product of irreducible representations of the subgroups. However, in general, that is not the case and a more sophisticated approach is required.

Since for space groups, the decomposition series to invariant subgroups always ends with an Abelian subgroup, the strategy to find all irreducible representations will consist of finding the irreducible representations of the Abelian subroup, and then moving up the decomposition chain and inducing the irreducible representations from the irreducible representation s of the subgroup.

The starting point for searching irreducible representations is the first Schur's lemma which states that only the scalar matrix commutes with all the matrices of an irreducible representation. This means that an Abelian group is represented by scalars, or in other words, it has only one-dimensional irreducible representations. Since, in an Abelian group, every element is in a conjugacy class by itself, the number of inequivalent irreducible representations will be equal to the group order.

The Abelian groups of interests for representations of space groups are cyclic, and since cyclic groups consist of powers of a single generator for which $g^n = 1$, where n is group order, all irreducible representations of the generator will be given as n-th roots of unity. With this observation, all irreducible representations of cyclic groups can easily be obtained.

The problem of finding irreducible representations of the group, from its subgroup is solved by the induction procedure which will be briefly outlined below.

Let us assume that we have a subgroup $\mathbb{H} < \mathbb{G}$ of index n and decompose the group $\mathbb{G}$ into left cosets with representatives $g_i, i = 1...n$. Let D be a d_D-dimensional representation of $\mathbb{H}$. The induced representation $D \uparrow \mathbb{G}$ of $\mathbb{G}$ is defined as

$$(\hat{\mathrm{D}} \uparrow \mathbb{G})(g) = \sum_{i,j=1}^{n} \sum_{h \in \mathbb{H}} \delta(t_i^{-1} g t_j, h) \hat{\mathrm{E}}_{ij} \otimes \hat{\mathrm{D}}(h), \tag{A.1}$$

where $\hat{\mathrm{E}}_{ij}$ are matrices of the n-dimensional Weyl basis defined as $[\hat{\mathrm{E}}_{ij}]_{pq} = \delta_{ip}\delta_{jq}$. Matrices of $D \uparrow \mathbb{G}$ consist of $n \times n$ d_D-dimensional blocks, such that the ij-th block is equal to $\hat{\mathrm{D}}(h)$ when $t_i^{-1} g t_j = h$ and zero otherwise.

Conversely, if D is a representation of the group $\mathbb{G}$, the subduced representation $D \downarrow \mathbb{H}$ to the subgroup $\mathbb{H} < \mathbb{G}$ can be defined just by taking the subset of matrices of D corresponding to elements of $\mathbb{H}$.

Let us restrict ourselves to the case where $\mathbb{H} \triangleleft \mathbb{G}$. We now define the g-conjugate representation ($g \in \mathbb{G}$) of the representation D of $\mathbb{H}$ as the representation where every element $h \in \mathbb{H}$ is represented by $\hat{\mathrm{D}}_g(h) = \hat{\mathrm{D}}(ghg^{-1})$. Because $ghg^{-1} \in \mathbb{H}$, the representation D_g consists of the same matrices as D, just differently assigned to the elements of $\mathbb{H}$. If $D^{(\mu)}$ is an irreducible representation of $\mathbb{H}$, the g-conjugated representation will also be an irreducible representation , which can either be equivalent or nonequivalent to it. We thus define the orbit O_μ of the irreducible representation $D^{(\mu)}$ as a set of all nonequivalent irreducible representations obtained from $D^{(\mu)}$ by g-conjugations with all $g \notin \mathbb{H}$. We also define the little group $\mathbb{L}_\mu$ of irreducible representation $D^{(\mu)}$ as a subgroup of $\mathbb{G}$ consisting of all elements g such that g-conjugation yields an irreducible representation equivalent to $D^{(\mu)}$. It is obvious that $\mathbb{H} < \mathbb{L}_\mu < \mathbb{G}$.

Any irreducible representation $D_A^{(\nu)}$ of $\mathbb{L}_\mu$ whose subduction to $\mathbb{H}$ contains $D^{(\mu)}$ at least once, is called allowed irreducible representation and the induced representation $D_A^{(\nu)} \uparrow \mathbb{G}$ is an irreducible representation of $\mathbb{G}$.

We can put this to use when $|\mathbb{G} : \mathbb{H}|$ is two or three. In this case coset representatives are $\{e, s\}$ and $\{e, s, s^2\}$ respectively. Since two and three are prime numbers and $\mathbb{H} < \mathbb{L}_\mu < \mathbb{G}$, we can either have that $\mathbb{L}_\mu = \mathbb{H}$ or $\mathbb{L}_\mu = \mathbb{G}$.

In case where $\mathbb{L}_\mu = \mathbb{G}$, the irreducible representation D^μ of $\mathbb{H}$ will also be an irreducible representation of $\mathbb{G}$. We can find matrices representing the coset elements by using the condition that for the coset representative we have $\hat{\mathrm{D}}^{(\mu)}(s^{n=2,3}) = \hat{\mathrm{D}}^\mu(h = s^n)$. This condition will yield two(three) matrices representing s which will result in 2(3) irreducible representations $D^{(\mu,i)}, i = 1..2(3)$ of $\mathbb{G}$ induced from $\mathbb{H}$. The matrices of induced irreducible representations for the case where $|\mathbb{G} : \mathbb{H}| = 2$ are

$$\begin{aligned} \hat{\mathrm{D}}^{(\mu,1)}(h) &= \hat{\mathrm{D}}^{(\mu)}(h) & \hat{\mathrm{D}}^{(\mu,1)}(sh) &= \hat{\mathrm{S}}\hat{\mathrm{D}}^{(\mu)}(h) \\ \hat{\mathrm{D}}^{(\mu,2)}(h) &= \hat{\mathrm{D}}^{\mu}(h) & \hat{\mathrm{D}}^{(\mu,2)}(sh) &= -\hat{\mathrm{S}}\hat{\mathrm{D}}^{(\mu)}(h) \end{aligned} \tag{A.2}$$

where $\hat{\mathrm{S}}$ is such that $\hat{\mathrm{S}}^2 = \hat{\mathrm{D}}^\mu(s^2)$ and $\hat{\mathrm{D}}^{(\mu)}(shs^{-1}) = \hat{\mathrm{S}}\hat{\mathrm{D}}^{(\mu)}(h)\hat{\mathrm{S}}^{-1}$. When $|\mathbb{G} : \mathbb{H}| = 3$

$$\begin{aligned} \hat{\mathrm{D}}^{(\mu,1)}(h) &= \hat{\mathrm{D}}^{(\mu)}(h) & \hat{\mathrm{D}}^{(\mu,1)}(sh) &= \hat{\mathrm{S}}\hat{\mathrm{D}}^{(\mu)}(h) \\ \hat{\mathrm{D}}^{(\mu,2)}(h) &= \hat{\mathrm{D}}^{(\mu)}(h) & \hat{\mathrm{D}}^{(\mu,2)}(sh) &= e^{2\pi i/3}\hat{\mathrm{S}}\hat{\mathrm{D}}^{(\mu)}(h) \\ \hat{\mathrm{D}}^{(\mu,3)}(h) &= \hat{\mathrm{D}}^{\mu}(h) & \hat{\mathrm{D}}^{(\mu,3)}(s^2h) &= e^{-2\pi i/3}\hat{\mathrm{S}}\hat{\mathrm{D}}^{(\mu)}(h) \end{aligned} \tag{A.3}$$

where $\hat{\mathrm{S}}$ is such that $\hat{\mathrm{S}}^3 = \hat{\mathrm{D}}^{\mu}(s^3)$ and $\hat{\mathrm{D}}^{(\mu)}(shs^{-1}) = \hat{\mathrm{S}}\hat{\mathrm{D}}^{(\mu)}(h)\hat{\mathrm{S}}^{-1}$.

In case when $\mathbb{L}_{\mu} = \mathbb{H}$, the induction formula (A.1) can be used, resulting in irreducible representations of $\mathbb{G}$. For the case of index two

$$\hat{\mathrm{D}}^{(\mu)}(h) = \begin{bmatrix} \hat{\mathrm{D}}^{(\mu)}(h) & 0 \\ 0 & \hat{\mathrm{D}}^{(\mu)}_{s}(h) \end{bmatrix} \qquad \hat{\mathrm{D}}^{(\mu)}(sh) = \begin{bmatrix} 0 & \hat{\mathrm{D}}^{\mu}(s^2)\hat{\mathrm{D}}^{(\mu)}_{s}(h) \\ \hat{\mathrm{D}}^{(\mu)}(h) & 0 \end{bmatrix} \tag{A.4}$$

and for the case of index three

$$\begin{aligned} \hat{\mathrm{D}}^{(\mu)}(h) &= \begin{bmatrix} \hat{\mathrm{D}}^{(\mu)}(h) & 0 & 0 \\ 0 & \hat{\mathrm{D}}^{(\mu)}_{s}(h) & 0 \\ 0 & 0 & \hat{\mathrm{D}}^{(\mu)}_{s^2}(h) \end{bmatrix} \\ \hat{\mathrm{D}}^{(\mu)}(sh) &= \begin{bmatrix} 0 & 0 & \hat{\mathrm{D}}^{(\mu)}(s^3)\hat{\mathrm{D}}^{(\mu)}_{s^2}(h) \\ \hat{\mathrm{D}}^{(\mu)}(h) & 0 & 0 \\ 0 & \hat{\mathrm{D}}^{(\mu)}_{s}(h) & 0 \end{bmatrix} \\ \hat{\mathrm{D}}^{(\mu)}(s^2h) &= \begin{bmatrix} 0 & \hat{\mathrm{D}}^{(\mu)}(s^3)\hat{\mathrm{D}}^{(\mu)}_{s}(h) & 0 & \\ 0 & 0 & \hat{\mathrm{D}}^{(\mu)}(s^3)\hat{\mathrm{D}}^{(\mu)}_{s^2}(h) & 0 \\ \hat{\mathrm{D}}^{(\mu)}(h) & 0 & 0 & \end{bmatrix} \end{aligned} \tag{A.5}$$

Formulas (A.2), (A.3), (A.4) and (A.5) are sufficient to induce all irreducible representations of every space group in a step by step procedure.

A.4 Induction of Irreducible Representations of Space Groups

Let us now outline the general procedure for induction of irreducible representations in an arbitrary spacegroup $\mathbb{S}$. $\mathbb{S}$ is composed of operations whose action on a general point $\boldsymbol{r}$ in the Euclidean space is given by $\boldsymbol{r} \to \boldsymbol{r}' = \hat{\mathrm{U}}\boldsymbol{r} + \boldsymbol{t}$, where $\hat{\mathrm{U}}$ is a point group operation. In Seitz notation, this operation is denoted by $[\hat{\mathrm{U}}|\boldsymbol{t}]$. The multiplication rule for space group operations is given by $[\hat{\mathrm{U}}_1|\boldsymbol{t}_1][\hat{\mathrm{U}}_2|\boldsymbol{t}_2] = [\hat{\mathrm{U}}_1\hat{\mathrm{U}}_2|\hat{\mathrm{U}}_1\boldsymbol{t}_2 + \boldsymbol{t}_1]$ and the inverse is given by $[\hat{\mathrm{U}}|\boldsymbol{t}]^{-1} = [\hat{\mathrm{U}}^{-1}| - \hat{\mathrm{U}}^{-1}\boldsymbol{t}]$.

When points $\boldsymbol{r}$ are restricted to lie on a periodic lattice, the space group operations will be $[\hat{\mathrm{U}}_m|\boldsymbol{R}_n + \boldsymbol{\tau}_m]$, where $\boldsymbol{R}_n$ are translation vectors connecting points on a lattice, and $\hat{\mathrm{U}}_m$ and $\boldsymbol{\tau}_m$ are point group operations and fractional translations respectively, under whose simultaneous application the lattice remains invariant (for pure point group operation $\hat{\mathrm{U}}_m$ the corresponding fractional translation is $\boldsymbol{\tau}_m = 0$). Here the lattice is

assumed to have N points in total, and that periodic boundary conditions are imposed so that there is a finite number of translations.

Pure translations $[\hat{\mathrm{I}}|\boldsymbol{R}_n]$ comprise a group $\mathbb{T} \triangleleft \mathbb{S}$, which is a direct product of three cyclic groups in addition. Thus, it is very easy to find its irreducible representations and then use them as a starting point in the induction of irreducible representations of $\mathbb{S}$. Irreducible representations $\mathbb{T}$ are given by a well known result $\hat{\mathrm{D}}^{(\boldsymbol{k})}(\boldsymbol{R}_n) = e^{-i\boldsymbol{k}\cdot\boldsymbol{R}_n}$.

Let a space group decomposition in terms of left cosets of $\mathbb{T}$ be $\mathbb{S} = \oplus_m[\hat{\mathrm{U}}_m|\boldsymbol{\tau}_m]\mathbb{T}$. If we take arbitrary space group operation $s = [\hat{\mathrm{U}}|\boldsymbol{t}]$, and find a conjugate of $D^{(\boldsymbol{k})}$ we arrive at the following

$$\hat{\mathrm{D}}^{(\boldsymbol{k})}(s[\hat{\mathrm{I}}|\boldsymbol{R}_n]s^{-1}) = \hat{\mathrm{D}}^{(\boldsymbol{k})}([\hat{\mathrm{U}}|\boldsymbol{t}][\hat{\mathrm{I}}|\boldsymbol{R}_n][\hat{\mathrm{U}}^{-1}|-\hat{\mathrm{U}}^{-1}\boldsymbol{t}]) = \hat{\mathrm{D}}^{(\boldsymbol{k})}([\hat{\mathrm{I}}|\hat{\mathrm{U}}\boldsymbol{R}_n]) = \hat{\mathrm{D}}^{(\hat{\mathrm{U}}^{-1}\boldsymbol{k})}(\boldsymbol{R}_n)$$

because $\boldsymbol{k}\cdot(\hat{\mathrm{U}}\boldsymbol{R}_n) = (\hat{\mathrm{U}}^{-1}\boldsymbol{k})\cdot\boldsymbol{R}_n$. In other words, conjugation of an irreducible representation $D^{(\boldsymbol{k})}$ by a space group element $[\hat{\mathrm{U}}|\boldsymbol{t}]$ yields the irreducible representation $D^{(\hat{\mathrm{U}}^{-1}\boldsymbol{k})}$. This means that the orbit of an irreducible representation $D^{(\boldsymbol{k})}$ will contain the irreducible representations for all nonequivalent $\boldsymbol{k}'$ obtained from $\boldsymbol{k}$ by application of all point group operations of coset representatives. The orbit of $\boldsymbol{k}$ is called star in the context of space groups. The Little group of $D^{(\boldsymbol{k})}$ consists of $\mathbb{T}$, augmented by operations $[\hat{\mathrm{U}}_{\boldsymbol{k},i}|\boldsymbol{\tau}_{\boldsymbol{k},i}]$ such that $\hat{\mathrm{U}}_{\boldsymbol{k},i}\boldsymbol{k} = \boldsymbol{k} + \boldsymbol{K}$, where $\boldsymbol{K}$ is a vector of the reciprocal lattice. As a result, a general element of the little group $\mathbb{L}_{\boldsymbol{k}}$ will have the form $[\hat{\mathrm{U}}_{\boldsymbol{k},i}|\boldsymbol{R}_n + \boldsymbol{\tau}_{\boldsymbol{k},i}]$. Connected to the concept of the Little group is the Little co-group $\mathbb{L}^{\mathrm{C}}_{\boldsymbol{k}}$, which consist only of the point group operators $\hat{\mathrm{U}}_{\boldsymbol{k},i}$. It is not hard to see that the Little co-group is isomorphic to the factor group $\mathbb{L}_{\boldsymbol{k}}/\mathbb{T}$.

The remaining problem in the induction procedure is to find allowed irreducible representations of the little group. The little group can be decomposed into left cosets of $\mathbb{T}$ as $\mathbb{L}_{\boldsymbol{k}} = \oplus_i[\hat{\mathrm{U}}_{\boldsymbol{k},i}|\boldsymbol{\tau}_{\boldsymbol{k},i}]\mathbb{T}$. Multiplication of coset representatives results in

$$[\hat{\mathrm{U}}_{\boldsymbol{k},i}|\boldsymbol{\tau}_{\boldsymbol{k},i}][\hat{\mathrm{U}}_{\boldsymbol{k},j}|\boldsymbol{\tau}_{\boldsymbol{k},j}] = [\hat{\mathrm{U}}_{\boldsymbol{k},i}\hat{\mathrm{U}}_{\boldsymbol{k},j}|\boldsymbol{\tau}_{\boldsymbol{k},i} + \hat{\mathrm{U}}_{\boldsymbol{k},i}\boldsymbol{\tau}_{\boldsymbol{k},j} + \boldsymbol{\tau}_{\boldsymbol{k},k} - \boldsymbol{\tau}_{\boldsymbol{k},k}] = [\hat{\mathrm{U}}_{\boldsymbol{k},k}|\boldsymbol{\tau}_{\boldsymbol{k},k} + \boldsymbol{R}_{ij}] = [\hat{\mathrm{I}}|\boldsymbol{R}_{ij}][\hat{\mathrm{U}}_{\boldsymbol{k},k}|\boldsymbol{\tau}_{\boldsymbol{k},k}] \quad \text{(A.6)}$$

where the lattice vector $\boldsymbol{R}_{ij} = \boldsymbol{\tau}_{\boldsymbol{k},i} + \hat{\mathrm{U}}_{\boldsymbol{k},i}\boldsymbol{\tau}_{\boldsymbol{k},j} - \boldsymbol{\tau}_{\boldsymbol{k},k}$ has been introduced.

Let $\Delta^{(\boldsymbol{k},\mu)}$ be an allowed irreducible representation of the $\mathbb{L}_{\boldsymbol{k}}$. Since it is an allowed irreducible representation , then $\hat{\Delta}^{(\boldsymbol{k},\mu)}[\hat{\mathrm{I}}|\boldsymbol{R}_n]$ must reduce to $\hat{\mathrm{D}}^{(\boldsymbol{k})}(\boldsymbol{R}_n)$. This allows us to write the representation of (A.6) as

$$\hat{\Delta}^{(\boldsymbol{k},\mu)}([\boldsymbol{U}_{\boldsymbol{k},i}|\boldsymbol{\tau}_{\boldsymbol{k},i}])\hat{\Delta}^{(\boldsymbol{k},\mu)}([\boldsymbol{U}_{\boldsymbol{k},j}|\boldsymbol{\tau}_{\boldsymbol{k},j}]) = \hat{\mathrm{D}}^{(\boldsymbol{k})}(\boldsymbol{R}_{ij})\hat{\Delta}^{(\boldsymbol{k},\mu)}([\boldsymbol{U}_{\boldsymbol{k},k}|\boldsymbol{\tau}_{\boldsymbol{k},k}]) \tag{A.7}$$

To simplify notation, we can drop the translational part of the coset representative and write just $\hat{\Delta}^{(\boldsymbol{k},\mu)}(\hat{\mathrm{U}}_{\boldsymbol{k},i}) = \hat{\Delta}^{(\boldsymbol{k},\mu)}([\hat{\mathrm{U}}_{\boldsymbol{k},i}|\boldsymbol{\tau}_{\boldsymbol{k},i}])$. With this, representation can be introduced $\hat{\Delta}_{\mathrm{C}}^{(\boldsymbol{k},\mu)}(\hat{\mathrm{U}}_{\boldsymbol{k},i}) = e^{i\boldsymbol{k}\cdot\boldsymbol{\tau}_{\boldsymbol{k},i}}\hat{\Delta}^{(\boldsymbol{k},\mu)}(\hat{\mathrm{U}}_{\boldsymbol{k},i})$. The multiplication rule for the representatives $\hat{\Delta}_{\mathrm{C}}^{(\boldsymbol{k},\mu)}(\hat{\mathrm{U}}_{\boldsymbol{k},i})$ is, with the help of (A.7)

$$\begin{aligned}\hat{\Delta}_{\mathrm{C}}^{(\boldsymbol{k},\mu)}(\hat{\mathrm{U}}_{\boldsymbol{k},i})\hat{\Delta}_{\mathrm{C}}^{(\boldsymbol{k},\mu)}(\hat{\mathrm{U}}_{\boldsymbol{k},j}) &= e^{i\boldsymbol{k}\cdot(\boldsymbol{\tau}_{\boldsymbol{k},i}+\boldsymbol{\tau}_{\boldsymbol{k},j})}\hat{\mathrm{D}}^{(\boldsymbol{k})}(\boldsymbol{R}_{ij})\hat{\Delta}^{(\boldsymbol{k},\mu)}(\hat{\mathrm{U}}_{\boldsymbol{k},k}) = \\ &e^{i\boldsymbol{k}\cdot(\boldsymbol{\tau}_{\boldsymbol{k},i}+\boldsymbol{\tau}_{\boldsymbol{k},j})}e^{-i\boldsymbol{k}\cdot(\boldsymbol{\tau}_{\boldsymbol{k},i}+\hat{\mathrm{U}}_{\boldsymbol{k},i}\boldsymbol{\tau}_{\boldsymbol{k},j}-\boldsymbol{\tau}_{\boldsymbol{k},k})}\hat{\Delta}^{(\boldsymbol{k},\mu)}(\hat{\mathrm{U}}_{\boldsymbol{k},k}) = \\ &e^{-i\boldsymbol{K}_i\cdot\boldsymbol{\tau}_{\boldsymbol{k},j}}e^{i\boldsymbol{k}\cdot\boldsymbol{\tau}_{\boldsymbol{k},j}}\hat{\Delta}^{(\boldsymbol{k},\mu)}(\hat{\mathrm{U}}_{\boldsymbol{k},k}) = e^{-i\boldsymbol{K}_i\cdot\boldsymbol{\tau}_{\boldsymbol{k},j}}\hat{\Delta}_{\mathrm{C}}^{(\boldsymbol{k},\mu)}(\hat{\mathrm{U}}_{\boldsymbol{k},k})\end{aligned} \tag{A.8}$$

where $\boldsymbol{K}_i$ is such that $\hat{\mathrm{U}}_{\boldsymbol{k},i}^{-1}\boldsymbol{k} = \boldsymbol{k} + \boldsymbol{K}_i$ is satisfied. From eq. (A.8) it follows that $\Delta_{\mathrm{C}}^{(\boldsymbol{k},\mu)}$ forms a projective representation of $\mathbb{L}_{\boldsymbol{k}}^{\mathrm{C}}$ with multipliers given by $m(\hat{\mathrm{U}}_{\boldsymbol{k},i}, \hat{\mathrm{U}}_{\boldsymbol{k},j}) = e^{-i\boldsymbol{K}_i\cdot\boldsymbol{\tau}_{\boldsymbol{k},j}}$. Moreover, this representation is irreducible, since $\Delta^{(\boldsymbol{k},\mu)}$ is irreducible by assumption and $\mathbb{L}_{\boldsymbol{k}}^{\mathrm{C}}$ is isomorphic to $\mathbb{L}_{\boldsymbol{k}}/\mathbb{T}$. When any of the following is fullfiled

- $\boldsymbol{k}$ lies inside the Brillouin zone
- $\mathbb{S}$ is a symmorphic space group
- $\mathbb{L}_{\boldsymbol{k}}$ is a symmorphic space group

then the projective irreducible representation multiplers reduce to unity, $\Delta_{\mathrm{C}}^{(\boldsymbol{k},\mu)}$ is an irreducible representation of $\mathbb{L}_{\boldsymbol{k}}^{\mathrm{C}}$ and the allowed irreducible representations of the little group $\mathbb{L}_{\boldsymbol{k}}$ are given by

$$\hat{\Delta}^{(\boldsymbol{k},\mu)}([\hat{\mathrm{U}}_{\boldsymbol{k},i}|\boldsymbol{R}_n + \boldsymbol{\tau}_{\boldsymbol{k},i}]) = e^{-i\boldsymbol{k}\cdot(\boldsymbol{R}_n+\boldsymbol{\tau}_{\boldsymbol{k},i})}\hat{\Delta}_{\mathrm{C}}^{(\boldsymbol{k},\mu)}(\hat{\mathrm{U}}_{\boldsymbol{k},i}) \tag{A.9}$$

Thus, for any space group and any $\boldsymbol{k}$ in the interior of the Brillouin zone, the allowed irreducible representations can be found by taking all irreducible representations of the little co-group of $\boldsymbol{k}$ and by using eq. (A.9). And finally, irreducible representations of the full space group can be found by using induction formulas (A.2)-(A.5).

Appendix B

Irreducible Representations and Projectors for Iron Pnictides

This appendix contains the atomic positions in fractional coordinates, induced irreducible representations and the corresponding projectors for the cases in 8. The order of atomic positions in the permutation matrices $\hat{\mathrm{K}}$ is the same as in the table of positions. The projectors omit the exponentials because our implementation of the unfolding relies on the band projections onto localized states which already contain the appropriate exponentials, as calculated by the VASP code.

B.1 FeSe doubled along the a-axis

p	Atom	x	y	z
1	Fe	1/8	1/4	0
2	Fe	2/8	3/4	0
3	Fe	3/8	1/4	0
4	Fe	4/8	3/4	0
5	Se	1/8	3/4	z
6	Se	2/8	1/4	-z
7	Se	1/8	3/4	z
8	Se	2/8	1/4	-z

TABLE B.1: Atomic positions in the supercell of FeSe, given in fractional coordinates with respect to the orthorhombic unit cell vectors $\boldsymbol{a}$, $\boldsymbol{b}$ and $\boldsymbol{c}$.

Δ	$[1\|\boldsymbol{R}_n]$	$[1\|\boldsymbol{R}_n+\boldsymbol{\tau}]$
$(\boldsymbol{k},0)$	$\exp(-\boldsymbol{k}\cdot\boldsymbol{R}_n)$	$\exp(-\boldsymbol{k}\cdot(\boldsymbol{R}_n+\boldsymbol{\tau}))$
$(\boldsymbol{k},1)$	$\exp(-\boldsymbol{k}\cdot\boldsymbol{R}_n)$	-$\exp(-\boldsymbol{k}\cdot(\boldsymbol{R}_n+\boldsymbol{\tau}))$

TABLE B.2: Induced irreducible representations; $\boldsymbol{\tau}=\boldsymbol{a}/2$.

$$\hat{\mathrm{P}}_{\boldsymbol{k},0}=\frac{1}{\sqrt{2}}\oplus_{i=1}^{2}\begin{bmatrix}1&0&1&0\\0&1&0&1\\1&0&1&0\\0&1&0&1\end{bmatrix}\otimes\hat{\mathrm{I}}_{n_i}$$

$$\hat{\mathrm{P}}_{\boldsymbol{k},1}=\frac{1}{\sqrt{2}}\oplus_{i=1}^{2}\begin{bmatrix}1&0&-1&0\\0&1&0&-1\\-1&0&1&0\\0&-1&0&1\end{bmatrix}\otimes\hat{\mathrm{I}}_{n_i}$$

where $\hat{\mathrm{I}}_n$ is a n by n unit matrix. Since we are interested in $3d$ orbitals of iron, and $4p$ orbitals of selenium, $n_1=5$ for iron atoms and $n_2=3$ for selenium atoms.

B.2 $Ca(FeAs_{1-x}P_x)_2$

p	Atom	x	y	z
1	Fe	3/4	1/4	1/4
2	Fe	1/4	3/4	3/4
3	Fe	1/4	3/4	1/4
4	Fe	3/4	1/4	3/4
5	Fe	1/4	1/4	3/4
6	Fe	3/4	3/4	1/4
7	Fe	3/4	3/4	3/4
8	Fe	1/4	1/4	1/4
9	As	0	1/2	1/2-z
10	As	0	1/2	1/2+z
11	As	0	0	1-z
12	As	0	0	z
13	As	1/2	1/2	1-z
14	As	1/2	1/2	z
15	As	1/2	0	1/2-z
16	P	1/2	0	1/2+z

TABLE B.3: Atomic positions in $Ca(FeAs_{1-x}P_x)_2$, given in fractional coordinates with respect to the orthorhombic unit cell vectors $\boldsymbol{a}$, $\boldsymbol{b}$ and $\boldsymbol{c}$. The fractional coordinates and lattice vectors are taken before the structure optimization. This choice does not impact the unfolding.

Δ	$[1\|\boldsymbol{R}_n]$	$[1\|\boldsymbol{R}_n+\boldsymbol{\tau}_1]$	$[1\|\boldsymbol{R}_n+\boldsymbol{\tau}_2]$	$[1\|\boldsymbol{R}_n+\boldsymbol{\tau}_3]$
$(\boldsymbol{k},0)$	$\exp(-\boldsymbol{k}\cdot\boldsymbol{R}_n)$	$\exp(-\boldsymbol{k}\cdot(\boldsymbol{R}_n+\boldsymbol{\tau}_1))$	$\exp(-\boldsymbol{k}\cdot(\boldsymbol{R}_n+\boldsymbol{\tau}_2))$	$\exp(-\boldsymbol{k}\cdot(\boldsymbol{R}_n+\boldsymbol{\tau}_3))$
$(\boldsymbol{k},1)$	$\exp(-\boldsymbol{k}\cdot\boldsymbol{R}_n)$	-$\exp(-\boldsymbol{k}\cdot(\boldsymbol{R}_n+\boldsymbol{\tau}_1))$	$\exp(-\boldsymbol{k}\cdot(\boldsymbol{R}_n+\boldsymbol{\tau}_2))$	-$\exp(-\boldsymbol{k}\cdot(\boldsymbol{R}_n+\boldsymbol{\tau}_3))$
$(\boldsymbol{k},2)$	$\exp(-\boldsymbol{k}\cdot\boldsymbol{R}_n)$	$\exp(-\boldsymbol{k}\cdot(\boldsymbol{R}_n+\boldsymbol{\tau}_1))$	-$\exp(-\boldsymbol{k}\cdot(\boldsymbol{R}_n+\boldsymbol{\tau}_2))$	-$\exp(-\boldsymbol{k}\cdot(\boldsymbol{R}_n+\boldsymbol{\tau}_3))$
$(\boldsymbol{k},3)$	$\exp(-\boldsymbol{k}\cdot\boldsymbol{R}_n)$	-$\exp(-\boldsymbol{k}\cdot(\boldsymbol{R}_n+\boldsymbol{\tau}_1))$	-$\exp(-\boldsymbol{k}\cdot(\boldsymbol{R}_n+\boldsymbol{\tau}_2))$	$\exp(-\boldsymbol{k}\cdot(\boldsymbol{R}_n+\boldsymbol{\tau}_3))$

TABLE B.4: Induced irreducible representations; $\boldsymbol{\tau}_1 = (\boldsymbol{a}+\boldsymbol{b})/2$, $\boldsymbol{\tau}_2 = (\boldsymbol{a}+\boldsymbol{c})/2$, $\boldsymbol{\tau}_3 = \boldsymbol{\tau}_1+\boldsymbol{\tau}_2$.

$$\hat{\mathrm{P}}_{\boldsymbol{k}\alpha} = \frac{1}{2}(\hat{\mathrm{B}}^{\mathrm{Fe}}_{\boldsymbol{k}\alpha}\otimes\hat{\mathrm{I}}_5)\oplus(\hat{\mathrm{B}}^{\mathrm{As}}_{\boldsymbol{k}\alpha}\otimes\hat{\mathrm{I}}_3)$$

where $\hat{\mathrm{I}}_n$ is a n by n unit matrix.

The subblocks corresponding to Fe atoms are

$$\hat{\mathrm{B}}^{\mathrm{Fe}}_{\boldsymbol{k},0} = \begin{bmatrix} 1 & 0 & 1 & 0 & 1 & 0 & 1 & 0 \\ 0 & 1 & 0 & 1 & 0 & 1 & 0 & 1 \\ 1 & 0 & 1 & 0 & 1 & 0 & 1 & 0 \\ 0 & 1 & 0 & 1 & 0 & 1 & 0 & 1 \\ 1 & 0 & 1 & 0 & 1 & 0 & 1 & 0 \\ 0 & 1 & 0 & 1 & 0 & 1 & 0 & 1 \\ 1 & 0 & 1 & 0 & 1 & 0 & 1 & 0 \\ 0 & 1 & 0 & 1 & 0 & 1 & 0 & 1 \end{bmatrix}$$

$$\hat{\mathrm{B}}^{\mathrm{Fe}}_{\boldsymbol{k},1} = \begin{bmatrix} 1 & 0 & -1 & 0 & 1 & 0 & -1 & 0 \\ 0 & 1 & 0 & -1 & 0 & 1 & 0 & -1 \\ -1 & 0 & 1 & 0 & -1 & 0 & 1 & 0 \\ 0 & -1 & 0 & 1 & 0 & -1 & 0 & 1 \\ 1 & 0 & -1 & 0 & 1 & 0 & -1 & 0 \\ 0 & 1 & 0 & -1 & 0 & 1 & 0 & -1 \\ -1 & 0 & 1 & 0 & -1 & 0 & 1 & 0 \\ 0 & -1 & 0 & 1 & 0 & -1 & 0 & 1 \end{bmatrix}$$

$$\hat{\mathrm{B}}^{\mathrm{Fe}}_{\boldsymbol{k},2} = \begin{bmatrix} 1 & 0 & 1 & 0 & -1 & 0 & -1 & 0 \\ 0 & 1 & 0 & 1 & 0 & -1 & 0 & -1 \\ 1 & 0 & 1 & 0 & -1 & 0 & -1 & 0 \\ 0 & 1 & 0 & 1 & 0 & -1 & 0 & -1 \\ -1 & 0 & -1 & 0 & 1 & 0 & 1 & 0 \\ 0 & -1 & 0 & -1 & 0 & 1 & 0 & 1 \\ -1 & 0 & -1 & 0 & 1 & 0 & 1 & 0 \\ 0 & -1 & 0 & -1 & 0 & 1 & 0 & 1 \end{bmatrix}$$

$$\hat{\mathrm{B}}^{\mathrm{Fe}}_{\boldsymbol{k},3} = \begin{bmatrix} 1 & 0 & -1 & 0 & -1 & 0 & 1 & 0 \\ 0 & 1 & 0 & -1 & 0 & -1 & 0 & 1 \\ -1 & 0 & 1 & 0 & 1 & 0 & -1 & 0 \\ 0 & -1 & 0 & 1 & 0 & 1 & 0 & -1 \\ -1 & 0 & 1 & 0 & 1 & 0 & -1 & 0 \\ 0 & -1 & 0 & 1 & 0 & 1 & 0 & -1 \\ 1 & 0 & -1 & 0 & -1 & 0 & 1 & 0 \\ 0 & 1 & 0 & -1 & 0 & -1 & 0 & 1 \end{bmatrix}$$

The subblocks corresponding to As atoms are

$$\hat{\mathrm{B}}^{\mathrm{As}}_{\boldsymbol{k},0} = \begin{bmatrix} 1 & 0 & 1 & 0 & 1 & 0 & 1 & 0 \\ 0 & 1 & 0 & 1 & 0 & 1 & 0 & 1 \\ 1 & 0 & 1 & 0 & 1 & 0 & 1 & 0 \\ 0 & 1 & 0 & 1 & 0 & 1 & 0 & 1 \\ 1 & 0 & 1 & 0 & 1 & 0 & 1 & 0 \\ 0 & 1 & 0 & 1 & 0 & 1 & 0 & 1 \\ 1 & 0 & 1 & 0 & 1 & 0 & 1 & 0 \\ 0 & 1 & 0 & 1 & 0 & 1 & 0 & 1 \end{bmatrix}$$

$$\hat{\mathrm{B}}^{\mathrm{As}}_{\boldsymbol{k},0} = \begin{bmatrix} 1 & 0 & -1 & 0 & 1 & 0 & -1 & 0 \\ 0 & 1 & 0 & -1 & 0 & 1 & 0 & -1 \\ -1 & 0 & 1 & 0 & -1 & 0 & 1 & 0 \\ 0 & -1 & 0 & 1 & 0 & -1 & 0 & 1 \\ 1 & 0 & -1 & 0 & 1 & 0 & -1 & 0 \\ 0 & 1 & 0 & -1 & 0 & 1 & 0 & -1 \\ -1 & 0 & 1 & 0 & -1 & 0 & 1 & 0 \\ 0 & -1 & 0 & 1 & 0 & -1 & 0 & 1 \end{bmatrix}$$

$$\hat{\mathrm{B}}^{\mathrm{As}}_{\boldsymbol{k},0} = \begin{bmatrix} 1 & 0 & -1 & 0 & -1 & 0 & 1 & 0 \\ 0 & 1 & 0 & -1 & 0 & -1 & 0 & 1 \\ -1 & 0 & 1 & 0 & 1 & 0 & -1 & 0 \\ 0 & -1 & 0 & 1 & 0 & 1 & 0 & -1 \\ -1 & 0 & 1 & 0 & 1 & 0 & -1 & 0 \\ 0 & -1 & 0 & 1 & 0 & 1 & 0 & -1 \\ 1 & 0 & -1 & 0 & -1 & 0 & 1 & 0 \\ 0 & 1 & 0 & -1 & 0 & -1 & 0 & 1 \end{bmatrix}$$

$$\hat{\mathrm{B}}^{\mathrm{As}}_{\boldsymbol{k},0} = \begin{bmatrix} 1 & 0 & 1 & 0 & -1 & 0 & -1 & 0 \\ 0 & 1 & 0 & 1 & 0 & -1 & 0 & -1 \\ 1 & 0 & 1 & 0 & -1 & 0 & -1 & 0 \\ 0 & 1 & 0 & 1 & 0 & -1 & 0 & -1 \\ -1 & 0 & -1 & 0 & 1 & 0 & 1 & 0 \\ 0 & -1 & 0 & -1 & 0 & 1 & 0 & 1 \\ -1 & 0 & -1 & 0 & 1 & 0 & 1 & 0 \\ 0 & -1 & 0 & -1 & 0 & 1 & 0 & 1 \end{bmatrix}$$

B.3 Using the Glide-Mirror Group to Unfold the Band Structure of FeSe

p	Atom	x	y	z
1	Fe	1/4	1/4	0
2	Fe	3/4	3/4	0
3	Se	1/4	3/4	z
4	Se	3/4	1/4	-z

TABLE B.5: Atomic positions are given in fractional coordinates with respect to the tetragonal unit cell vectors $\boldsymbol{a}$, $\boldsymbol{b}$ and $\boldsymbol{c}$.

Δ	$[1\|\boldsymbol{R}_n]$	$[\hat{\sigma}_z\|\boldsymbol{R}_n+\boldsymbol{\tau}]$
$(\boldsymbol{k},0)$	$\exp(-\boldsymbol{k}\cdot\boldsymbol{R}_n)$	$\exp(-\boldsymbol{k}\cdot(\boldsymbol{R}_n+\boldsymbol{\tau}))$
$(\boldsymbol{k},1)$	$\exp(-\boldsymbol{k}\cdot\boldsymbol{R}_n)$	-$\exp(-\boldsymbol{k}\cdot(\boldsymbol{R}_n+\boldsymbol{\tau}))$

TABLE B.6: Induced irreducible representations; $\boldsymbol{\tau}=\boldsymbol{a}/2$.

$$\hat{\mathrm{P}}_{\boldsymbol{k},0}=\frac{1}{\sqrt{2}}\oplus_{i=1}^{2}\begin{bmatrix}1 & 1\\ 1 & 1\end{bmatrix}\otimes\hat{\mathrm{A}}_i$$

$$\hat{\mathrm{P}}_{\boldsymbol{k},1}=\frac{1}{\sqrt{2}}\oplus_{i=1}^{2}\begin{bmatrix}1 & -1\\ -1 & 1\end{bmatrix}\otimes\hat{\mathrm{A}}_i$$

with $\hat{\mathrm{A}}_1=\mathrm{diag}(1,-1,1,-1,1)$ and $\hat{\mathrm{A}}_2=\mathrm{diag}(1,-1,1)$, assuming orbital orbital indices are $\alpha=(3d_{xy},3d_{yz},3d_{z^2},3d_{xz},3d_{x^2-y^2})$ for Fe atoms and $\alpha=(4p_x,4p_z,4p_y)$ for As atoms.

Bibliography

[1] J. Kohanoff. *Electronic Structure Calculations for Solids and Molecules*. Cambridge University Press, 2006.

[2] M. C. Payne, M. P. Teter, D. C. Allan, T. A. Arias, and J. D. Joannopoulos. *Rev. Mod. Phys.*, 64:1045, 1992.

[3] M. Born and J. R. Oppenheimer. *Annalen der Physik*, 389:457, 1927.

[4] L. H. Thomas. *Proc. Cambridge Phill. Soc.*, 23:542, 1927.

[5] E. Fermi. *Rend. Accad. Naz. Lincei*, 6:602, 1927.

[6] P. Hohenberg and W. Kohn. *Physical Review*, 136:B864, 1964.

[7] W. Kohn and L. J. Sham. *Physical Review*, 140(4A):A113, 1965.

[8] T. C. Koopmans. *Physica*, 1:104, 1934.

[9] P. A. M. Dirac. *Proc. Cambridge Philos. Soc.*, 26:376, 1930.

[10] P. E. Blöchl. *Physical Review B*, 50:17953, 1994.

[11] C. Rostgaard. The projector augmented-wave method. URL http://arxiv.org/abs/0910.1921.

[12] K. Koepernik and H.Eschrig. *Physical Review B*, 59:1743, 1999.

[13] T. J. Dekker. Finding a zero by means of successive linear interpolation. In B. Dejon, editor, *Constructive Aspects of the Fundamental Theorem of Algebra*, 1969.

[14] R. P. Brent. *Algorithms for Minimization without Derivatives*. Prentice-Hall, 1973.

[15] P. Wolfe. *SIAM Review*, 11:226, 1969.

[16] P. Wolfe. *SIAM Review*, 13:185, 1971.

[17] C. G. Broyden. *J. I. Math. Appl.*, 6:76, 1970.

[18] R. Fletcher. *Comput. J.*, 13:317, 1970.

[19] D. Goldfarb. *Math. Comp.*

[20] D. F. Shanno. *Math. Comput.*, 24:647, 1970.

[21] M. R. Hestenes and E.Sriefel. *J. Res. N.B.S.*, 49:409, 1952.

[22] E. Bitzek, P. Koskinen, F. Gähler, M. Moseler, and P. Gumbsch. *Phys. Rev. Lett*, 97:170201, 2006.

[23] M. Tomić, H. O. Jeschke, R. M. Fernandes, and R. Valentí. *Physical Review B*, 87:174503, 2013.

[24] E. R. Davidson. *J. Comput. Phys.*, page 87, 1975.

[25] Y. Kamihara, H. Hiramatsu, M. Hirano, R. Kawamura, H. Yanagi, T. Kamiya, and H. Hosono. *J. Am. Chem. Soc.*, 128:10012, 2006.

[26] Y. Kamihara, T. Watanabe, M. Hirano, and H. Hosono. *J. Am. Chem. Soc.*, 130: 3296, 2008.

[27] S. He, J. He, W. Zhang, L. Zhao, D. Liu, X. Liu, D. Mou, Y. Ou, Q. Wang, Z. Li, L. Wang, Y. Peng, Y. Liu, C. Chen, L. Yu, G. Liu, X. Dong, J. Zhang, C. Chen, Z. Xu, X. Chen, X. Ma, Q. Xue, and X. J. Zhou. *Nature Mater.*, 12:605, 2013.

[28] S. Tan, Y. Zhang, M. Xia, Z. Ye, F. Chen, X. Xie, R. Peng, D. Xu, Q. Fan, H. Xu, J. Jiang, T. Zhang, X. Lai, T. Xiang, J. Hu, B. Xie, and D. Feng. *Nature Mater.*, 12:634, 2013.

[29] M. Tomić, R. Valentí, and H. O. Jeschke. *Physical Review B*, 85:094105, 2012.

[30] F. Wang and D-H. Lee. *Science*, 332:200, 2011.

[31] C. W. Chu. *Nature Phys.*, 5:787, 2009.

[32] C. de la Cruz, Q. Huang, J. W. Lynn, J. Li, W. Ratcliff II, J. L. Zarestky, H. A. Mook, G. F. Chena, J. L. Luo, N. L. Wang, and P. Dai. *Nature*, 453:899, 2008.

[33] Q. Huang, Y. Qiu, W. Bao, M. A. Green, J. W. Lynn, Y. C. Gasparovic, T. Wu, G. Wu, and X. H. Chen. *Phys. Rev. Lett.*, 101:257003, 2008.

[34] J. Zhao, Q. Huang, C. de la Cruz, S. Li, J. W. Lynn, Y. Chen, M. A. Green, G. F. Chen, G. Li, Z. Li, J. L. Luo, N. L. Wang, and P. Dai. *Nature Mater.*, 7:953, 2008.

[35] J. Chu, J. G. Analytis, C. Kucharczyk, and I. R. Fisher. *Phys. Rev. B*, 79:014506, 2009.

[36] J. Paglione and R. L. Greene. *Nature Phys.*, 6:645, 2010.

[37] I. Mazin. *Physics*, 4:26, 2011.

[38] J. Guo, S. Jin, G. Wang, S. Wang, K Zhu, T. Zhou, M. He, and X. Chen. *Phys. Rev. B*, 82:180520, 2010.

[39] M. S. Torikachvili, S. L. Bud'ko, N. Ni, and P. C. Canfield. *Phys. Rev. Lett.*, 101: 057006, 2008.

[40] A. Kreyssig, M. A. Green, Y. Lee, G. D. Samolyk, P. Zajdel, J. W. Lynn, S. L. Bud'ko, M. S. Torikachvili, N. Ni, S. Nandi, J. B. Leão, J. Poulton, D. N. Argyriou, B. N. Harmon, R. J. McQueeney, P.C. Canfield, and A. I. Goldman. *Phys. Rev. B*, 78:184517, 2008.

[41] W. Yu, A. A. Aczel, T. J. Williams, S. L. Bud'ko, N. Ni, P. C. Canfield, and G. M. Luke. *Phys. Rev. B*, 79.

[42] K. Prokeš, A. Kreyssig, B. Ouladdiaff, D. K. Pratt, N. Ni, S. L. Bud'ko, P. C. Canfield, R. J. McQueeney, D. N. Argyriou, and A. I. Goldman. *Phys. Rev. B*, 81: 180506, 2010.

[43] T. Goko, A. A. Aczel, E. Baggio-Saitovitch, S. L. Bud'ko, P. C. Canfield, J. P. Carlo, G. F. Chen, P. Dai, A. C. Hamann, W. Z. Hu, H. Kageyama, G. M. Luke, J. L. Luo, B. Nachumi, N. Ni, D. Reznik, D. R. Sanchez-Candela, A. T. Savici, K. J. Sikes, N. L. Wang, C. R. Wiebe, T. J. Williams, T. Yamamoto, W. Yu, and Y. J. Uemura.

[44] P. L. Alireza, Y. T. C. Ko, J. Gillett, C. M. Petrone, J. M. Cole, G. G. Lonzarich, and S. E. Sebastian. *J. Phys.: Condens. Matter*, 21:012208, 2009.

[45] W. Uhoya, A. Stemshorn, G. Tsoi, Y. K. Vohra, A. S. Sefat, B. C. Sales, K. M. Hope, and S. T. Weir.

[46] R. Mittal, S. K. Mishra, S. L. Chaplot, S. V. Ovsyannikov, E. Greenberg, D. M. Trots, L. Dubrovinsky, Y. Su, Th. Brueckel, S. Matsuishi, H. Hosono, and G. Garbarino. *Phys. Rev. B*, 83:054503, 2011.

[47] S. A. J. Kimber, A. Kreyssig, Y. Z. Zhang, H. O. Jeschke, R. Valenti, F. Yokaichiya, E. Colombier, J. Yan, T. C. Hansen, Chatterji T, R. J. McQueeney, P. C. Canfield, A. I. Goldman, and D. N. Argyriou. *Nature Mater.*, 8:471, 2009.

[48] A. I. Goldman, A. Kreyssig, K. Prokeš, K. Pratt, D. N. Argyriou, J. W. Lynn, S. Nandi, S. A. J. Kimber, Y. Chen, Y. B. Lee, G. Samolyuk, J. B. Leão, S. J. Poulton, S. L. Bud'ko, N. Nil, P. C. Canfield, B. N. Harmon, and R. J. McQueeney.

[49] T. Yamazaki, N. Takeshita, R. Kobayashi, H. Fukazawa, Y. Kohori, K. Kihou, C. H. Lee, H. Kito, A. Iyo, and H. Eisaki. *Phys. Rev. B*, 81:224511, 2010.

[50] W. J. Duncan, O. P. Welzel, C. Harrison, X. F. Wang, X. H. Chen, F. M. Grosche, and P. G. Niklowitz. *J. Phys.: Condens. Matter*, 22:052201, 2010.

[51] J. H. Chu, J. G. Analytis, K De Greeve, P. L. McMahon, Z. Islam, Y. Yamamoto, and I. R. Fisher. *Science*, 329:824, 2010.

[52] M. A. Tanatar, E. C. Bloomberg, A. Kreyssig, M. G. Kim, N. Ni, A. Thaler, S. L. Bud'ko, P. C. Canfield, A. I. Goldman, I. I. Mazin, and R. Prozorov. *Phys. Rev. B*, 81:184508, 2010.

[53] H.-H. Kuo, J. H. Chu, S. C. Riggs, L. Yu, P. L. MacMahon, K. De Greeve, Y. Yamamoto, J. G. Analytis, and I. R. Fisher. *Phys. Rev. B*, 84:054540, 2011.

[54] C. Dhital, Z. Yamani, W. Tian, J. Zeretsky, A. S. Sefat, Z. Wang, R. J. Birgeneau, and S. D. Wilson.

[55] T. Liang, M. Nakajima, K. Kihou, Y. Tomioka, T. Ito, C. H. Lee, H. Kito, A. Iyo, H. Eisaki, T. Kakeshita, and S. Uchida.

[56] E. C. Blomberg, A. Kreyssig, M. A. Tanatar, R. M. Fernandes, M. G. Kim, A. Thaler, J. Schmalian, S. L. Bud'ko, P. C. Canfield, A. I. Goldman, and R. Prozorov. *Phys. Rev. B*, 85:144509, 2012.

[57] J.-H. Chu, H.-H. Kuo, J. G. Analytis, and I. R. Fisher. *Science*, 337:710, 2012.

[58] C. Fang, H. Yao, W.-F. Tsai, J. Hu, and S. A. Kivelson. *Phys. Rev. B*, 77:224509, 2008.

[59] C. Xu, M. Müller, and S. Sachdev. *Phys. Rev. B*, 78:020501(R), 2008.

[60] R. M. Fernandes, L. H. VanBebber, S. Bhattacharya, P. Chandra, V. Keppens, D. Mandrus, M. A. McGuire, B. C. Sales, A. S. Sefat, and J. Schmalian. *Phys. Rev. Lett.*, 105:157003, 2010.

[61] R. M. Fernandes, E. Abrahams, , and J. Schmalian. *Phys. Rev. Lett.*, 107:217002, 2011.

[62] E. C. Blomberg, M. A. Tanatar, A. Kreyssig, N. Ni, A. Thaler, R. Hu, S. L. Bud'ko, P. C. Canfield, A. I. Goldman, and R. Prozorov. *Phys. Rev. B*, 83:134505, 2011.

[63] H-.H. Kuo, J. G. Analytis, J.-H. Chu, R. M. Fernandes, J. Schmalian, and I. R. Fisher. *Phys. Rev. B*, 86:134507, 2012.

[64] Q. Y. Wang, Z. Li, W. H. Zhang, Z. C. Zhang, J. S. Zhang, W. Li, H. Ding, Y. B. Ou, P. Deng, K. Chang, J. Wen, C. L. Song, K. He, J. F. Jia, S. H. Ji, Y. Wang, L. Wang, X. Chen, X. Ma, and Q.K. Xue.

[65] N. Colonna, G. Profeta, A. Continenza, and S. Massidda. *Phys. Rev. B*, 83:094529, 2011.

[66] Y.-Z. Zhang, H. C. Kandpal, I. Opahle, H. O. Jeschke, and R. Valentí. *Phys. Rev. B*, 80:094530, 2009.

[67] N. Colonna, G. Profeta, and A. Continenza. *Phys. Rev. B*, 83:224526, 2011.

[68] G. Kresse and J. Hafner. *Phys. Rev. B*, 47:558, 1993.

[69] N. Sata, G. Shen, M. L. Rivers, and S. R. Sutton. *Phys. Rev. B*, 65:104114, 2002.

[70] D. Johrendt, C. Felser, O. Jepsen, O. K. Andersen, A. Mewis, and J. Rouxel. *J. Solid State Chem.*, 130:254, 1997.

[71] T. Yildirim. *Phys. Rev. Lett.*, 102:037003, 2009.

[72] A. I. Coldea, C. M. J. Andrew, J. G. Analytis, R. D. McDonald, A. F. Bangura, J.-H. Chu, I. R. Fisher, and A. Carrington. *Phys. Rev. Lett.*, 103:026404, 2009.

[73] E. Granado, L. Mendonça-Ferreira, F. Garcia, G. de M. Azevedo, G. Fabbris, E. M. Bittar, C. Adriano, T. M. Garitezi, P. F. S. Rosa, L. F. Bufaiçal, M. A. Avila, H. Terashita, and P. G. Pagliuso. *Phys. Rev. B*, 83:184508, 2011.

[74] M. Aichhorn, L. Pourovskii, V. Vildosola, M. Ferrero, O. Parcollet, T. Miyake, A. Georges, and S. Biermann. *Phys. Rev. B*, 80:085101, 2009.

[75] Z. P. Yin, K. Haule, and G. Kotliar. *Nature Mater.*, 10:932, 2011.

[76] M. Aichhorn, L. Pourovskii, and A. Georges. *Phys. Rev. B*, 84:054529, 2011.

[77] J. Ferber, K. Foyevtsova, R. Valentí, and H. O. Jeschke. *Phys. Rev. B*, 85:094505, 2012.

[78] J. Ferber, H.O. Jeschke, and R. Valentí. *Phys. Rev. Lett.*, 109:236403, 2012.

[79] O. K. Andersen and L. Boeri. *Ann. Phys.*, 523:8, 2011.

[80] J. D. Clayton. *Nonlinear Mechanics of Crystals.* Springer, 2010.

[81] J. E. Jörgensen and T. C. Hansen. *Eur. Phys. J. B*, 78:411, 2010.

[82] A. Cano, M. Civelli, I. Eremin, and I. Paul. *Phys. Rev. B*, 82:020408(R), 2010.

[83] V. Barzykin and L. P. Gor'kov. *Phys. Rev. B*, 79:134510, 2009.

[84] S. Graser, A. F. Kemper, T. A. Maier, H.-P. Cheng, P. J. Hirschfeld, and D. J. Scalapino. *Phys. Rev. B*, 81:214503, 2010.

[85] J. Hu, C. Setty, and S. Kivelson. *Phys. Rev. B*, 85:100507(R), 2012.

[86] I. I. Mazin and M. D. Johannes. *Nature Phys.*, 5:141, 2009.

[87] T. B. Boykin and G. Klimeck. *Phys. Rev. B*, 71:115215, 2005.

[88] T. B. Boykin, N. Kharche, and G. Klimeck. *Phys. Rev. B*, 76:035310, 2007.

[89] T. B. Boykin, N. Kharche, G. Klimeck, and M. Korkusinski. *J. Phys. Condens. Matter*, 19:036203, 2007.

[90] W. Ku, T. Berlijn, and C. Lee. *Phys. Rev. Lett.*, 104:216401, 2010.

[91] V. Popescu and A. Zunger. *Phys. Rev. B*, 85:085201, 2012.

[92] P. V. C. Medeiros, S. Stafström, and J. Björk. *Phys. Rev. B*, 89:041407(R), 2014.

[93] C. Lin, T. Berlijn, L. Wang, C. Lee, W. Yin, and W. Ku. *Phys. Rev. Lett.*, 107: 257001, 2011.

[94] E. P. Wigner. *Gruppentheorie und ihre Anwendung auf die Quantenmechanik der Atomspektren*. Vieweg, 1931.

[95] M. El-Batanouny and F. Wooten. *Symmetry and Condensed Matter Physics; A Computational Approach*. Cambridge University Press, 2008.

[96] S. Kasahara, T. Shibauchi, K. Hasimoto, Y. Nakai, H. Ikeda, T. Terashima, and Y. Matsuda. *Phys. Rev. B*, 83:060505(R), 2011.

[97] M. D. Lumsden, A. D. Christianson, E. A. Goremychkin, S. E. Nagler, H. A. Mook, M. B. Stone, D. L. Abernathy, T. Guidi, G. J. MacDougall, C. de la Cruz, A. S. Sefat1, M. A. McGuire, B. C. Sales, and D. Mandrus. *Nature Phys.*, 6:182, 2010.

[98] J. T. Park, D. S. Inosov, A. Yaresko, S. Graser, D. L. Sun, P. Bourges, Y. Sidis, Yuan Li, J.-H. Kim, D. Haug, A. Ivanov, K. Hradil, A. Schneidewind, P. Link, E. Faulhaber, I. Glavatskyy, C. T. Lin, B. Keimer, and V. Hinkov. *Phys. Rev. B*, 82:134503, 2010.

[99] S. A. J. Kimber, A. Salamat, S. R. Evans, H. O. Jeschke, K. Muthukumar, M. Tomić, F Salvat-Pujol, R. Valentí, M. V. Kaisheva, I. Zizak, and T. Chatterji.

[100] A. Ruff, M. Sing, R. Claessen, H. Lee, M. Tomić, H. O. Jeschke, and R. Valentí. *Phys. Rev. Lett.*, 110:216403, 2013.

[101] T. Chattopadhyay and H. G. Schnering. *J. Phys. Chem. Solids*, 46:113, 1985.

[102] T. Chattopadhyay, H. G. Schnering, and W. A. Grosshans. *Physica B*, 139-140: 305, 1986.

[103] A. R. Oganov and C. W. Glass. *J. Chem. Phys*, 124:244704, 2006.

[104] C. W. Glass, A. R. Oganov, and N. Hansen. *Comput. Phys. Commun.*, 175:713, 2006.

[105] A. Togo, F. Oba, and I. Tanaka. *Phys. rev. B*, 78:134106, 2008.

[106] J. M. Hastings, N. Elliot, and L. M. Corliss. *Phys. Rev.*, 115:13, 1959.

[107] R. Mitsuhashi, Y. Suzuki, Y. Yamanari, H. Mitamura, T. Kambe, N. Ikeda, H. Okamoto, A. Fujiwara, M. Yamaji, and N. Kawasaki. *Nature(London)*, 464:76, 2010.

[108] K. Teranishi, H. Xe, Y. Sakai, M. Izumi, H. Goto, R. Eguchi, Y. Takabayashi, T. Kambe, and Y. Kubozono. *Phys. Rev. B*, 87:060505(R), 2013.

[109] A. De, R. Ghosh, S. Roychowdhury, and P. Roychowdhury. *Acta Cryst.*, C41:907, 1985.

[110] P. L.de Andres, A. Guijarro, and J. A. Vergés. *Phys. Rev. B*, 83:245113, 2011.

[111] M. Aroyo and H. Wondratschek. Representation of crystallographic groups. 2010. URL http://www.crystallography.fr/mathcryst/pdf/nancy2010/Aroyo_reps2010.pdf.

[112] M. Damjanović. Hilbertovi prostori i grupe. 2000. URL http://www.ff.bg.ac.rs/Katedre/QMF/pdf/y2k.pdf.

[113] M. Damjanović. O simetriji u kvantnoj nerelativističkoj fizici. 2000. URL http://www.ff.bg.ac.rs/Katedre/QMF/pdf/sknf2e.pdf.

[114] S. K. Kim. *Group Theoretical Methods and Applications to Molecules and Crystals*. Cambridge University Press, 1999.